Technische Universität München

Max-Planck-Institut für Quantenoptik

Entanglement States in Ion Traps: Properties and Applications

Xiaolong Deng

Vollständiger Abdruck der von der Fakultät für Physik
der Technischen Universität München
zur Erlangung des akademischen Grades eines

Doktors der Naturwissenschaften (Dr. rer. nat.)

genehmigten Dissertation.

Vorsitzender : Univ.-Prof. Dr. Rudolf Gross

Prüfer der Dissertation : 1. Hon.-Prof. Ignacio Cirac, Ph. D.
2. Univ.-Prof. Dr. Manfred Kleber

Die Dissertation wurde am 03.04.07 bei der
Technischen Universität München eingereicht und
durch die Fakultät für Physik am 07.05.07 angenommen.

Abstract

This thesis is devoted to the theoretical study of strongly correlated quantum many-body states with trapped ions interacting with lasers. A system of trapped ions under the action of off–resonant standing–waves can be used to simulate a variety of quantum interacting models. Based on this idea we study in detail effective quantum spin models and Bose-Hubbard model in ion traps.

In the first part of the thesis we review the physics of ion traps, which is considered as the basics of building quantum simulators with trapped ions. We derive the vibrational modes in a string of ions, discuss the ion-laser interaction in the Lamb-Dicke limit, and explain how to prepare and detect quantum states in ion-trap experiments.

In the second part of the thesis we build up our own DMRG method for an inhomogeneous system with long-range interactions or hoppings. We discuss how to actualize the operators and correlations in the DMRG steps, and how to speed up the calculations.

In the third part we describe theoretically effective quantum spin models in ion traps. The coupling between internal states and vibrational modes under the off-resonant standing-wave can be written as an effective spin interacting Hamiltonian plus a residual spin-phonon coupling. Our numerical calculations with the DMRG method show that experiments with ion traps should allow one to access general properties of quantum critical systems. On the other hand, ion trap quantum spin models show a few novel features due to the peculiarities of induced effective spin–spin interactions which lead to interesting effects like long–range quantum correlations and the coexistence of different spin phases.

In the fourth part we focus on the phonon-Hubbard model in ion traps. The vibrations of a chain of trapped ions can be considered, under suitable experimental conditions, as an ensemble of interacting phonons, whose quantum dynamics is governed by a Bose–Hubbard Hamiltonian. Our studies of this system show that thermodynamical properties, such as critical parameters and critical exponents, can be measured in experiments with a limited number of ions. Besides that, interacting phonons in trapped ions offer us the possibility to access regimes which are difficult to study with ultracold bosons in optical lattices, like models with attractive or site–dependent phonon-phonon interactions.

Zusammenfassung

Diese Arbeit behandelt die theoretische Untersuchung von stark korrelierten Quanten-Vielteilchen-Zuständen, die bei gefangenen Ionen, die mit Lasern wechselwirken, auftreten. Ein Systen aus gefangenen Ionen unter Einwirkung von off-resonanten stehenden Wellen kann dazu verwendet werden, eine Vielzahl von Modellen mit Quantenwechselwirkungen zu simulieren. Basierend auf dieser Idee studieren wir im Detail effektive Quanten-Spin-Modelle und das Bose-Hubbard Modell.

Im ersten Teil der Arbeit wiederholen wir die Physik von Ionenfallen, welche die Basis für einen Quantensimulator mit gefangenen Ionen bilden. Wir berechnen die Vibrationsmoden in einer Ionenkette, diskutieren die Ionen-Laser Wechselwirkung im Lamb-Dicke Limit und erklären, wie Quantenzustände in Ionenfallen-Experimenten präpariert und gemessen werden.

Der zweite Teil der Arbeit behandelt unsere eigene DMRG-Methode für inhomogene Systeme mit langreichweitigen Wechselwirkungen oder Tunneleffekten. Wir diskutieren, wie Operatoren und Korrelationen in den einzelnen DMRG-Schritten aktualisiert werden und wie eine Geschwindigkeitsoptimierung erreicht wird.

Im dritten Teil beschreiben wir theoretisch die effektiven Quanten-Spin-Modelle, die in Ionenfallen simuliert werden können. Die Kopplung zwischen den internen Zuständen und den Vibrationsmoden unter der Einwirkung von off-resonanten stehenden Wellen kann als effektive Spin-Wechselwirkung plus einer Spin-Phonon Kopplung geschrieben werden. Unsere numerischen Berechnung mittels DMRG zeigen, dass mittels Experimenten mit Ionenfallen Erkenntnis über allgemeine Eigenschaften von kritischen Quantensystemen erlangt werden kann. Desweiteren zeigen Quanten-Spin-Modelle in Ionenfallen zahlreiche neue Eigenschaften aufgrund der Besonderheiten der induzierten Spin-Spin Wechselwirkungen. Diese führen zu interessanten Effekten - wie langreichweitigen Quantenkorrelationen oder der Koexistenz von unterschiedlichen Spin-Phasen.

Im vierten Teil behandeln wir das Phonon-Hubbard Modell in Ionenfallen. Die Vibrationen in einer Kette von gefangenden Ionen, können, unter geeigneten experimentellen Zuständen, als Ensemble von wechselwirkenden Phononen betrachtet werden, dessen Dynamik vom Bose-Hubbard Hamiltonian bestimmt wird. Unsere Untersuchungen dieses Systems zeigen, dass die thermodynamischen Eigenschaften, wie kritische Parameter oder kritische Exponenten, in Experimenten mit einer geringen Anzahl von Ionen gemessen werden können. Desweiteren bieten uns wechselwirkende Phononen in gefangenen Ionen die Möglichkeit, Bereiche zu analysieren, die mittels ultrakalter Bosonen in optischen Gittern schwierig zu erreichen sind - wie Modelle mit

attraktiver oder ortsabhängiger Phonon-Phonon Wechselwirkung.

Contents

Chapter 1

Introduction

The goal of quantum many–body physics is to understand the properties of real materials ranging from quantum magnets to high–Tc superconductors. For this task, theorists have developed a variety of simplified models, such as spin models and Hubbard models [1], which allow us to describe the rich phenomenology, especially strongly correlated quantum mechanics, which is observed in those materials. However, those real systems corresponding to these simplified models are very difficult to be controlled in experiments, due to disorder and complicated structures. Moreover, many of these simplified models are not accessible to exact theoretical treatments in the strongly correlated regime. In the last years, progress in laser cooling and manipulations of cold atoms at the microscopic scale [2] has changed dramatically this situation. Experiments in atomic physics and quantum optics offer us the possibility to find experimental realizations of the above theoretical models which were first proposed in the context of condensed matter physics [3,4,5]. The basic idea is to perform quantum simulations with an analogue system [6] or a quantum computer [7]. In this way quantum interacting models can be studied in a controlled and clean way and some of the limitations of solid-state set-ups are overcome. Thus, the interplay between atomic and many–body physics is becoming an exciting research field.

On the one hand, cold atoms in optical lattices are an excellent experimental set-up to simulate other quantum many-body systems [5]. The optical lattice is formed by three orthogonal pairs of counterpropagating (standing-wave) laser beams that are off-resonant with the atomic transition [2]. The induced ac-Stark shift (we will explain this effect for trapped ions in Chapter 2) makes the atoms trapped in the minima of the three-dimensional lattice potential. By tuning the lattice potential depth, one can control the kinetic energy of the atoms and the interaction between them. The optical lattice not only provides us with high controllability and manipulation of trapped

atoms at quantum levels, but its geometry and dimensionality are also controllable easily. In addition, as a clean experimental set-up the optical lattice avoids the unwanted interactions and disorder in real materials, or it allows one to add them on purpose. In 1998 D. Jaksch *et al.* [8] proposed the realization of the superfluid-Mott insulator transition with cold atoms in optical lattices. The first experimental step in this direction was made in 2002 by M. Greiner *et al.* [9] with the successful observation of the quantum phase transition at the zero temperature from a superfluid to a Mott insulator in a gas of ultracold atoms in an optical lattice. In the experiment, starting from a Bose-Einstein condensate loaded in a three-dimensional optical potential, the system undergoes a superfluid-Mott insulator transition with the lattice potential depth increasing until the on-site interaction between atoms prevails over their kinetic energy. Thus, the work by D. Jaksch *et al.* [8] and by M. Greiner *et al.* [9] opened the door of theoretically and experimentally studying strongly correlated many-body quantum mechanics with ultracold atoms. Stimulated by their work, a large number of theoretical proposals using optical lattices come out to mimic various condensed matter models of interest [10,11,12,13,14,15,16,17,18,19,20], see the reviews in Refs. [5,21,22]. And a large number of experiments are devoted to investigating behaviors of ultracold atoms in optical lattices in the strongly correlated regime [23,24,25,26,27]. The bosonic superfluid–Mott insulator transition in disordered Bose systems [28] and in Bose-Fermi mixtures [29,30], the Mott state of molecules [31] and bound repulsive pairs of atoms [32] have been created and observed in experiments. The Tonks-Girardeau gas of ultracold atoms in an optical lattice has also been observed directly in the experiments [33,34,35,36]. The fermionic atoms have also been loaded into an optical lattice, and the BEC-BCS crossover has been observed [37,38,39,40,41].

On the other hand, trapped ions [42] are another clean experimental system in which quantum optics offers us accurate techniques for the manipulation and measurement of quantum states [43, 44, 45, 46, 47]. In the last years this experimental field has been mainly motivated by applications to quantum information processing [48, 49, 50]. The original scheme of quantum computing with trapped ions was proposed by J. I. Cirac and P. Zoller in 1995 [51]. Then soon, the first experiment demonstrating an ion-trap quantum logic gate was performed in the D. Wineland's group at NIST in Boulder, USA [52]. Since their seminal work [51, 52] ion traps have been widely regarded as a leading candidate for quantum computing, and lots of theoretical work based on ion traps has been proposed [53, 54, 55, 56, 57, 58]. The Cirac-Zoller 1995 proposal [51] considers a linear Paul trap, where two hyperfine levels of the internal ground states of the ions are used as qubits, and collective vibrational modes allow us to perform quantum gates between

them. These ion-qubits can be addressed individually with laser beams. The original scheme depends on the possibility of achieving the ground state of vibrational modes by laser cooling and on the ability of manipulating a quantum state in a precisely controlled manner. However, due to the limited confinement in a linear Paul trap, it is difficult to scale this architecture to more than a few ions. In 2000, J. I. Cirac and P. Zoller suggested another quantum computing scheme called pushing gate [56], using trapped ions in an array of microtraps, which could be scalable in experiments. In this scheme off-resonant standing waves are introduced to create internal-state-dependent dipole forces on trapped ions. Thus, two–qubit gates between two neighboring ions would depend on the particular internal state. The details of this scheme has been explained in Ref. [59]. On the experimental side there has been remarkable progress in recent years [60, 61, 62, 63, 64, 65, 66, 67, 68]. For example, quantum algorithms for a few particles has been implemented in ion traps [64,65,66], and entangled states of up to eight ions have been prepared in experiments [67, 68].

In fact, trapped ions are also an experimental system with potential applications to the quantum simulation of many–body problems as cold atoms in an optical lattice. The coherent manipulation of their internal and vibrational states could be used to simulate the dynamics of other systems [3, 69, 70, 71, 72, 73, 74, 75]. In particular, D. Porras and J. I. Cirac have shown recently that trapped ions can be used for the study of a rich variety of quantum interacting models [70, 71, 74]. The internal states coupling to the vibrational modes by the lasers can result in an effective spin-spin interaction under certain conditions. By using similar experimental techniques to quantum computing, one can use trapped ions to simulate interacting quantum spin models [70]. With this proposal, the Heisenberg Hamiltonian could be implemented in ion traps, which is very interesting from the perspective of magnetism. In this way, the physics of quantum magnetism could be accessed in experiments with ion traps. On the other hand, the vibrational modes of a chain of trapped ions under suitable experimental conditions follow the quantum dynamics of a Bose–Hubbard model [71]. The interaction between phonons is induced by the anharmonicities of an optical potential, which can also be created by an off–resonant standing wave. The hopping term is from the Coulomb potential. Thus trapped ions provide us with another way to observe the superfluid-Mott insulator quantum phase transition. The experimental requirements for the study of quantum interacting systems with trapped ions are indeed much less stringent than those for quantum information tasks. It also has the advantage that internal electronic or quantum vibrational states can be measured at the single particle level [44, 47, 60], since the distance between ions is large enough to address them individually

by optical means.

This thesis contributes to the theoretical study of quantum simulations of many-body systems with trapped ions. In the following chapters we will mainly focus on the two schemes–effective spin models and Bose-Hubbard model with trapped ions, proposed in Refs. [70] and [71]. Below we give an overview of the content of this thesis.

In Chapter 2 we review the physics of ion traps, which is the carrier of building our quantum simulators. In our study we mainly use two types of ion traps: the linear Paul trap and the array of microtraps. We give their draft structures and talk about how to confine the ions by these traps. Then we give a description of the internal electronic states of trapped ions, and derive the vibrational modes in the thermodynamic limit and in finite size systems, respectively. The ion-laser interaction is the most important part in this chapter. We consider two cases of lasers: the traveling wave and the standing wave. To simplify our analysis we limit the interaction Hamiltonian in the Lamb-Dicke regime, and get some further simplified Hamiltonians which are used to engineer quantum states of trapped ions. We also explain the internal-state-dependent force on the ions due to the off-resonant standing waves, which is the starting point of our schemes. At the end we discuss how to prepare and detect internal and vibrational states, which would make our proposals possible in experiments.

In Chapter 3 we develop the numerical tool–the density matrix renormalization group (DMRG) [76, 77], so that it allows us to deal with inhomogeneous systems with long-range interactions or hoppings. The DMRG suffices for studying one-dimensional strongly correlated system. We first review the basic ideas of the DMRG method, based on the singular value decomposition of the wavefunction. Then we illustrate our own algorithms which is for long-range interacting or hopping models. Thirdly, we talk about how to project the operators and correlations onto new basis at each steps in the DMRG, in order to construct the new Hamiltonian for the next step. The efficiency of the algorithms is discussed at the end of this chapter. We mainly perform three large improvements to speed up our calculations: block storage, state prediction and good quantum numbers. Our source codes are written in Matlab, which has highly efficient functions to solve (sparse) large matrices.

In Chapter 4 we pursue the ideas proposed in Ref. [70] for the realization of a quantum simulator of quantum magnetism with trapped ions. We first describe theoretically how to create the effective spin models with trapped ions in the simplest realizations: quantum Ising model and XY model. The decoherence in our spin models is analyzed carefully. With the DMRG method we then investigate numerically the different quantum phases of

these two models in a linear Paul trap and in an array of microtraps, respectively. The ion-trap quantum spin models have some novel features due to their peculiar spin-spin interactions. We explain quantitatively the long-range quantum Ising correlations under the spin wave formalism through the Holstein-Primakoff transformation. We also show the coexistence of different phases in the linear Paul trap.

In Chapter 5 we focus on the ideas proposed in Ref. [71] for the realization of a phonon-Hubbard model with trapped ions. First we derive the Bose–Hubbard model for phonons in a chain of trapped ions, in the presence of the anharmonicities induced by an optical dipole potential. The conditions of keeping phonons conserved and getting phonon-phonon interactions and hoppings are discussed, respectively. By means of the DMRG we study different quantum phases of interacting phonons, such as the superfluid, Mott-insulator and Tonks-gas phases, under the relevant experimental parameters. Besides that, we also investigate in detail the phonon-Hubbard models with attractive and site-dependent on-site interactions, respectively.

The result presented in Chapter 4 is published in [72]. The result in Chapter 5 is submitted to Phys. Rev. **A** [75].

Chapter 2

Ion Traps

Atomic ions can be confined by particular arrangements of electromagnetic fields [42, 78]. By means of laser cooling [2, 79, 80, 81], trapped ions can approach a sufficiently low temperature, and form a crystal structure at equilibrium where the Coulomb repulsion among them balances the trapping potential. Small displacements of trapped ions around their equilibrium positions are strongly coupled due to the Coulomb interaction between them. However, in the harmonic approximation (i.e. the small displacements of ions around equilibrium positions are much smaller than the distances between ions), small displacements can be expressed in terms of normal modes, which are uncoupled.

Trapped ions can be controlled easily and precisely with lasers. The laser interacting with trapped ions can couple their internal states with their motion (i.e. normal modes), which indeed offers possibilities of preparing and manipulating quantum states of motion of trapped ions. Some important states in quantum mechanics, such as Fock states, coherent states, squeezed states and Schödinger cat states have already been generated and detected in ion-trap experiments [44, 47, 60].

In this chapter we review the theoretical description of ion traps which is closely related to building our quantum simulators in this thesis. First we talk about the different types of ion traps used in the thesis: the linear Paul trap and the array of ion microtraps. Second, the physics of trapped ions is given: the internal states of ions in the two-level approximation and vibrational modes of a string of ions. Third, we derive the basic ion-laser interaction Hamiltonians for the traveling wave and the standing wave, respectively, discuss the Hamiltonians in the Lamb-Dicke limit, and explain the state-dependent force in a far-detuned standing wave, which plays a very important role in building our models. The last section is about how to prepare and detect quantum states (internal and motional states) in ion traps.

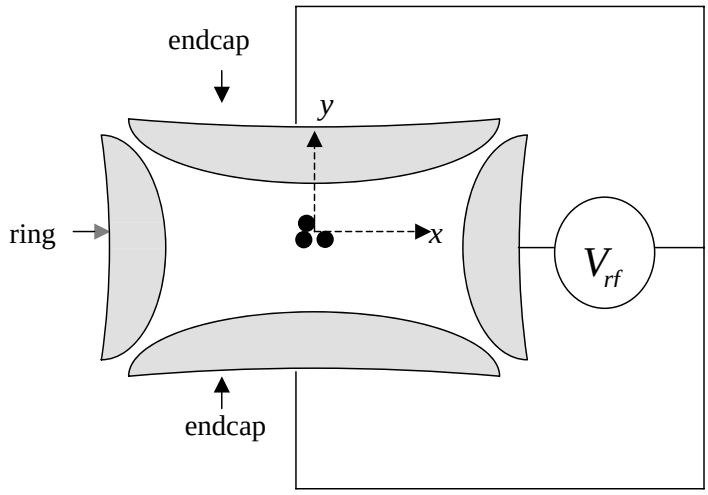

Figure 2.1: Draft scheme of a Paul trap with trapped ions. A rf voltage V_{rf} is applied between the endcap and ring electrodes. The coordinates x and y direct along the principal axes of the trap.

2.1 The different types of ion traps

From the Earnshaw's theorem, it is impossible to confine an ion using a purely electrostatic field [81]. Therefore to create a stable trap one has to apply a time-varying electric field or a combination of a static electric and magnetic field. There are two traditional traps: the Paul trap and the Penning trap. The Paul trap uses radio-frequency (rf) fields to confine ions, while the Penning trap uses static electric fields and a static magnetic field to do so. The Paul trap can be extended to a linear Paul trap under some designs. There is also an array of ion microtraps, which is composed of electric or magnetic fields and of high scalability. In the following subsections, we will give some brief explanations about the Paul trap, the linear Paul trap and an array of ion microtraps. The work in this thesis is not related to the Penning trap.

2.1.1 The Paul trap

In the Paul trap a radio-frequency voltage $V_{rf} = V_0 \cos(\omega_{rf} t)$ is applied between the endcap and ring electrodes to confine ions, see Fig. 2.1 for the configuration.

The quadrupole potential of the Paul trap in 2D is of the form

$$\Phi = V_0 \cos(\omega_{rf} t)(x^2 - y^2). \tag{2.1}$$

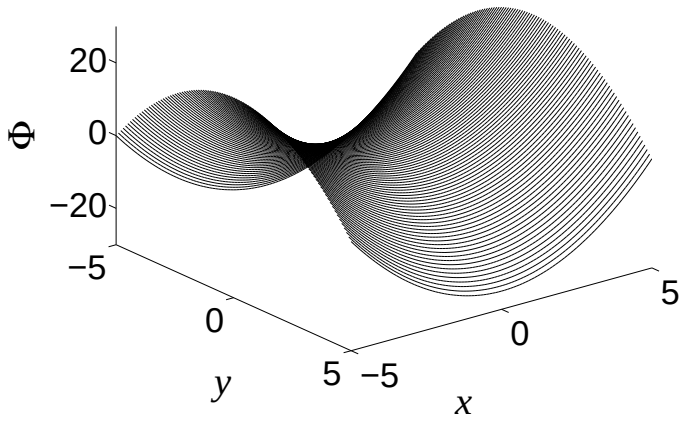

Figure 2.2: Saddle potential Φ of a Paul trap. Stable dynamic equilibrium at $x = y = 0$ is achieved with a rf voltage V_{rf}.

If there is no radio-frequency voltage, but a direct-current voltage applied between the electrodes, the above Eq. (2.1) represents a saddle potential, see Fig. 2.2. There is no stable equilibrium for the ion, since any slight displacements from the center of the saddle potential (where the ion experiences no force) will cause the ion to be off down the sides. However, if one applies a radio-frequency voltage between the electrodes, a trapping is obtained, since reversing the sign of rf voltage with time means rotating the saddle potential around the vertical axis, and it leads to a stable dynamic equilibrium on average. With an appropriate frequency ω_{rf}, ions can be trapped stably.

The Paul trap is mostly used for studying quantum dynamics of single trapped ions interacting with lasers.

2.1.2 The linear Paul trap

The linear Paul trap is very important in quantum information processing. Not only the Cirac-Zoller quantum computing proposal [51] but also our quantum simulators [72, 75] are mainly based on the linear Paul trap. It is indeed made by extending a Paul trap. In Fig. 2.3 we show the schematic drawing of a linear Paul trap with a string of ions.

A radio-frequency potential $V_{rf} = V_0 \cos(\omega_{rf} t)$ is applied between two pairs of diagonally opposite rod electrodes for confining the ions in the radial direction, as explained for the Paul trap in the above subsection. From Eq.

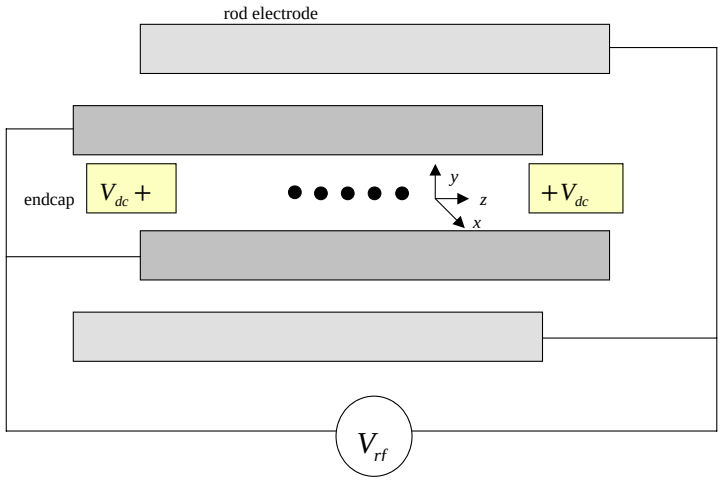

Figure 2.3: Draft scheme of a linear Paul trap with a string of trapped ions. It consists of four rod electrodes and two endcap electrodes. A rf voltage V_{rf} is applied between two pairs of diagonally opposite rod electrodes, i.e. electrodes labeled 1,3 and electrodes labeled 2,4. The endcap electrodes have a positive direct-current voltage V_{dc}. The z–direction is along the trap axis.

(2.1), one can get the equations of motion in the radial direction. Its stable solutions show that a confined ion oscillates as if it is trapped in a harmonic pseudopotential Ψ in the radial direction, given by

$$q\Psi = \frac{1}{2}m\omega_x^2 x^2 + \frac{1}{2}m\omega_y^2 y^2, \tag{2.2}$$

where q, m, ω_x and ω_y denote the ion charge, mass and radial trapping frequencies, and (x, y) is the position of the ion.

An additional static electric potential V_{dc} is created along the z axis on the end caps for preventing the ions from escaping along the axis z–direction. This create a static harmonic potential in the z–direction with the longitudinal trapping frequency ω_z.

Therefore, the resulting effective pseudopotential Ψ for an ion confined in a linear Paul trap in three directions is given by

$$q\Psi = \frac{1}{2}m\omega_x^2 x^2 + \frac{1}{2}m\omega_y^2 y^2 + \frac{1}{2}m\omega_z^2 z^2. \tag{2.3}$$

The trapping frequencies ω_x, ω_y and ω_z depend on the rf frequency, direct-current voltage, ion mass, ion charge and geometry configuration of the trap, see the Ref. [42] for the detailed derivation.

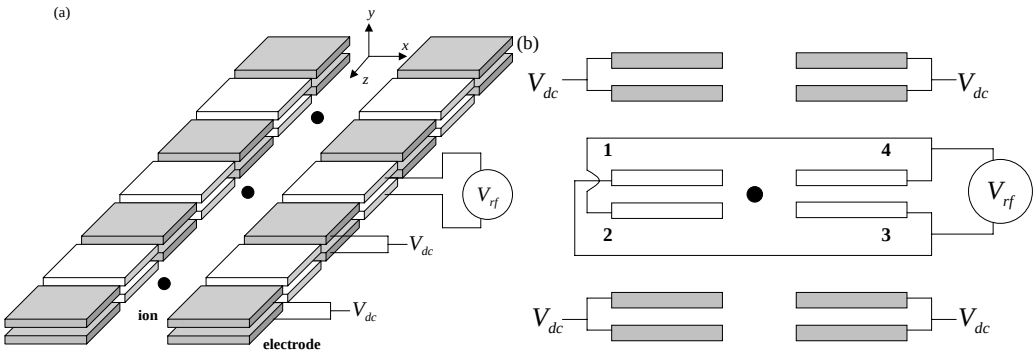

Figure 2.4: (a) A draft scheme of an array of microtraps. A string of ions lie along the z–axis as shown in the figure. The radio-frequency voltages V_{rf} and static voltages V_{dc} are applied to white electrodes and gray electrodes, respectively. Twelve electrodes (4 white rf-electrodes and 8 gray dc-electrodes on both sides) form a sub-microtrap. Each sub-microtrap confines only one ion individually. (b) The side views of the separate parts, i.e. dc and rf electrodes of an ion sub-microtrap. The dc voltage V_{dc} creates the confinement along the z–axis direction. The rf voltage V_{rf} creates a 2D quadrupole field to confine the ion. The effect of a microtrap is the same as a linear Paul trap.

In the linear Paul trap, typically $\omega_x, \omega_y \gg \omega_z$, the ions are strongly confined in the radial direction and arrange a linear chain along the trap axis.

2.1.3 The array of microtraps

The array of ion microtraps was first proposed by R. DeVoe [82]. This type of ion traps can be fabricated using semiconductor micromachining and lithographic techniques such as micro-electro-mechanical-systems (MEMS) and molecular beam epitaxy. Such a device can be integrated up to a long 1D chain or a large 2D pattern. Therefore it has a potential application to scalable quantum computing. Based on the experimental work by the C. Monroe's group [83, 84], here we give some explanations about the basic structure of an array of microtraps.

A scheme diagram of an array of ion microtraps is shown in Fig. 2.4. The design, illustrated in Fig. 2.4, is a two-layer planar geometry where both layers are divided into separate electrodes. The division of each layer into six electrodes (2 white and 4 gray in the figure) accommodates both the

rf potentials V_{rf} and the static potentials V_{dc} needed to create a linear Paul trap. The radio-frequency voltages V_{rf} are applied between each set of diagonally opposing white electrodes, as shown in Fig. 2.4. In the cross-section plane at $z = 0$,the radio-frequency generates a two-dimension trapping pseudopotential, as is discussed in Subsection 2.1.2 about the linear Paul trap. Applying the direct-current voltages V_{dc} to the endcap electrodes (gray electrods on both sizes of the white) generates a potential, which provides axial confinement for ions in the center of traps. One could distribute the individual microtraps in space to form a 1D chain or a 2D pattern. The separations between adjacent microtraps are same, and typically about $d \simeq 1 - 500\mu m$, which allows for individual addressing of the ions.

In this thesis we always study the behaviors both in an array of microtraps and in a linear Paul trap, and compare them. The array of microtraps could give a more clear picture of quantum phase transitions.

2.2 The physics of trapped ions

2.2.1 Internal states

In general, we assume the internal structure of the ion has two levels. It is straightforward to obtain fundamental properties, neglecting unnecessary details [85]. We consider a two-level ion with internal states $|g\rangle$ (ground state) and $|e\rangle$ (excited state), and the corresponding energies E_g and E_e. Its Hamiltonian is

$$\begin{aligned} H_{atom} &= E_e|e\rangle\langle e| + E_g|g\rangle\langle g| \\ &= \frac{\hbar\omega_{eg}}{2}\sigma^z + \frac{E_e + E_g}{2}I, \end{aligned} \tag{2.4}$$

where $\omega_{eg} = \frac{E_e - E_g}{\hbar}$ is the atomic resonance frequency between $|e\rangle$ and $|g\rangle$, σ^z is a Pauli operator, and I is a unity matrix.

For convenience, we give here the Pauli operators and the unity matrix:

$$\begin{aligned} &\sigma^x = |g\rangle\langle e| + |e\rangle\langle g|, \quad \sigma^y = i(|g\rangle\langle e| - |e\rangle\langle g|), \\ &\sigma^z = |e\rangle\langle e| - |g\rangle\langle g|, \qquad I = |e\rangle\langle e| + |g\rangle\langle g|. \end{aligned} \tag{2.5}$$

We may define raising and lowering operators

$$\sigma^+ = |e\rangle\langle g|, \quad \sigma^- = |g\rangle\langle e|, \tag{2.6}$$

then

$$\sigma^x = \sigma^+ + \sigma^-. \tag{2.7}$$

If we set the zero of energy equal to the energy of the level $|g\rangle$, the Hamiltonian (2.4) will be

$$H_{atom} = \hbar\omega_{eg}|e\rangle\langle e|. \tag{2.8}$$

Or if we shift the zero of energy to $\frac{E_e+E_g}{2}$, we get the rescaled energy

$$H_{atom} = \hbar\frac{\omega_{eg}}{2}\sigma^z. \tag{2.9}$$

Typically, the internal resonant frequency ω_{eg} will be much larger than any motional mode frequency ω_{vib}, i.e. $\omega_{eg} \gg \omega_{vib}$.

2.2.2 Vibrational modes

It is well known in solid state physics that the motion of some interacting particles can be described by some motional eigenmodes (vibrational modes) corresponding to eigenfrequencies [86]. The same holds for a system of trapped ions [45, 87].

Small displacements

We consider a string of N ions with mass m and charge $+e$ confined in a harmonic potential with cylindrical symmetry. From Eq. (2.3), the Hamiltonian including the trapping potential and the Coulomb repulsion reads:

$$\begin{aligned} V &= \frac{1}{2}m\sum_{i=1}^{N}\left(\omega_x^2x_i^2+\omega_y^2y_i^2+\omega_z^2z_i^2\right)+ \\ &\quad \frac{1}{2}\sum_{i,j=1,j\neq i}^{N}\frac{e^2}{\sqrt{(x_i-x_j)^2+(y_i-y_j)^2+(z_i-z_j)^2}}, \end{aligned} \tag{2.10}$$

where x_i, y_i and z_i are the absolute position of the ith ion in three orthogonal directions, ω_x, ω_y and ω_z are the radial(x and y direction) and longitudinal (z direction) trap frequencies, and $\omega_x, \omega_y \gg \omega_z$. However, here $\gg$ only means greater enough, so that the ions may form a chain, but the small oscillations in the radial directions will not be neglected. The amplitude of these oscillations is much smaller than the separation between ions, so we may describe the vibrations around the equilibrium points in harmonic approximation[1].

[1]Here we give a general description of small bounded motions around equilibrium points $(x_1^{(0)}, x_2^{(0)}, ..., x_n^{(0)})$ for the energy potential $V(x_1, x_2, ..., x_n)$. Let q_i denote a small displacement around equilibrium point $x_i^{(0)}$. Expanding the potential energy in a Tayler series,

Since in the Coulomb chain, the vibrational modes are uncoupled in each orthogonal direction, so that we can address the displacements in x, y, and z directions separately.

The equilibrium points $(x_i^{(0)}, y_i^{(0)}, z_i^{(0)})$ are determined by the first derivative of the potential via $\left(\frac{\partial V}{\partial r_i^\alpha}\right)_0 = 0$, where

$$\frac{\partial V}{\partial r_i^\alpha} = m\omega_\alpha^2 r_i^\alpha + \sum_{j,j\neq i} \frac{e^2(r_j^\alpha - r_i^\alpha)}{(\sqrt{(x_i-x_j)^2+(y_i-y_j)^2+(z_i-z_j)^2})^3}, \qquad (2.14)$$

$\alpha = x, y, z$ represents x, y or z direction, and $r_i^\alpha = x_i, y_i, z_i$ represents the absolute position x_i, y_i or z_i of the ith ion. For a linear Paul trap it is obvious that $x_0^{(0)} = y_0^{(0)} = 0$. Then only $z_0^{(0)}$ needs to obtain from Eq. 2.14 by numerical calculations. The distance between ions is smaller at the center of the chain than on both sides. Typically the distance between ions (eg. 2μm) is of the order of 10 optical wavelengths (eg. 313nm), which allows one to individually address the ions.

The second derivatives are

$$\frac{1}{\omega_\alpha^2}\frac{\partial^2 V}{\partial r_i^\alpha \partial r_j^\alpha} = \begin{cases} 1 - c_\alpha \sum_{j'(\neq i)} \frac{e^2/m\omega_\alpha^2}{|z_i^0 - z_{j'}^0|^3} & i = j \\ +c_\alpha \frac{e^2/m\omega_\alpha^2}{|z_i^0 - z_j^0|^3} & i \neq j \end{cases}. \qquad (2.15)$$

where $c_{x,y} = 1$, $c_z = -2$.

In the end, V is expressed as a function of the displacements around the

---

we have

$$V(x_1, ..., x_n) = V_0 + \sum_i \left(\frac{\partial V}{\partial x_i}\right)_0 q_i + \sum_{i,j} \frac{1}{2}\left(\frac{\partial^2 V}{\partial x_i \partial x_j}\right)_0 q_i q_j + \cdots, \qquad (2.11)$$

where $V_0 \equiv V(x_1^{(0)}, ..., x_n^{(0)})$, and the higher order terms $\mathcal{O}(q_i^3)$ may be neglected in harmonic approximation.

At equilibrium

$$\left(\frac{\partial V}{\partial x_i}\right)_0 = 0. \qquad (2.12)$$

Redefine $V_0 = 0$, then the potential energy has the form

$$V(x_1, ..., x_n) = \frac{1}{2}\sum_{i,j}\left(\frac{\partial^2 V}{\partial x_i \partial x_j}\right)_0 q_i q_j = \frac{1}{2}\sum_{i,j} V_{ij} q_i q_j, \qquad (2.13)$$

where $V_{ij} \equiv \left(\frac{\partial^2 V}{\partial x_i \partial x_j}\right)_0$.

equilibrium positions:

$$V = \frac{1}{2}m\omega_\alpha^2 \sum_{\alpha,i,j} \mathcal{K}_{i,j}^\alpha q_i^\alpha q_j^\alpha, \tag{2.16}$$

where $\mathcal{K}_{i,j}^\alpha \equiv \frac{1}{\omega_\alpha^2}\left(\frac{\partial^2 V}{\partial r_i^\alpha \partial r_j^\alpha}\right)_0$ and $q_i^\alpha = r_i^\alpha - r_i^{\alpha(0)}$.

Normal modes

The complete vibrational Hamiltonian contains the trapping potential, the Coulomb interaction, and the kinetic energy, written as

$$H_{vib} = \sum_\alpha \left(\frac{1}{2}m\omega_\alpha^2 \sum_{i,j} \mathcal{K}_{i,j}^\alpha q_i^\alpha q_j^\alpha + \frac{1}{2m}\sum_i p_i^{\alpha 2}\right). \tag{2.17}$$

where p_i^α is the momentum of the ith ion in the α direction. In Eq. (2.17), small displacements of different ions q_i^α and q_j^α are coupled each other due to the Coulomb interaction. The motion of the ion string cannot be described in terms of the motion of individual ions. Instead, it can be described in terms of eigen-modes (normal modes) of the entire ions with distinct eigen-frequencies. In the following lines, we consider normal modes in two cases: idealized case (infinite ion chain with constant distance between ions) and real case (finite ion chain with non-constant distance between ions). In the idealized case we approximate that the ions are arranged in a chain with constant space d_0. This approximation could be justified if the laser interacts with the central part of the linear chain only, where the variations of the distance between ions are very small. Under this approximation we can get analytically the dispersion relations for radial and longitudinal trapping frequencies. In experiments with a linear Paul trap, however, one deal with a finite ion string with different distances between ions. Therefore, it is also necessary to consider the real experimental case. The normal modes in this case could be calculated numerically.

First, we consider an infinite chain with constant distance d_0 between ions. Using the Fourier transform, one can decouple the small displacements in Eq. (2.17), and obtain the normal modes of the entire chain.

For concreteness, we consider the case of the radial modes in the direction of x, perpendicular to the axis of the Coulomb chain. In the infinite chain

limit we define a continuum of collective modes

$$\begin{aligned} Q_q &= \frac{1}{\sqrt{2\pi}} \sum_{r=-\infty}^{\infty} \mathrm{e}^{iqr} X_r, \\ P_q^x &= \frac{1}{\sqrt{2\pi}} \sum_{r=-\infty}^{\infty} \mathrm{e}^{-iqr} P_r^x. \end{aligned} \tag{2.18}$$

Note that here and in the following we use X_r, P_r, r and s to replace q_i^x, p_i^x, i and j, in order to avoid confusion with other terms.

The collective coordinates have to satisfy $Q_q^\dagger = Q_{-q}$ and $P_q^{x\dagger} = P_{-q}^x$, so that the position operators are hermitian. The collective operators also satisfy the continuum commutation relations

$$[Q_q, P_k^x] = i\hbar\delta(q-k). \tag{2.19}$$

The local coordinates can be expressed in terms of the collective operators:

$$\begin{aligned} X_r &= \frac{1}{\sqrt{2\pi}} \int_{-\pi}^{\pi} \mathrm{d}q Q_q \mathrm{e}^{-iqr}, \\ P_r^x &= \frac{1}{\sqrt{2\pi}} \int_{-\pi}^{\pi} \mathrm{d}q P_q^x \mathrm{e}^{iqr}. \end{aligned} \tag{2.20}$$

Substituting the Eq. (2.20) into the Hamiltonian Eq. (2.17), we can get

$$\begin{aligned} H_{vib}^x &= \frac{1}{2} m\omega_x^2 \sum_{r,s} \mathcal{K}_{r,s} X_r X_s + \frac{1}{2m} \sum_r P_r^{x2} \\ &= \frac{1}{2} m\omega_x^2 \int_{-\pi}^{\pi} \int_{-\pi}^{\pi} \mathrm{d}q \mathrm{d}q' Q_q Q_{q'} \frac{1}{2\pi} \sum_{r,s} \mathcal{K}_{r,s} \mathrm{e}^{-iqr-iq's} + \frac{1}{2m} \int_{-\pi}^{\pi} \mathrm{d}q P_q^x P_{-q}^x, \end{aligned} \tag{2.21}$$

where we have used the δ-function

$$\delta(q+q') = \frac{1}{2\pi} \sum_{r=-\infty}^{\infty} \mathrm{e}^{i(q+q')r}. \tag{2.22}$$

The term $\frac{1}{2\pi}\sum_{r,s}\mathcal{K}_{r,s}\mathrm{e}^{-iqr-iq's}$ in Eq. (2.21) can be expressed

$$\begin{aligned}\frac{1}{2\pi}\sum_{r,s}\mathcal{K}_{r,s}\mathrm{e}^{-iqr-iq's} &= \frac{1}{2\pi}\sum_{r,s=-\infty,r\neq s}^{\infty}\beta_x\frac{1}{|r-s|^3}\left[\mathrm{e}^{iq'(r-s)}-1\right]\mathrm{e}^{-i(q+q')r} \\ &\quad+\frac{1}{2\pi}\sum_{r=-\infty}^{\infty}\mathrm{e}^{-i(q+q')r} \\ &= \delta(q+q')+\beta_x\sum_{s=-\infty,s\neq 0}^{\infty}\frac{1}{|s|^3}\left(\mathrm{e}^{-iqs}-1\right)\delta(q+q') \\ &= \delta(q+q')+2\beta_x\sum_{s=1}^{\infty}\frac{\cos(sq)-1}{|s|^3}\delta(q+q'), \qquad (2.23)\end{aligned}$$

where we had ever defined new variables $s'=r-s$ and $r'=r$ to satisfy a δ-function, and $\beta_x \equiv \frac{e^2}{d_0^3}/m\omega_x^2$. The quantity β_x will be in detail discussed later.

Then, substituting Eq. (2.23) into Eq. (2.21), the Hamiltonian takes the following form

$$H_{vib}^x = \int_{-\pi}^{\pi}\mathrm{d}q\left(\frac{1}{2}m\omega_x(q)^2Q_{-q}Q_q+\frac{1}{2m}P_{-q}^xP_q^x\right), \qquad (2.24)$$

where $\omega_x(q)$ is the transverse vibrational mode frequency in the x–direction, and the phonon dispersion relation is given by

$$\omega_x(q)^2=\omega_x^2\left(1+2\beta_x\sum_{s=1}^{\infty}\frac{\cos(sq)-1}{|s|^3}\right). \qquad (2.25)$$

We define the creation and annihilation operators for the continuum of collective modes

$$\begin{aligned}a_q^\dagger &= \left(\frac{\hbar}{2m\omega_x(q)}\right)^{1/2}\left(\frac{m\omega_x(q)}{\hbar}Q_{-q}-\frac{i}{\hbar}P_q^x\right), \\ a_q &= \left(\frac{\hbar}{2m\omega_x(q)}\right)^{1/2}\left(\frac{m\omega_x(q)}{\hbar}Q_q+\frac{i}{\hbar}P_{-q}^x\right).\end{aligned} \qquad (2.26)$$

It can be easily checked that $[a_q,a_k^\dagger]=\delta(q-k)$ is satisfied. The collective coordinate can be expressed in terms of these operators as

$$\begin{aligned}Q_{-q} &= \left(\frac{\hbar}{2m\omega_x(q)}\right)^{1/2}(a_q^\dagger+a_{-q}), \\ P_q^x &= i\left(\frac{m\hbar\omega_x(q)}{2}\right)^{1/2}(a_q^\dagger-a_{-q}).\end{aligned} \qquad (2.27)$$

The Hamiltonian (2.24) is then written as

$$H_{vib}^{x} = \int_{-\pi}^{\pi} \mathrm{d}q \hbar \omega_x(q) \left(a_q^{\dagger} a_q + 1 \right). \tag{2.28}$$

We get the final form for the local coordinate in terms of the creation and annihilation operators

$$X_r = \frac{1}{\sqrt{2\pi}} \int_{-\pi}^{\pi} \mathrm{d}q \left(\frac{\hbar}{2m\omega_x(q)} \right)^{1/2} (a_q^{\dagger} \mathrm{e}^{iqr} + a_q \mathrm{e}^{-iqr}). \tag{2.29}$$

For the case of the longitudinal modes, that describe the motion in the axial direction, one only has to replace $\beta_x \rightarrow -\beta_z$.

On the other hand, the normal modes in finite chain with different distances can be calculated numerically. Assume the length of chain is N.

The matrix $\omega_\alpha^2 \mathcal{K}^\alpha$ in Eq. (2.17) is symmetric, positive definite, and can be decomposed as

$$\mathcal{M} \omega_\alpha^2 \mathcal{K}^\alpha \mathcal{M}^T = \omega_{\alpha,q}^2 \delta_{q,q'}, \tag{2.30}$$

where

$$\mathcal{M} \mathcal{M}^T = \mathcal{M}^T \mathcal{M} = I. \tag{2.31}$$

Define in the x–direction

$$X_r = \sum_{q=1}^{N} \mathcal{M}_{rq} Q_q, \tag{2.32}$$

$$P_r = \sum_{q=1}^{N} \mathcal{M}_{rq} P_q, \tag{2.33}$$

and we get the Hamiltonian

$$H_{vib}^{x} = \sum_{q=1}^{N} \frac{1}{2} \omega_{x,q}^2 Q_q^x + \frac{P_q^x}{2m}. \tag{2.34}$$

Introducing annihilation and creation operators a and $a^\dagger$, we have

$$H_{vib}^{x} = \sum_{q=1}^{N} \hbar \omega_{x,q} (a_q^{\dagger} a_q + 1/2), \tag{2.35}$$

where q refers to the qth normal mode. For a 1D chain of N ions, there are exactly N normal modes and N normal frequencies in each orthogonal direction.

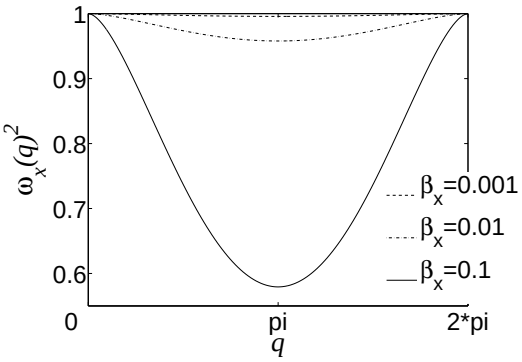

Figure 2.5: The dispersion relation for the transverse vibrational modes of a Coulomb chain. q is from 0 to 2π, and the value of β_x is 0.001, 0.01 and 0.1 from top to bottom. Note that in the figure we use pi to represent π.

Soft limit and stiff limit

We introduce the parameter β_α, which is defined as the ratio between the Coulomb interaction (i.e. spring constant) and the trapping potential in different directions:

$$\beta_\alpha = |c_\alpha| \frac{e^2}{d_0^3} / m\omega_\alpha^2. \tag{2.36}$$

The parameter β_α, indeed, characterizes the normal modes in transverse and longitudinal directions. When $\beta_z \gg 1$, the Coulomb repulsion prevails over the trapping potential and thus they have a strong collective character involving many sites in the axis direction. We call this *soft limit*. When $\beta_{x,y} \ll 1$, on the contrary, the Coulomb interaction is limited between nearest ions only. It represents the local modes (in radial directions) at each ion. We call this *stiff limit*.

We discuss now the dispersion relation $\omega_\alpha(q)$ under some limits, see Eq. (2.25). In Fig. 2.5, we plot $\omega_x(q)^2$ as a function of q when $\beta_x = 0.001, 0.01, 0.1$, respectively. In the limit of $\beta_x \ll 1$ (stiff limit), there is a large energy gap and a small energy dispersion, which is related to optical phonons. With the increase of β_x, the energy gap is decreasing. Obviously, in the limit of $\beta_z \gg 1$ (soft limit), there is a small energy gap and a large energy dispersion, which is related to acoustic phonons.

When $\beta_x \ll 1$ in Eq. (2.25), the Coulomb interaction between ions can be considered as a small perturbation, then we can easily get the effective dipole-dipole spin interaction, see Chapter 4 for details.

In the following chapters, we will use β_α to describe the softness of the Coulomb crystal.

2.3 Ion-laser interaction

In this section we describe the ion-laser interaction [88, 89]. The interaction Hamiltonian decides how to manipulate the ions by the means of lasers and how to create initial states and some special states of the ions. Building a suitable interaction Hamiltonian lies in the heart of quantum simulations. In this thesis our quantum simulators are constructed just by designing the particular interaction Hamiltonians between ions and lasers.

In the electric dipole approximation, the interaction Hamiltonian of a two-level atom with the light field can be written as

$$H_{int} = -\vec{\mu} \cdot \vec{E}(\vec{r}, t), \tag{2.37}$$

where $\vec{\mu} = -e\vec{r}$ is the electric dipole moment,

$$\vec{\mu} = \mu\vec{n}(|e\rangle\langle g| + |g\rangle\langle e|), \tag{2.38}$$

and $\vec{n} = \frac{\vec{\mu}}{\mu}$ is a unit vector along the quantization axis. The electric field $\vec{E}$ is classical, and evaluated at the location $\vec{r}$ of the atomic center of mass within the long-wavelength approximation.

For simplicity we only consider here a single trapped ion interacting with the laser beam, which can be easily extended to a chain of ions. The Hamiltonian of a single ion confined in a harmonic trap reads

$$H_{vib} = \frac{p^2}{2m} + \frac{1}{2}m\omega_{vib}^2 r^2, \tag{2.39}$$

where p and r are the momentum and position operators, and ν is the trapping potential. Introduce the creation and annihilation operators $a^\dagger$ and a,

$$r = \sqrt{\frac{\hbar}{2m\omega_{vib}}}(a^\dagger + a), \quad p = i\sqrt{\frac{\hbar m\omega_{vib}}{2}}(a^\dagger - a), \tag{2.40}$$

then the Hamiltonian can be reexpressed as

$$H_{vib} = \hbar\omega_{vib}a^\dagger a + 1/2. \tag{2.41}$$

2.3.1 The interaction Hamiltonian

We consider two cases of laser configurations along the z-direction perpendicular to the trap axis. One is the traveling wave with the electric field operator

$$\vec{E}_{tw}(z,t) = \frac{1}{2}E_0\vec{\epsilon}\left(\mathrm{e}^{i(kz-\omega_L t)} + \mathrm{e}^{-i(kz-\omega_L t)}\right), \tag{2.42}$$

and the other is the standing wave with the electric field operator

$$\vec{E}_{sw}(z,t) = E_0\vec{\epsilon}\sin(kz+\phi)\left(\mathrm{e}^{-i\omega_L t} + \mathrm{e}^{i\omega_L t}\right). \tag{2.43}$$

Here E_0 is the amplitude of the laser light field, $\vec{\epsilon}$is the unit vector of polarization, $k = 2\pi/\lambda$ is the wave vector, z is the center-of-mass position operator, ω_L is the laser frequency, and tw (sw) represents the traveling (standing) wave for short. ϕ gives the position of the ion (center of the trap) in the laser standing wave, e.g. $\phi = 0$ at the node, $\phi = \frac{\pi}{2}$ at the antinode.

The Hamiltonian of a two-level atom in a classical traveling (standing) wave field reads

$$H_{tw} = \hbar\frac{\omega_{eg}}{2}\sigma^z - \hbar\frac{\Omega}{2}\left(\mathrm{e}^{i(kz-\omega_L t)} + \mathrm{e}^{-i(kz-\omega_L t)}\right)(\sigma^+ + \sigma^-), \tag{2.44}$$

$$H_{sw} = \hbar\frac{\omega_{eg}}{2}\sigma^z - \hbar\frac{\Omega}{2}\sin(kz+\phi)\left(\mathrm{e}^{-i\omega_L t} + \mathrm{e}^{i\omega_L t}\right)(\sigma^+ + \sigma^-), \tag{2.45}$$

where Ω is the Rabi frequency defined by

$$\Omega \equiv \frac{eE_0}{\hbar}\langle e|\vec{\epsilon}\cdot\vec{\mu}|g\rangle \qquad \text{(traveling wave)}, \tag{2.46}$$

$$\Omega \equiv \frac{2eE_0}{\hbar}\langle e|\vec{\epsilon}\cdot\vec{\mu}|g\rangle \qquad \text{(standing wave)}. \tag{2.47}$$

The laser detuning from the atomic resonance is $\delta\omega \equiv \omega_L - \omega_{eg}$, then the Hamiltonian can be written in the form:

$$H_{tw} = \hbar\frac{\omega_L}{2}\sigma^z - \hbar\frac{\delta\omega}{2}\sigma^z - \hbar\frac{\Omega}{2}\left(\mathrm{e}^{i(kz-\omega_L t)} + \mathrm{e}^{-i(kz-\omega_L t)}\right)(\sigma^+ + \sigma^-), \tag{2.48}$$

$$H_{sw} = \hbar\frac{\omega_L}{2}\sigma^z - \hbar\frac{\delta\omega}{2}\sigma^z - \hbar\frac{\Omega}{2}\sin(kz+\phi)\left(\mathrm{e}^{-i\omega_L t} + \mathrm{e}^{i\omega_L t}\right)(\sigma^+ + \sigma^-). \tag{2.49}$$

In a frame, which is rotating with the laser frequency ω_L, we have the Hamiltonian in the interaction picture after making the rotating-wave approximation (RWA)

$$H^I_{tw} = -\hbar\frac{\delta\omega}{2}\sigma^z - \hbar\frac{\Omega}{2}(\mathrm{e}^{ikz}\sigma^+ + \mathrm{e}^{-ikz}\sigma^-), \tag{2.50}$$

$$H^I_{sw} = -\hbar\frac{\delta\omega}{2}\sigma^z - \hbar\frac{\Omega}{2}\sin(kz+\phi)(\sigma^+ + \sigma^-). \tag{2.51}$$

The interaction Hamiltonian describes the excitation of the electron by the laser field evaluated at the center-of-mass position z of the ion.

2.3.2 Lamb-Dicke limit

In general, the theoretical analysis of the ion-laser interaction is very complicated. However, it can be simplified greatly under some conditions, such as in the Lamb-Dicke limit [90], which is also the typical situation in linear Paul traps. In this subsection we will describe a single ion interacting with lasers in this Lamb-Dicke limit[2].

First we introduce the Lamb-Dicke parameter, which is defined by

$$\eta = \frac{2\pi a_0}{\lambda}, \tag{2.52}$$

where a_0 is the size of the ground state of the harmonic potential, i.e.

$$a_0 = \sqrt{\frac{\hbar}{2m\omega_{vib}}}, \tag{2.53}$$

and λ is the wavelength of the laser light exciting a given transition.

When $\eta \ll 1$, the motion of the ion is restricted in a tight trap, whose region is much smaller than the wavelength of the laser light. We call this the Lamb-Dicke limit, which allows us to expand the interaction Hamiltonian in terms of the Lamb-Dicke parameter.

Here we give the Lamb-Dicke expansions of e^{ikz} and $\sin(kz+\phi)$ in Eqs. (2.50) and (2.51), respectively:

$$\begin{aligned} \mathrm{e}^{ikz} &= \mathrm{e}^{i\eta(a+a^\dagger)} = 1 + i\eta(a+a^\dagger) + \mathcal{O}(\eta^2), && (2.54)\\ \sin(kz+\phi) &= \sin[\eta(a+a^\dagger)]\cos\phi + \cos[\eta(a+a^\dagger)]\sin\phi \\ &= \sin(\phi) + \eta\cos(\phi)(a+a^\dagger) + \mathcal{O}(\eta^2). && (2.55) \end{aligned}$$

Substituting Eq. (2.54) and (2.55) directly into the Hamiltonians (2.50) and (2.51), respectively, we get

$$H^I_{tw} = -\hbar\frac{\delta\omega}{2}\sigma^z - \hbar\frac{\Omega}{2}\left\{[1+i\eta(a+a^\dagger)]\sigma^+ + [1-i\eta(a+a^\dagger)]\sigma^-\right\}, \tag{2.56}$$

$$H^I_{sw} = -\hbar\frac{\delta\omega}{2}\sigma^z - \hbar\frac{\Omega}{2}[\sin(\phi) + \eta\cos(\phi)(a+a^\dagger)](\sigma^+ + \sigma^-). \tag{2.57}$$

[2]Some parts in this subsection are based on the reference by J. I. Cirac *et al* [90] and the lecture by P. Zoller [91].

The above Eqs. (2.56) and (2.57) can be further simplified under certain conditions. In the following we discuss three most important cases of Eq. (2.56) for the traveling wave. Before discussing, we denote $|g\rangle|n\rangle$ ($|e\rangle|n\rangle$) the state of the single ion where $|n\rangle$ is the Fock state of the harmonic oscillator.

1. When the laser is close to the resonance with the atom transition $\delta\omega \approx 0$, $\delta\omega \ll \omega_{vib}$, the varies of the harmonic oscillator quantum number n can be neglected due to their off-resonance. Thus, it will excite $|g\rangle|n\rangle \rightarrow |e\rangle|n\rangle$. In this case, the Hamiltonian is approximately reduced to

$$H = -\hbar\frac{\delta\omega}{2}\sigma^z - \hbar\frac{\Omega}{2}\left(\sigma^+ + \sigma^-\right). \tag{2.58}$$

2. When the laser is tuned to close to the lower motional sideband (red sideband) resonance $\delta\omega \approx -\omega_{vib}$, only transitions decreasing one phonon are important. Thus, it will excite $|g\rangle|n\rangle \rightarrow |e\rangle|n-1\rangle$, where the Hamiltonian in the RWA is of the Jaynes-Cummings type:

$$H = -\hbar\frac{\delta\omega}{2}\sigma^z - \eta\hbar\frac{\Omega}{2}\left(i\sigma^+ a + (-i)\sigma^- a^\dagger\right). \tag{2.59}$$

3. When the laser is tuned close to the upper motional sideband (blue sideband) resonance $\delta\omega \approx +\omega_{vib}$, only transitions increasing one phonon are important. Thus, it will excite $|g\rangle|n\rangle \rightarrow |e\rangle|n+1\rangle$. In this case the Hamiltonian in RWA is of the anti-Jaynes-Cummings type:

$$H = -\hbar\frac{\delta\omega}{2}\sigma^z - \eta\hbar\frac{\Omega}{2}\left(i\sigma^+ a^\dagger + (-i)\sigma^- a\right). \tag{2.60}$$

To make the above approximations valid, the effective Rabi frequency have to be much smaller than the trapping frequency. To fully describe single trapped ions in a harmonic trap potential, one will add the free motion Hamiltonian to the Eqs. (2.58), (2.59) and (2.60). According to these three limiting Hamiltonians, one can create and manipulate quantum motion states of ions using lasers. In the following section we will discuss in detail how to engineer some of quantum states. Actually this control of states largely depends on how to perform approximations for the real Hamiltonian under certain conditions. Then, new Hamiltonians could be designed under certain different conditions, in order to produce interesting quantum states.

2.3.3 State-dependent force

Relating to the work of effective quantum spin systems with trapped ions in Chapter 4, we will consider an ion in a far-detuned standing wave in this subsection. We assume that the ion have two internal ground hyperfine levels, denoted the qubit (spin) states $|g\rangle$ and $|e\rangle$, and an auxiliary higher energy level $|p\rangle$, see Fig. 2.6 for the energy level structure and the optical transition. A standing-wave light is far-detuned from the third, excited energy level $|p\rangle$ of the ion, with the detuning $\delta\omega$. This off-resonant light will produce an optical dipole force on the ion [2, 56]. The force depends on the position variable z along the trap axis, and on the qubit (spin) state of the ion $|e\rangle$. If the ion is in the state $|e\rangle$, the laser will push the ion along the propagating direction. We call it a state-dependent force.

Starting from Eq. (2.51), we write the Hamiltonian as

$$H_{sw}^{I} = -\hbar\frac{\delta\omega}{2}\sigma^{z} - \hbar\frac{\Omega}{2}\sin(kz+\phi)\sigma^{x}. \tag{2.61}$$

In the limit of large detuning ($\delta\omega \gg \Omega\sin(kz+\phi)$), diagonalizing this Hamiltonian, we can get [89]

$$H \approx -\frac{\hbar}{2}\sqrt{\delta\omega^{2}+\Omega^{2}\sin^{2}(kz+\phi)}\sigma^{z}. \tag{2.62}$$

Further it leads to the effective Hamiltonian

$$H_{eff} = \pm\hbar\frac{\delta\omega}{2}\sigma^{z} - \hbar\left(\frac{\Omega^{2}\sin^{2}(kz+\phi)}{4\delta\omega}\right)\sigma^{z}, \quad (\delta\omega \lessgtr 0). \tag{2.63}$$

The solution shows that the atomic levels are shifted, i.e. a.c. Stark shift. The shifted energies due to the large frequency detuning are

$$\Delta E_{e,p}(z) = \pm\frac{\hbar[\Omega\sin(kz+\phi)]^{2}}{4\delta\omega} \tag{2.64}$$

for the ground and excited state[3].

[3]In another way, the effect of far-detuned laser on the atomic levels can also be treated as a perturbation in second order of the electric field.In the second order time-independent perturbation theory for non-degenerate states, an interaction H_1 leads to an energy shift of the i-th state, which is given by

$$\Delta E_{i} = \sum_{j\neq i}\frac{|\langle j|H_{1}|i\rangle|^{2}}{\varepsilon_{i}-\varepsilon_{j}}. \tag{2.65}$$

For a two-level atom, the interaction is $H_1 = -\mu E$, and the general result (2.65) right simplifies to Eq. (2.64).

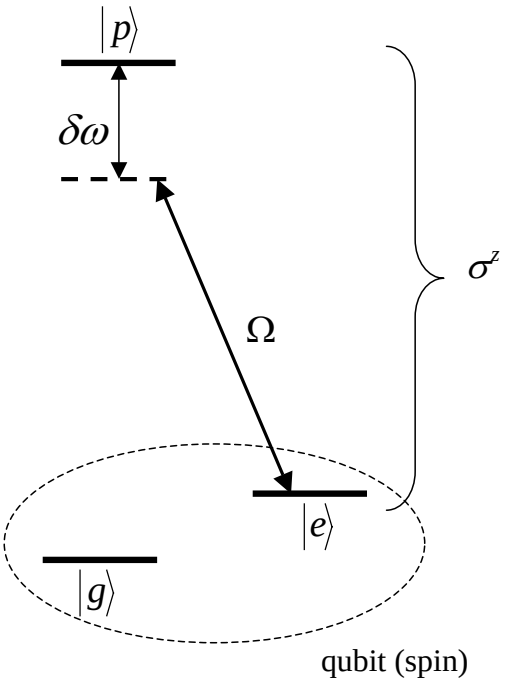

Figure 2.6: The three-level ion in a far-detuned standing-wave light. $|g\rangle$ and $|e\rangle$ are the internal ground hyperfine states, and $|p\rangle$ is an auxiliary excited state. The laser is detuned from the excited state $|p\rangle$ with the detuning $\delta\omega$. Ω is the Rabi frequency of the laser. Choosing the relative phase of the laser, one can make that $|g\rangle$ is dark and $|e\rangle$ is bright with respect to the laser. Then the ion will experience a force if it is in the state $|e\rangle$. Note that σ^z in this subsection refers to the two levels $|e\rangle$ and $|p\rangle$.

The light shifts are spatially dependent due to the inhomogeneity of the standing wave. This gradient of energy would result in the dipole force on the ion. The force F on an atom is defined as the expectation value of the quantum mechanical operator $\mathcal{F}$, i.e.

$$F = \langle \mathcal{F} \rangle = \langle \dot{p} \rangle = -\left\langle \frac{\partial H}{\partial z} \right\rangle. \tag{2.66}$$

We define $\Omega' = \Omega \sin(kz + \phi)$. Substituting Eq. (2.63) into Eq. (2.66) gets

$$F = \frac{\hbar\Omega'}{2\delta\omega}\frac{\partial\Omega'}{\partial z}\sigma^z \equiv f \cdot \sigma^z, \tag{2.67}$$

where $f \equiv \frac{\hbar\Omega'}{2\delta\omega}\frac{\partial\Omega'}{\partial z}$, and it depends on $\delta\omega$, Ω' and the first derivative of Ω'. Since the light field is far-detuned from the resonance between $|e\rangle$ and

$|p\rangle$, the upper electronic state $|p\rangle$ remains largely unoccupied, and can be adiabatically eliminated. Then the force (2.67) becomes

$$F = -f \cdot |e\rangle\langle e|. \tag{2.68}$$

The interaction Hamiltonian in a Tayler series can be written as

$$H_{eff} = (H_{eff})_{z=0} + \left(\frac{\partial H_{eff}}{\partial z}\right)_{z=0} z + \cdots, \tag{2.69}$$

where $\left(\frac{\partial H_{eff}}{\partial z}\right)_{z=0} = \frac{\hbar\Omega^2 k}{4\delta\omega}\sin(2\phi)\sigma^z$ is just the force. This force allows to couple the qubit (spin) states of the ions to the vibrational modes (Note that z is the position operator in Eq. 2.69). It not only plays a most important role in the pushing gate of quantum computation [56], but is also a staring point of our proposals [72, 75]. We will meet it again in the next chapters.

2.4 Engineering of quantum states

In experiments of ion traps, one can control optimally the evolution of internal states and quantum motion states, such as Fock states, coherent states, squeezed states and Schödinger cat states. These states are of interest from the point view of quantum measurement and quantum computation. Controlling successfully these states is the first step of performing quantum computing and quantum simulation.

In this section we will review how to prepare and detect internal states and Fock states in ion-trap experiments, based on the work by D. M. Meekhof *et al* [60]. These states are just the basic ingredients in our proposals of realizing quantum spin models and the Bose-Hubbard model in ion traps[4]. The details of generating, manipulating and detecting quantum motion states in ion traps can be found in the reviews by D. J. Wineland *et al* [44], and by D. Leibfried *et al* [47].

2.4.1 Preparation and detection of internal states

The preparation of the ion's internal states could be achieved via optical pumping techniques, whose fidelity could approach 1. Whenever the ion is in a state different to the desired state, e.g. $|g\rangle$, it can, via appropriately optical pumping, absorb a photon and decay into another state until it finally

[4]Note that quantum analogue should be reached under the current or very near future experiments.

reaches the desired state. The detection of internal states is accomplished by light scattering, and is also of high efficiency. One apply an appropriately polarized laser beam to the ion, and tune it to a transition, which will scatter many photons if the atom is in one internal state, e.g. $|g\rangle$, but will scatter essentially no photons if the atom is in the other internal state, e.g. $|e\rangle$. If a modest number of these photons are detected, the efficiency of detection could be 100%, to distinguish these different states.

In the experiment of D. M. Meekhof *et al* [60], they focused on the ion $^9Be^+$. The relevant level structure of $^9Be^+$ is shown in Fig. 2.7 [92]. The two-level systems one is interested in is formed by the two hyperfine levels of the ground state $|2s\ ^2S_{1/2}; F = 2, M_F = 2\rangle$ and $|2s\ ^2S_{1/2}; F = 1, M_F = 1\rangle$, which are denoted the qubit (spin) states $|g\rangle$ and $|e\rangle$, respectively. These two levels are separated by the hyperfine splitting of $\omega_0/2\pi = 1.25$GHz in the experiments, where ω_0 is defined as the total splitting between $|g\rangle$ and $|e\rangle$. The splitting between the $2p$ levels is approximately 197GHz. The single-photon optical transitions driven by D1, D2 and D3 are cycling transition (internal-state detecting), Doppler cooling and optical pumping, respectively. The laser beams R1 and R2 drive two-photon Raman transitions, which couple $|g\rangle$ and $|e\rangle$ through the level $2p\ ^2P_{1/2}$ ($\Delta/2\pi = 40$GHz). All optical transitions between the $2p$ excited states and the $2s$ ground states are near $\lambda = 313$nm, where λ is the laser wavelength. In addition, the motional states for $|g\rangle$ and $|e\rangle$ are omitted in Fig. 2.7 for clarity and simplicity.

First, we consider how to prepare the ion into the state $|g\rangle$. We apply the laser beam D2 to drive the transition $|e\rangle \rightarrow |2p\ ^2P_{3/2}; F = 3, M_F = 2\rangle$, which is a non-circling transition. From the excite state $2p\ ^2P_{3/2}$ the ion can decay back into $|e\rangle$, $|g\rangle$, or $|2s\ ^2S_{1/2}; F = 2, M_F = 1\rangle$. If the ion is in the state $|2s\ ^2S_{1/2}; F = 2, M_F = 1\rangle$, we have to re-pump the ion back into the qubit states $|g\rangle$ or $|e\rangle$. We apply the laser D3 resonant with the transition $|2s\ ^2S_{1/2}; F = 2, M_F = 1\rangle \rightarrow |2p\ ^2P_{1/2}; F = 2, M_F = 2\rangle$, which could empty population out of the level $|2s\ ^2S_{1/2}; F = 2, M_F = 1\rangle$. If D1 and D3 are turned on together (D1 is a cycling transition beam, which will be discussed in the following), the ion is finally optically pumped into $|g\rangle$. Usually, the state of the ion is prepared at the beginning of experiments. $|e\rangle$ is prepared from $|g\rangle$ using a π–pulse Raman transition.

Then, we talk about how to detect the state $|g\rangle$. D1 is a cycling transition beam. If the ion is in $|g\rangle$ and a circularly σ^+–polarized laser (i.e. D1) is applied, the ion repeatly cycles between $|g\rangle$ and the excited state $|2p\ ^2P_{3/2}; F = 3, M_F = 3\rangle$, spontaneously emitting a photon each time. Then there will be continuous photon-scattering if the ion is in the state $|g\rangle$, but no photon-scattering in the state $|e\rangle$. Detect the fluorescence photons, and

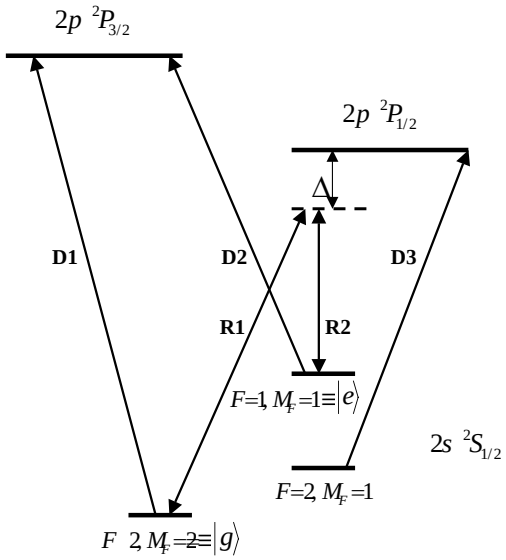

Figure 2.7: Relevant energy levels of ^{9}Be and the corresponding optical transitions. The hyperfine levels $|2s\ ^2S_{1/2}; F = 2, M_F = 2\rangle$ and $|2s\ ^2S_{1/2}; F = 1, M_F = 1\rangle$ of the $2s\ 2S_{1/2}$ ground state are denoted the qubit (spin) states $|g\rangle$ and $|e\rangle$, respectively. The laser beams D1, D2 and D3 are for internal-state detecting, Doppler cooling and optical pumping, respectively. R1 and R2 are Raman beams, which couple $|g\rangle$ and $|e\rangle$ through the level $2p\ ^2P_{1/2}$ ($\Delta/2\pi = 40$GHz). The motional state levels are spaced by 10MHz, but omitted here for clarity.

get the average signal, which is proportional to $P_g(t)$, where $P_g(t)$ is defined as the probability of finding the ion in the state $|g\rangle$. This detection efficiency is near 100%.

2.4.2 Preparation and detection of Fock states

There have been several proposals about how to create Fock (number) states of trapped ion's motion, such as using quantum jumps and adiabatic passage. In experiments, however, one only used a simple technique involving multiple π pulses to create a series of Fock states [60]. Here we outline briefly the procedure of how to create Fock states.

The starting point is a pure state, e.g. the ground state of motion $|0\rangle$, which can be achieved by laser cooling. We also assume that the ion occupy the internal ground state $|g\rangle$, which can be prepared by using standard optical pumping techniques, see the subsection 2.4.1. The initial state of the ion is

thus $|g\rangle|0\rangle$.

1. $|g\rangle|0\rangle \rightarrow |e\rangle|1\rangle$ by a blue sideband π–pulse
   First, one applies a π pulse laser on the first blue sideband of the ion. According to Eq. (2.60), we see that the ion flips from $|g\rangle|0\rangle$ into $|e\rangle|1\rangle$. The Fock state $|1\rangle$ is created.

2. $|e\rangle|1\rangle \rightarrow |g\rangle|2\rangle$ by a red sideband π–pulse
   Second, one applies a π pulse on the first red sideband of the ion. According to Eq. (2.59), the ion flips from $|e\rangle|1\rangle$ into $|g\rangle|2\rangle$. The Fock state $|2\rangle$ is created.

3. $|g\rangle(|e\rangle)|n-1\rangle \rightarrow |e\rangle(|g\rangle)|n\rangle$ by a series of blue (red) sideband π–pulses
   In the end, higher Fock states $|n\rangle$ can be created in a similar manner by applying a sequence of π pulses on the blue, or red sideband. Note that if the light is not a π pulse, i.e. for some other times t, the entangled states will be created.

After producing these quantum motional states, one needs to measure them. According to Eqs. (2.59) and (2.60), we know that the internal state transition depends on the changing of vibrational modes. In general, the internal states and vibrational modes are entangled. One can map the motional state of the ion onto its internal state, to get the information of motion by measuring the internal state. This mapping is straightforward in the resolved sideband regime. Same as the internal-state detection, this method also gives high efficiency.

In the Lamb-Dicke limit, we consider the first blue sidebands, which is useful to get the number-state distribution of various states of motion. Assume the initial state of an ion is

$$|\Psi(0)\rangle = |g\rangle|n\rangle. \tag{2.70}$$

Applying a laser on the blue sideband of the ion for a time t, the state of the ion is

$$|\Psi(t)\rangle = \cos(\frac{\Omega}{2}\sqrt{n+1}\eta t)|g\rangle|n\rangle + \sin(\frac{\Omega}{2}\sqrt{n+1}\eta t)|e\rangle|n+1\rangle. \tag{2.71}$$

The probability of finding the ion in the ground state after the interaction is

$$\begin{aligned} P_g(t) &= \langle\Psi(t)|(|g\rangle\langle g| \times I_{vib})|\Psi(t)\rangle & (2.72)\\ &= \cos^2(\frac{\Omega}{2}\sqrt{n+1}\eta t) = \frac{1}{2}\left[1+\cos(\Omega\sqrt{n+1}\eta t)\right], & (2.73) \end{aligned}$$

where I_{vib} is the identity matrix of vibrational modes. From the frequency of $P_g(t)$, one can get the initial value of n. The experiment is repeated many times to get the average of the value.

Extend the initial state of the ion to

$$|\Psi(0)\rangle = |g\rangle \sum_{n=0}^{\infty} c_n |n\rangle. \tag{2.74}$$

Similarly, we can get

$$P_g(t) = \frac{1}{2}\left[1 + \sum_{n=0}^{\infty} P_n \cos\left(\Omega\sqrt{(n+1)}\eta t\right)\right], \tag{2.75}$$

where $P_n = |c_n|^2$ is the probability of finding the ion in the number state $|n\rangle$. After the Fourier transform of Eq. (2.75), we can obtain the occupation P_n of number states $|n\rangle$.

For the complete determination of the quantum state of motion, one needs to reconstruct the density matrix or the Wigner function of the quantum state of motion. This topic can be found in Refs. [47] and [93]. In this thesis, we do not further discuss this topic.

2.5 Conclusions

In this chapter we review the internal states and vibrational modes of trapped ions, the ion-laser interactions and how to engineer quantum states of ions. All of these are closely related to our further study in this thesis. Based on these knowledge, we will talk about, in the following chapters, how to make use of the internal states (considered as *spins*) and vibrational modes (considered as *phonons*) of trapped ions interacting with lasers, to simulate quantum spin models and Bose-Hubbard models under certain conditions.

Chapter 3

Density Matrix Renormalization Group

The density matrix renormalization group (DMRG) [76, 77] is a quasi-exact numerical technique for finding an efficient approximation of the ground state in strongly correlated systems. Since its original formulation by S. White in 1992 [76], the DMRG algorithm has become the most important method in studying low dimensional quantum systems. It has been applied to spin chains and ladders, fermionic and bosonic systems, disordered models, impurities and molecules, 2D electrons in high magnetic fields, and so on. The extensive reviews on DMRG can be found in the references [94], [95] and [96]. In addition, with the development of quantum information theory in recent years, there come up the extensions [97,98,99,100,101,102] of the DMRG under the formalism of Matrix Product state (MPS) [103, 104]. More recently, the efficient time-dependent DMRG is also being developed [105, 106, 107], which could be used to study dynamic properties of the ultracold atoms.

This chapter gives a description of the main method–the DMRG, that was used extensively in my studies. First we review the DMRG in a general scheme. Then the outline of our algorithms is described and illustrated. Our algorithms are built for long-range interacting (hopping) models. Third, we talk about how to actualize the operators and correlations at each step in the DMRG. In the end, we discuss how to improve the efficiency of the DMRG algorithms. Our DMRG method is restricted to the ground state of the system, that is, we only consider static properties at zero temperature.

3.1 The density-matrix projection

When one numerically studies strongly correlated lattice systems (there are very few systems which could be exactly solved), e.g. the Heisenberg model or the Hubbard model [86], the amount of states grows exponentially with the system size. Then, one has to reduce the size of the Hilbert space to be able to deal with larger systems. In such a way, there have been several numerical methods, such as Monte Carlo [108], renormalization group [109] and DMRG [76]. Each of these methods considers a particular criterion of keeping the relevant information when reducing the Hilbert space.

The basic idea behind the DMRG is to optimize iteratively the basis states of the system through a truncation procedure called the *density matrix projection*. With enlarging the system, the corresponding Hilbert space is truncated systematically by keeping the most important basis states describing the ground state. Such relevant basis states are right obtained from the reduced density matrix of the system. In the following we give more details of this procedure.

To begin with, we consider a 1D quantum lattice chain of length N, e.g. a 1D quantum Ising chain. This chain is called the *superblock* in DMRG language, and divided into three parts: the *left block*, the *single site* and the *right block* (see Fig. 3.1 for the configuration). Here we use $[\mathbf{B_L}]$, $[\bullet]$ and $[\mathbf{B_R}]$ to represent the left block, the single site and the right block, respectively. Note that in the original scheme of the DMRG formulated by Stephen White, he used the configuration consisting of two blocks and two sites. But here, considering long-range interactions in our inhomogeneous system, the configuration in Fig. 3.1 will be more simple and useful.

Assume that the left block contains M lattice sites in the basis $\{|\alpha_L\rangle\}$ spanning a D-dimensional Hilbert space, and without loss of generality, the right block has also M lattice sites in the basis $\{|\alpha_R\rangle\}$ spanning a D–dimensional Hilbert space. d is the dimension of the Hilbert space at the single site with the local basis $\{|S\rangle\}$. The left block tensoring the single site constructs the so called *system* in the product basis $\{|\alpha_L S\rangle\}$ with $D\cdot d$ states, and the right block the *environment*.

The ground state $|\Psi\rangle$ of the superblock is represented in terms of the basis states $|\alpha_L\rangle$, $|S\rangle$ and $|\alpha_R\rangle$:

$$|\Psi\rangle = \sum_{\alpha_L,S,\alpha_R} \Psi_{\alpha_L S\alpha_R}|\alpha_L\rangle|S\rangle|\alpha_R\rangle. \tag{3.1}$$

The reduced density matrix ρ for the *system* is obtained by tracing over the

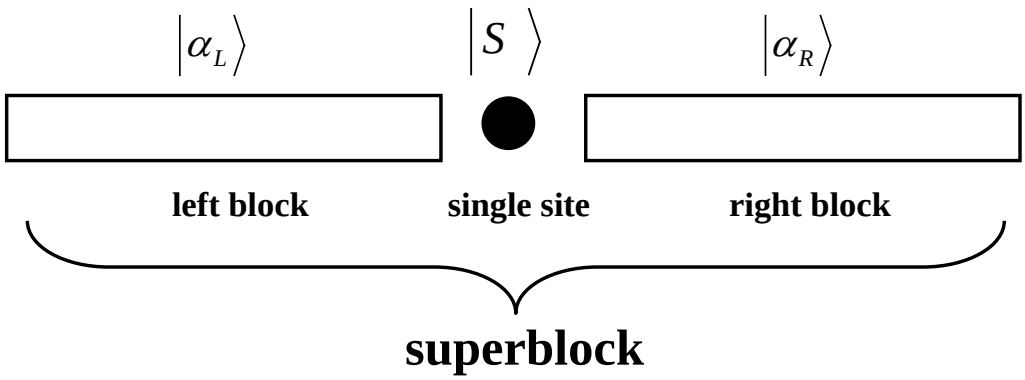

Figure 3.1: The superblock configuration in our DMRG method, which consists of a left block, a single site and a right block. The basis states of the left block, the single site and the right block are $|\alpha_L\rangle$, $|S\rangle$ and $|\alpha_R\rangle$, respectively. The left block and the single site constitute the so called *system*, and the right block is called the *environment*.

environment:

$$\rho = \mathrm{tr}_E |\Psi\rangle\langle\Psi|. \tag{3.2}$$

In the basis $\{|\alpha_L S\rangle\}$, it can be written as

$$\rho = \sum_{\alpha_L S, \tilde{\alpha}_L \tilde{S}, \alpha_R} \Psi^*_{\alpha_L S \alpha_R} \Psi_{\tilde{\alpha}_L \tilde{S} \alpha_R} |\alpha_L S\rangle\langle\tilde{\alpha}_L \tilde{S}|. \tag{3.3}$$

The reduced density matrix contains all the information needed to calculate the properties of the *system*. For instance, the expectation of an operator O acting on the *system* is given by $\langle O\rangle = \mathrm{tr}\{\rho O\}$. The norm of the wavefunction is $\langle\Psi|\Psi\rangle = \mathrm{tr}\rho = 1$.

The *system* is in a product basis $\{|\alpha_L S\rangle\}$ with $D \cdot d$ states, and no truncation takes place up to now. Our aim in the DMRG is to find a small set of new basis $\{|\beta\rangle_L\}$ with m states ($m < D \cdot d$), which should represent effectively the *system* in the product basis $\{|\alpha_L S\rangle\}$. Indeed, we will see below that $\{|\beta\rangle_L\}$ with D states are the only eigenvectors of the reduced density matrix ρ. The basis $\{|\beta\rangle_L\}$ with D states is right the optimal representation of the *system*.

The elements $\Psi_{\alpha_L S \alpha_R}$ can be thought of as a matrix Ψ of dimension $((D \cdot d) \times D)$. Then the matrix Ψ can be written in a *singular value decom-*

position(SVD)[1] as:

$$\Psi = U\Xi V^\dagger, \tag{3.4}$$

where U is a $(D \cdot d) \times D$ matrix with orthonormal columns, Ξ is a $D \times D$ diagonal matrix with positive entries Ξ_β, and $(V^\dagger)$ is a $D \times D$ unitary matrix. That is

$$\Psi_{\alpha_L S,\alpha_R} = \sum_\beta U_{\alpha_L S,\beta}\Xi_\beta (V^\dagger)_{\beta\alpha_R}. \tag{3.5}$$

Substituting Eq. (3.5) into Eq. (3.1), we get

$$\begin{aligned} |\Psi\rangle &= \sum_\beta \Xi_\beta \underbrace{\left(\sum_{\alpha_L S} U_{\alpha^L S,\beta}|\alpha_L\rangle|S\rangle\right)}_{|\beta\rangle_L} \underbrace{\left(\sum_{\alpha_R} V^*_{\alpha_R\beta}|\alpha_R\rangle\right)}_{|\beta\rangle_R} \\ &= \sum_\beta \Xi_\beta |\beta\rangle_L |\beta\rangle_R, \end{aligned} \tag{3.6}$$

where we have defined new bases

$$|\beta\rangle_L = \sum_{\alpha_L S} U_{\alpha_L S,\beta}|\alpha_L\rangle|S\rangle, \tag{3.7}$$

$$|\beta\rangle_R = \sum_{\alpha_R} V^*_{\alpha_R\beta}|\alpha_R\rangle. \tag{3.8}$$

Here $\{|\beta\rangle_L\}$ and $\{|\beta\rangle_R\}$ have the same number of states D, and form the orthonormal bases for the *system* and *environment*, respectively. Indeed, the Eq. (3.6) is just the Schmidt decomposition[2] of the wave function.

[1]Suppose M is an $m \times n$ real or complex matrix, then M can be factorized in the form $M = U\Xi V^\dagger$, where U is an $m \times m$ unitary matrix, Ξ is an $m \times n$ diagonal matrix, and V is an $n \times n$ unitary matrix. Such a factorization is called a *singular value decomposition* [110]. Generally, $MM^\dagger = U(\Xi\Xi^\dagger)U^\dagger$ and $M^\dagger M = V(\Xi^\dagger\Xi)V^\dagger$.

[2]The Schmidt decomposition [48, 111] shows that any state of two subsystem A and B can be written as

$$|\Psi_{AB}\rangle = \sum_{i=1} c_i |u_i\rangle|v_i\rangle, \tag{3.9}$$

where $\{|u_i\rangle\}$ is a orthonormal basis for subsystem A, $\{|v_i\rangle\}$ is a orthonormal basis for subsystem B, and c_i are non-negative real numbers satisfying $\sum_i c_i = 1$. The reduced density matrices of both subsystems, written in the Schmidt basis, are diagonal and have the same positive spectrum, e.g. see Eq. 3.10.

The reduced density matrix of the *system* in the new basis $\{|\beta\rangle_L\}$ is then given by

$$\rho = \mathrm{tr}_E(|\Psi\rangle\langle\Psi|) = \sum_\beta \Xi_\beta^2 |\beta\rangle_L \langle\beta|_L, \tag{3.10}$$

which shows that $\{|\beta\rangle_L\}$ are the eigenvectors, and Ξ_β are the square roots of the eigenvalues of ρ.

After being performed the Schmidt Decomposition, the *system* is changed onto the basis $\{|\beta\rangle_L\}$ from $\{|\alpha_L S\rangle\}$. Its Hilbert space is truncated from $D \cdot d$ dimensions to D dimensions, where $D < D \cdot d$. The matrix $U_{\alpha_L S,\beta}$ (we think of it as a matrix) is the projector which realize the projection from the basis $\{|\alpha_L S\rangle\}$ with $D \cdot d$ states to the basis $\{|\beta\rangle_L\}$ with D states. Note that here the dimension of Hilbert space of the *environment* keep unchanged.

Therefore, we can get the optimal basis $\{|\beta\rangle_L\}$ and the projection operator $U_{\alpha_L S,\beta}$ using the SVD of the wavefunction in the configuration $[\mathbf{B_L} \bullet \mathbf{B_R}]$. Then the dimension of the Hilbert space can be truncated from $D \cdot d$ to D without loss of non-zero eigenvalues of the density matrix[3].

3.2 The DMRG algorithms

According to the truncation techniques mentioned in the Section 3.1, we will now enlarge linearly the *system* to a large size. At each iteration, the left block is increased by a single site, and projected onto a truncated basis. There are two algorithms: the infinite system algorithm and the finite system algorithm [77]. The finite system algorithm is based on the infinite system algorithm, and improves the accuracy of results largely. In general, one uses the infinite system algorithm at the first steps to build the system up to a finite length, then turns to the finite size method to increase the accuracy of the results.

3.2.1 The infinite system algorithm

We describe the infinite system algorithm in this subsection. We start from a small chain, for instance, the left block and the right block both contain 2 lattice sites, and the length of the chain is $N = 5$ including the single site. Then the left block (its size) is increased iteratively by adding a site to it at each step and form a new left block. Correspondingly, the single site

[3]Indeed, performing a singular value decomposition is equivalent to diagonalizing a density matrix. We can also diagonalize the density matrix (not using the SVD), and keep the eigenvectors with non-zero eigenvalues as the truncated basis.

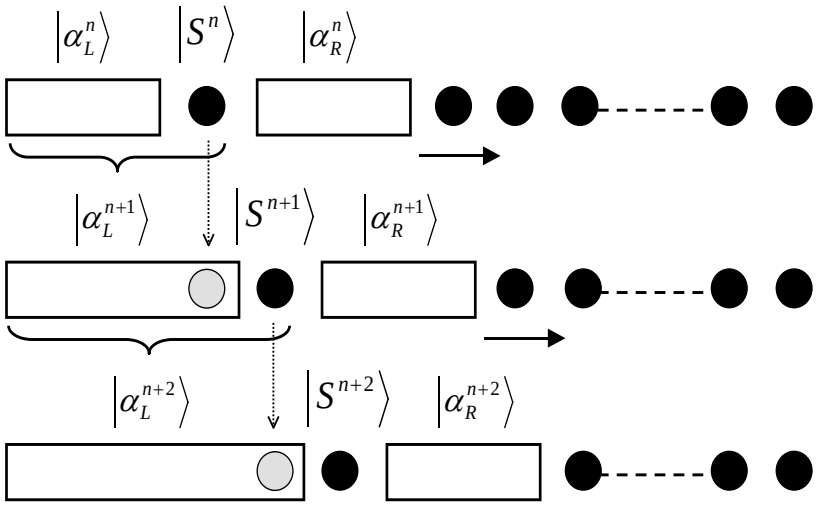

Figure 3.2: The pictorial description of the infinite system algorithm of the DMRG. The left block is growing linearly from the nth step to the $(n+1)$th and further the $(n+2)$th step. $|\alpha_L^n\rangle$, $|S^n\rangle$ and $|\alpha_R^n\rangle$ are the basis states at the nth step.

and the right block is shifted towards the right direction by a site. At each step, the new left block is projected onto a new truncated basis. The general procedure is schematically shown in Fig. 3.2. The left block is increased linearly from the nth step to the $(n+2)$th step, where $|\alpha_L^n\rangle$, $|S^n\rangle$ and $|\alpha_R^n\rangle$ are the basis states of the left block $[\mathbf{B_L^n}]$, single site $[\bullet]$ and right block $\mathbf{B_R^n}]$ at the nth step, respectively. The algorithm proceeds as follows:

1. Construct a small superblock with $2M+1$ lattice sites, i.e. $[\mathbf{B_L^n} \bullet \mathbf{B_R^n}]$ (n=1). The number of states is D, d and D for the left block, single site and right block, respectively. The superblock is small enough to be exactly diagonalized.

2. Diagonalize the superblock Hamiltonian H, obtaining the ground state wavefunction $|\Psi\rangle$.

3. Perform the SVD on the matrix Ψ, i.e. $\Psi = U\Xi V^\dagger$, obtaining the projector U, and the new basis $\{|\beta\rangle_L\}$ with D states. Define $|\alpha_L^{n+1}\rangle \equiv |\beta_L\rangle$ as the new basis for convenience and consistence.

4. Project the operators O_i (including the Hamiltonians) in the *system* $[\mathbf{B_L^n}\bullet]$, from the basis $|\alpha_L^n S^n\rangle$ onto the new basis $|\alpha_L^{n+1}\rangle$ (We explain in the following subsection how to do the projection). Then consider

the *system* $[\mathbf{B_L^n}\bullet]$ as a new left block $[\mathbf{B_L^{n+1}}]$ in the basis $\{|\alpha_L^{n+1}\rangle\}$ with $M+n$ lattice sites.

5. Shift the right block (keeping its size) towards the right direction by one site, getting a new right block $[\mathbf{B_R^{n+1}}]$. Then form a new superblock $[\mathbf{B_L^{n+1}} \bullet \mathbf{B_R^{n+1}}]$ and replace the old one. Here the single site $[\bullet]$ is in the basis $\{|S^{n+1}\rangle\}$.

6. $n = n+1$, go back to step 2, and repeat the steps 2–6, until a desired size is reached.

If the infinite system algorithm runs until the size of the superblock is large enough, it could describe effectively the thermodynamic behavior of the system.

3.2.2 The finite system algorithm

In general the infinite-system algorithm cannot give accurate results, so that we have to further use the finite-system algorithm after the infinite algorithm to get more accurate results. The method is aiming to find an optimal description of the system of a fixed length. We repeat the algorithm at each site and several sweeps[4] until the energy is approaching convergence. The procedure of this method is as follows (also see Fig. 3.3):

1. Use the infinite system algorithm for the first steps to build the left block up to $N-M-1$ sites, where N is the length of the whole chain, and $n = N-M$. Note that at each iteration of the infinite system algorithm, one should store the left block Hamiltonian and the operators for use at the next sweep.

2. Diagonalize the superblock Hamiltonian with N sites, and obtain the ground state wavefunction $|\Psi\rangle$.

3. Permute the left block and the right block, then one considers the single site and the right block $[\bullet\mathbf{B_R^n}]$ as the *system*, and the left block as the *environment*. Now the new wavefunction is $|\Psi'\rangle$ in the basis $|\alpha_R^n S^n \alpha_L^n\rangle$.

4. Perform the SVD on the matrix Ψ', obtaining the projector U, which project the basis $|\alpha_R^n S^n\rangle$ onto $|\alpha_R^{n-1}\rangle$. Project the operators and the Hamiltonian (in $[\bullet\mathbf{B_R^n}]$) onto the new basis, and store them. Consider then $[\bullet\mathbf{B_R^n}]$ as a new right block $[\mathbf{B_R^{n-1}}]$.

[4] A complete back-and-forth sequence for both blocks in a chain is called a sweep.

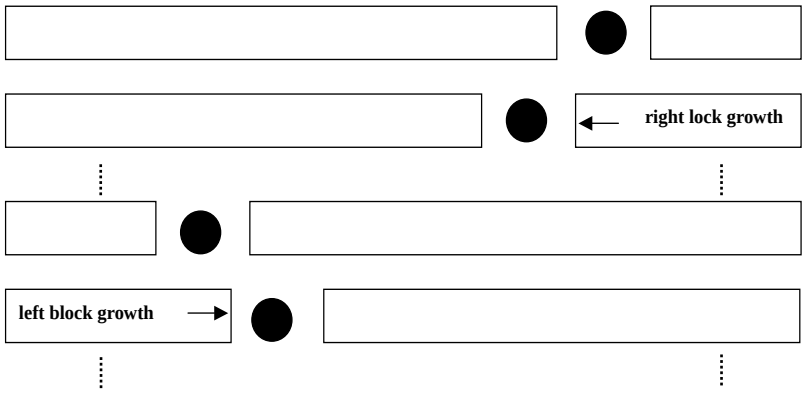

Figure 3.3: The pictorial description of the finite system algorithm. In the right-to-left sweep the right block grows at the expense of shrinking the left block. In the left-to-right sweep, on the contrary the left block grows at the expense of shrinking the right block.

5. Shrink the left block towards the left direction by one site, obtaining the left block $[B_L^{n-1}]$, which has already been stored in the previous infinite-algorithm steps or previous sweeps. Construct the new superblock $[\mathbf{B_L^{n-1}} \bullet \mathbf{B_R^{n-1}}]$. Here the single site $[\bullet]$ is in the basis $|S^{n-1}\rangle$.

6. $n = n - 1$, go back to the step 2, and repeat the steps 2–6 until $n = 1$.

   (The above is the right-to-left phase of the algorithm, and called a right-to-left *sweep*.)

7. Build up the superblock $[\mathbf{B_L^n} \bullet \mathbf{B_R^n}]$ $(n = 1)$.

8. Diagonalize the Hamiltonian of the superblock, obtaining the ground state $|\Psi\rangle$ in the basis $\{|\alpha_L^n S^n\rangle|\alpha_R^n\rangle\}$.

9. Perform the SVD on the matrix Ψ, obtaining the projector U. Project the operators and the Hamiltonian onto the new basis $\{\alpha_L^{n+1}\}$. Form the new left block B_L^{n+1}. Remember to update the stored operators and the Hamiltonian in the previous sweep.

10. Shrink the right block towards the right direction by one site, obtaining a new right block $[B_R^{n+1}]$. Construct the new superblock $[\mathbf{B_L^{n+1}} \bullet \mathbf{B_R^{n+1}}]$. Here the single site is in the basis $|S^{n+1}\rangle$.

11. $n = n + 1$, go back to step 8, and repeat step 8-11, until $n = N - 2M$.

    (This is the left to right phase of the algorithm.)

12. Go back to step 2. Carry out all of the following steps, until the energy approaches the convergence. In the end we can get a good precision.

The left block grows at the expense of shrinking the right block, and the right block grows at the expense of shrinking the right block. The single site is thus moved back and forth with the left block and right block. After several sweeps, one can get more accurate values than in the infinite system algorithm.

3.3 Operators and correlations

At the DMRG iterative steps one cannot use directly the operators and correlations in their original basis to build the Hamiltonian. One has to project the operators and correlations onto the new basis keeping the dimension of the Hilbert space constant. Then operator and correlations have to be initialized, updated and evaluated in the procedure of the DMRG.

In this section we talk about how to project the operators and correlations from the old basis onto the new basis, and how to evaluate them. The correlations we are interested in are such as the spin-spin $\langle \sigma_i^z \sigma_j^z \rangle$, creation-annihilation $\langle a_i^\dagger a_j \rangle$, and density-density correlations $\langle n_i n_j \rangle$, where i and j are the indices of lattice sites. Our discussion is in the left-to-right sweep, but it can easily be extended to the right-to-left sweep.

3.3.1 Projection onto the new basis

Consider a superblock $[\mathbf{B_L^n} \bullet \mathbf{B_R^n}]$ at the nth step, where the basis states are $|\alpha_L^n\rangle$, $|S^n\rangle$ and $|\alpha_R^n\rangle$, respectively. In the DMRG, the basis $\{|\alpha_L^n\rangle\}$ are not known explicitly, but the operators in this basis are known. Assume the operator O_i is acting the site i in the left block $[\mathbf{B_L^n}]$, i.e. $\langle \alpha_L^n | O_i | \tilde{\alpha}_L^n \rangle$, which can be written as

$$O_i = \sum_{\alpha_L^n, \tilde{\alpha}_L^n} O^i_{\alpha_L^n \tilde{\alpha}_L^n} |\alpha_L^n\rangle\langle\tilde{\alpha}_L^n|. \tag{3.11}$$

At the further step we can get the new basis $|\alpha_L^{n+1}\rangle$ through the SVD

$$|\alpha_L^{n+1}\rangle \equiv \sum_{\alpha_L^n S^n} U^{\alpha_L^{n+1}}_{\alpha_L^n S^n} |\alpha_L^n\rangle |S^n\rangle. \tag{3.12}$$

Update the operator O_i from the basis $|\alpha_L^n\rangle$ to $|\alpha_L^{n+1}\rangle$, substituting Eq. (3.12) into Eq. (3.11), and we have the operator in the new basis

$$\langle \alpha_L^{n+1} | O_i | \tilde{\alpha}_L^{n+1} \rangle = \sum_{\alpha_L^n, \tilde{\alpha}_L^n, S^n} \left(U^{\alpha_L^{n+1}}_{\alpha_L^n S^n} \right)^* O^i_{\alpha_L^n \tilde{\alpha}_L^n} U^{\tilde{\alpha}_L^{n+1}}_{\tilde{\alpha}_L^n S^n}. \tag{3.13}$$

If the operator is acting on the single site s outside of the left block, say O_s, its representation in the new basis is

$$\langle \alpha_L^{n+1}|O_s|\tilde{\alpha}_L^{n+1}\rangle = \sum_{\alpha_L^n,S^n,\tilde{S}^n} \left(U^{\alpha_L^{n+1}}_{\alpha_L^n S^n}\right)^* O^s_{S^n\tilde{S}^n} U^{\tilde{\alpha}_L^{n+1}}_{\alpha_L^n\tilde{S}^n}. \tag{3.14}$$

In the case of correlations, we consider one operator inside the left block O_i and the other acting the single site outside the left block O_s. In the new basis the correlation O_iO_s reads

$$\langle \alpha_L^{n+1}|O_iO_s|\tilde{\alpha}_L^{n+1}\rangle = \sum_{\alpha_L^n,\tilde{\alpha}_L^n,S^n,\tilde{S}^n} \left(U^{\alpha_L^{n+1}}_{\alpha_L^n S^n}\right)^* O^i_{\alpha_L^n\tilde{\alpha}_L^n} O^s_{S^n\tilde{S}^n} U^{\tilde{\alpha}_L^{n+1}}_{\tilde{\alpha}_L^n\tilde{S}^n}. \tag{3.15}$$

3.3.2 Evaluation of physical quantities

At the last step of the DMRG, the ground state of the system $|\Psi\rangle$ is obtained. Then various physical quantities can be evaluated under the form $\langle\Psi|O_i|\Psi\rangle$.

If i is in the left block, the local quantities $\langle\Psi|O_i|\Psi\rangle$ are given by

$$\langle\Psi|O_i|\Psi\rangle = \sum_{\alpha_L^n,S_n,\alpha_R^n,\tilde{\alpha}_L^n} \Psi^*_{\alpha_L^n,S_n,\alpha_R^n} O_{\alpha_L^n,\tilde{\alpha}_L^n} \Psi_{\tilde{\alpha}_L^n,S_n,\alpha_R^n}. \tag{3.16}$$

If i is in the right block $[\mathbf{B_R^n}]$, one has

$$\langle\Psi|O_i|\Psi\rangle = \sum_{\alpha_L^n,S_n,\alpha_R^n,\tilde{\alpha}_R^n} \Psi^*_{\alpha_L^n,S_n,\alpha_R^n} O_{\alpha_R^n,\tilde{\alpha}_R^n} \Psi_{\alpha_L^n,S_n,\tilde{\alpha}_R^n}. \tag{3.17}$$

For a correlation function such as $\langle\Psi|O_iO_j|\Psi\rangle$, the evaluation depends on the site location of i and j. If they are on different blocks, e.g. i in the left block and j in the right block, one follows the procedure for separate operators:

$$\langle\Psi|O_iO_j|\Psi\rangle = \sum_{\alpha_L^n,S^n,\alpha_R^n,\tilde{\alpha}_L^n,\tilde{\alpha}_R^n} \Psi^*_{\alpha_L^n S^n\alpha_R^n} O^i_{\alpha_L^n\tilde{\alpha}_L^n} O^j_{\alpha_R^n\tilde{\alpha}_R^n} \Psi_{\tilde{\alpha}_L^n S^n\tilde{\alpha}_R^n}. \tag{3.18}$$

The correlations $\langle\Psi|O_iO_j|\Psi\rangle$ cannot be calculated when i and j are on the same block at the last step. They have to be calculated at previous steps of the last sweep, where the left block and the single site form a product Hilbert space, and i is in the left block $[\mathbf{B_L}]$ and j is acting on the single site $[\bullet]$ attaching to the left block. The correlations can thus be written as

$$\langle\Psi|O_iO_j|\Psi\rangle = \sum_{\alpha_L^n,S^n,\alpha_R^n,\tilde{\alpha}_L^n,\tilde{S}^n} \Psi^*_{\alpha_L^n S^n\alpha_R^n} O^i_{\alpha_L^n\tilde{\alpha}_L^n} O^j_{S^n\tilde{S}^n} \Psi_{\tilde{\alpha_L^n}\tilde{S}^n\alpha_R^n}. \tag{3.19}$$

3.4 The efficiency of algorithms

The diagonalization of the superblock Hamiltonian is the major part of time consuming in the DMRG. Since we are only interested in the ground state of the system, we can resort to an iterative method–the Lanczos algorithm, to get the lowest energy eigenstate with high efficiency. However, in the thesis we do not consider the detail of how to realize the Lanczos algorithm. In Matlab, the function *eigs* is based on this algorithm to perform diagonalization of a large sparse matrix.

Within the iterative method, there are several schemes to accelerate the diagonalization, such as the block storage and the state prediction. In addition, good quantum numbers of the Hamiltonian can reduce storage and thin out the Hilbert space.

In this section we talk about the above optimizations. We have implemented them in our routines.

3.4.1 Block storage

The superblock Hamiltonian is constructed explicitly as a large, sparse matrix in a tensor product basis

$$H = H^L \otimes I^R + I^L \otimes H^R + L \otimes R, \tag{3.20}$$

where the operator H^L (H^R) is the Hamiltonian acting on the left (right) block, and $L \otimes R$ is the interaction term between the left and right blocks. For simplicity of the discussion, here we assume that the single site is tensored into the left block. i.e. $[\mathbf{B_L^n}] \equiv [\mathbf{B_L^n \bullet}]$. The dimension of the Hamiltonian H is $D * d * D$, and thus the storage requirement is very large.

However, within the Lanczos algorithm there is no need to construct explicitly a large sparse Hamiltonian matrix through the tensor products between the left and right blocks. The Lanczos algorithm only needs a *matrix-vector product*, i.e. $H|\Psi\rangle$, where $|\Psi\rangle$ is the wavefunction vector of the Hamiltonian matrix H. This efficient representation of the Hamiltonian matrix reduces storage and time consuming of diagonalization [96].

The wavefunction $|\Psi\rangle$ of the Hamiltonian H can be decomposed as

$$|\Psi\rangle = \sum_{\alpha_L, \alpha_R} \Psi_{\alpha_L \alpha_R} |\alpha_L\rangle |\alpha_R\rangle, \tag{3.21}$$

where we omit the DMRG step number n in $|\alpha_L^n\rangle$, since this technique is not relevant to the truncation process.

Then $H|\Psi\rangle$ which is called the matrix-vector product can then be written as

$$\begin{aligned} H|\Psi\rangle &= H\sum_{\alpha_L,\alpha_R}\Psi_{\alpha_L\alpha_R}|\alpha_L\rangle|\alpha_R\rangle \\ &= \sum_{\alpha_L,\alpha_R}\Psi_{\alpha_L\alpha_R}[\big(H^L|\alpha_L\rangle\big)\otimes|\alpha_R\rangle+|\alpha_L\rangle\otimes\big(H^R|\alpha_R\rangle\big) \\ &\quad +(L|\alpha_L\rangle)\otimes(R|\alpha_R\rangle)] \\ &= \sum_{\alpha'_L,\alpha_L,\alpha_R}H^L_{\alpha'_L\alpha_L}\Psi_{\alpha_L\alpha_R}|\alpha'_L\rangle|\alpha_R\rangle+\sum_{\alpha'_R,\alpha_L,\alpha_R}\Psi_{\alpha_L\alpha_R}H^R_{\alpha'_R\alpha_R}|\alpha_L\rangle|\alpha'_R\rangle \\ &\quad +\sum_{\alpha'_L,\alpha'_R,\alpha_L,\alpha_R}L_{\alpha'_L\alpha_L}\Psi_{\alpha_L\alpha_R}R_{\alpha'_R\alpha_R}|\alpha'_L\rangle|\alpha'_R\rangle, \end{aligned} \tag{3.22}$$

where

$$H^L = \sum_{\alpha'_L\alpha''_L}H^L_{\alpha'_L\alpha''_L}|\alpha'_L\rangle\langle\alpha''_L|, \tag{3.23}$$

$$H^R = \sum_{\alpha'_R\alpha''_R}H^R_{\alpha'_R\alpha''_R}|\alpha'_R\rangle\langle\alpha''_R|, \tag{3.24}$$

$$\tag{3.25}$$

and L (R) is similar with H^L (H^R). Think of Ψ as a matrix, and the matrix-vector product is represented as

$$H\Psi = H^L\Psi+\Psi(H^R)^\dagger+L\Psi R^\dagger. \tag{3.26}$$

$H|\Psi\rangle$ is the product that the Lanczos algorithm needs. Thus, the matrix-vector product in this form only require $\mathcal{O}(D^3d^2)$ operations, instead of the original multiplications $\mathcal{O}(D^4d^2)$. This block storage optimization improves approximately an order of magnitude than the original formulation. In my calculations, this optimization is always performed.

3.4.2 State prediction

The Lanczos algorithm convergence depends largely on the initial (random) guess vector for the desired eigenvector. If a suitable starting vector (guess vector) is specified, the number of Lanczos iterative steps are reduced substantially, and the convergence of eigenvalue will be accelerated largely.

Thus, a good initial guess vector can dramatically speed up the diagonalization of the DMRG [112]. In the DMRG one might construct a starting

vector from the previous eigenvector calculation typically. Although the previous wavefunction is in a different basis, corresponding to a different block configuration, it can be transformed into the current basis corresponding to the current configuration.

We describe here the procedure of finding such an initial vector as a good guess in the finite system algorithm.

Consider a step in the left-to-right sweep, e.g. the nth step, where the system block is $[\mathbf{B_L^n}\bullet]$ in the basis $|\alpha_L^n S^n\rangle$, the environment block is $[\mathbf{B_R^n}]$ in the basis $|\alpha_R^n\rangle$, and the wavefunction in the nth superblock basis is denoted as:

$$|\Psi^{[n]}\rangle = \sum_{\alpha_L^n S^n \alpha_R^n} \Psi^{[n]}_{\alpha_L^n S^n \alpha_R^n} |\alpha_L^n S^n \alpha_R^n\rangle. \tag{3.27}$$

The next step in the algorithm is to calculate the wavefunction $|\Psi^{[n+1]}\rangle$ in the $(n+1)$th superblock basis $|\alpha_L^{n+1} S^{n+1} \alpha_R^{n+1}\rangle$. The wavefunction $|\Psi^{[n]}\rangle$ is chosen as an initial guess vector for $|\Psi^{[n+1]}\rangle$, so $|\Psi^{[n]}\rangle$ has to be transformed onto the basis of $|\Psi^{[n+1]}\rangle$.

The basis $|\alpha_L^{n+1}\rangle$ can be approximated by means of the SVD at the nth step, i.e.

$$|\alpha_L^{n+1}\rangle = \sum_{\alpha_L^n, S^n} U^{\alpha_L^{n+1}}_{\alpha_L^n, S^n} |\alpha_L^n\rangle |S^n\rangle, \tag{3.28}$$

where the truncation operator $U^{\alpha_L^{n+1}}_{\alpha_L^n, S^n}$ represents the transformation from the tensor product basis to the truncated basis.

The basis $|S^{n+1}\alpha_R^{n+1}\rangle$ can be got from the earlier right-to-left sweep. At the firstly previous, right-to-left sweep, the basis $|\alpha_R^n\rangle$ of the right block $\mathbf{B_R^n}$ is written in a similar fashion as in Eq. (3.28):

$$|\alpha_R^n\rangle = \sum_{\alpha_R^{n+1}, S^{n+1}} U^{\alpha_R^n}_{\alpha_R^{n+1}, S^{n+1}} |S^{n+1}\rangle |\alpha_R^{n+1}\rangle. \tag{3.29}$$

Note that the truncation matrices U in the left-to-right sweep and in the right-to-left sweep are independent.

We know that the transformation from $|\alpha_L^n S^n\rangle$ to $|\alpha_L^{n+1}\rangle$ is not exact. However we can make an approximation here:

$$\sum_{\alpha_R^{n+1}} |\alpha_R^{n+1}\rangle\langle\alpha_R^{n+1}| \approx 1. \tag{3.30}$$

Based on this approximation we can get the guessed wavefunction $|\tilde{\Psi}^{[n+1]}\rangle$ from the $|\Psi^{[n]}\rangle$:

$$|\tilde{\Psi}^{[n+1]}\rangle \approx \sum_{\alpha_L^n S^n \alpha_R^n} U^{\alpha_L^{n+1}}_{\alpha_L^n S^n} \Psi^{[n]}_{\alpha_L^n S^n \alpha_R^n} U^{\alpha_R^n}_{\alpha_R^{n+1} S^{n+1}} |\alpha_L^{n+1} S^{n+1} \alpha_R^{n+1}\rangle. \tag{3.31}$$

In this form the wavefunction as a guess vector can accelerate the finding of the true wavefunction. This will lead to a dramatic reduction of iteration steps. The speed of algorithm will be increased by about an order of magnitude. However, all the truncation matrices U have to be stored on the disk.

In the infinite-system algorithm, there is also some optimal methods [113, 114] related to the wavefunction prediction, but we did not perform in our calculations. The interested reader could refer to the papers [113,114], or see the review by U. Schollwöck [96].

3.4.3 Conserved quantum numbers

In the DMRG method, making use of the symmetries and good quantum numbers of the Hamiltonian can greatly reduce the block storage and computation time [96, 115].

If a quantity is conserved with the Hamiltonian, then the Hilbert space $\mathcal{H}$ of the system is divided into a direct sum of subspaces with respect to the quantity. Thus, if one is interested in some specific properties related to this quantity, one needs only to diagonalize the Hamiltonian within the corresponding subspace. We call this quantity a good quantum number of the Hamiltonian. In the thesis, we consider the phonon-Hubbard model in 1D with conserved number of particles, so we can make use of the number operator of phonons as a good quantum number.

The Hamiltonian of the system is denoted as H in the Hilbert space $\mathcal{H}$, and the total number of phonons is N, which is conserved with the Hamiltonian, i.e. $[\hat{H}, \hat{N}] = 0$.

We are interested in the eigenstate $|\Psi_N\rangle$ with $\hat{N}|\Psi_N\rangle = N|\Psi_N\rangle$. Define P_N as the projector on the subspace $\mathcal{H}_N$ of fixed number of phonons N,

$$P_N|\Psi\rangle = |\Psi_N\rangle. \tag{3.32}$$

Then we can project the Hamiltonian onto the subspace $\mathcal{H}_N$.

P_N is evidently an observable possessing a total of two eigenvalues 0 and 1, and satisfies

$$P_N^2 = P_N, \quad P_N = P_N^\dagger. \tag{3.33}$$

The subspace $\mathcal{H}_N$ on which P_N projects is just the subspace of its eigenvalue 1.

Consider now a set of number operator states $|0\rangle, |1\rangle, |2\rangle, \ldots, |N\rangle$ of phonons in a single site. These states span a certain subspace $\mathcal{H}$ with N dimensions. The projector on this subspace $\mathcal{H}$ is

$$P \equiv \sum_{n=0}^{N} |n\rangle\langle n|. \tag{3.34}$$

Extending from a single site to L sites, the projector is changed to a tensor product,

$$P = \prod_{i=1}^{L} \left(\sum_{n_i=0}^{N} |n_i\rangle\langle n_i| \right), \tag{3.35}$$

which is just the identity in the truncated phonon Hilbert space. As the total number of particles is conserved, i.e. $\sum_{i=1}^{L} n_i = N$, this means that if $\sum_{i=1}^{L} n_i \neq N$, the corresponding eigenvalues of P_N must be 0. Under this restriction, the projector onto the subspace $\mathcal{H}_N$ of N number of phonons is thus

$$P_N = \prod_{i=1}^{L} \left(\sum_{n=0}^{N} |n\rangle\langle n|_i \right) \delta_{\sum_i^L n_i, N}. \tag{3.36}$$

We turn to the implementation in the DMRG. To simplify the discussion, the single site is tensored into the left block as in the above subsection, i.e. $[\mathbf{B_L}] \equiv [\mathbf{B_L}\bullet]$. The projector on the subspace $\mathcal{H}_N$ is written as

$$P_N = \sum_{N_L=0}^{N} P_{N_L}^{L} \otimes P_{N_R}^{R}, \tag{3.37}$$

where

$$P_{N_L}^{L} = \sum_{\alpha_L} \delta_{n(\alpha_L), N_L} |\alpha_L\rangle\langle\alpha_L|, \tag{3.38}$$

$$P_{N_R}^{R} = \sum_{\alpha_R} \delta_{n(\alpha_R), N-N_L} |\alpha_R\rangle\langle\alpha_R|. \tag{3.39}$$

Here, $N_L(N_R)$ is the number of particles in the left(right) block, $n(\alpha_{L(R)})$ is the number of particles in the state $|\alpha_{L(R)}\rangle$, and $P_{N_L}^{L}(P_{N_R}^{R})$ denotes the projectors on the subspace of $N_L(N_R)$ phonons in the left(right) block.

Considering the matrix-vector product of the Hamiltonian, we have

$$H_N|\Psi_N\rangle = P_N H P_N|\Psi\rangle = H P_N|\Psi\rangle = H|\Psi_N\rangle.$$

Think of Ψ_N as the matrix form of $|\Psi_N\rangle$, and we have

$$H_N\Psi_N = H^L\Psi_N + \Psi_N(H^R)^\dagger + L\Psi_N R^\dagger. \tag{3.40}$$

Consequently, as discussed in Subsection 3.4.1, the Hamiltonian in the Hilbert subspace $\mathcal{H}_N$ can also be calculated efficiently within the Lanczos algorithm.

3.5 Some remarks and conclusions

In our DMRG method, the truncated weight is zero, that is, all of density-matrix eigenstates corresponding to positive eigenvalues are kept as the truncated basis. Assume we increase the *system* up to the length N. If there is no truncation, the dimension of Hilbert space of the *system* is d^N, where d is the dimension of the Hilbert space at single site. However, if there is truncation, the dimension of Hilbert space of the *system* is only D, where D is the number of truncated states. Since $D \ll d^N$, the truncation is the major error in our method. Furthermore, from the SVD, we know that the number of truncated states depends on the size of the *environment*. Therefore, in order to get more accurate results, we have to keep more truncated states, i.e. to increase the sizes of the *system* and the *environment*. The number of truncated states we kept in the calculations is usually $m = 128$, which is large enough to get a good precision.

Our DMRG algorithm is implemented in Matlab. For the sparse matrix diagonalization, it is convenient to call the function *eigs*, which uses the Lanczos algorithm, and the matrix-vector product and the state prediction are available as well. To perform the singular value decomposition of the wavefunction we call the function *svd* in Matlab.

To conclude, we build up our numerical method-the DMRG in this chapter, and discuss how to implement and improve our algorithms. In the following chapters our DMRG will be applied to study strongly correlated behaviors in ion traps.

Chapter 4

Effective Spin Models with Trapped Ions

Trapped ions as a clean experimental system offers us accurate techniques for the manipulation and measurement of quantum states [47]. In the last years this experimental field has been mainly motivated by applications to quantum information processing [48], in which internal electronic states are used as qubits, and vibrational modes permit us to perform quantum gates between them [51, 56].

In fact, by using similar ideas of quantum computation Ref. [70] and [71] have shown recently that trapped ions can be used for the study of a rich variety of quantum interacting models. The experimental requirements for the study of quantum interacting systems with trapped ions are indeed much less stringent than those for quantum information tasks.

In this chapter we pursue the ideas proposed in Ref. [70] for the realization of a quantum simulator [3, 6, 7] of quantum magnetism with trapped ions. We focus on the possibility of studying antiferromagnetic Ising and XY spin chains [116, 117, 118] in linear ion traps, where quantum phase transitions [119] can be induced and explored. We show that experiments with trapped ions can access the physics of magnetic quantum phases with an accuracy that is not possible in other experimental set-ups, and allow us to test general properties of quantum systems at, or near, criticality. On the other hand, the effective spin Hamiltonians that can be engineered with trapped ions show a few remarkable features, the most important one being the fact that spin–spin interactions follow power–law decays, something that induces long–range quantum correlations between distant ions, which are absent in the usual nearest–neighbor models.

The chapter is organized as follows. In the first section we give a description of quantum Ising model and XY model with nearest-neighbor in-

teractions as an introduction. In the second section we describe in detail our proposal, taking as a starting point the system formed by a set of trapped ions coupled to an off–resonant standing wave, and show that it realizes a system of effective interacting spins. We focus on the cases of Ising and XY interactions. In the third section we study the many–body problem posed by the quantum Ising model in ion traps. For this purpose, we make use of the quasi–exact numerical method-the DMRG, and introduce also an analytical, approximate solution in terms of Holstein–Primakoff bosons. The fourth section deals with the study of the XY model in ion traps. Finally, we present our conclusions.

4.1 Quantum spin models

Quantum spin–1/2 models are the simplest quantum magnetic systems showing a large variety of properties. One of the most important properties is the existence of quantum phase transition at zero temperature driven by quantum fluctuations. For instance, there is a quantum phase transition from the ferromagnetic phase to the paramagnetic phase in the quantum Ising model. Singularities occurs strictly at the transition point. On the experimental side, people are able to produce artificial samples with behaviors that fits well with the theoretical descriptions, such as one observed a quantum phase transition in the insulator $LiHoF_4$ [118, 119].

To solve these low-dimensional systems there are some efficient analytical and numerical tools, such as the Bethe Ansatz [1], bosonization [1], fermionization [1, 116, 117], exact diagonalization and the DMRG approach. In our discussion here we focus on free-fermionic quantum spin chains, which are nearest-neighbor spin models that can be mapped on systems of non-interacting fermions, and can be solved exactly, such as quantum Ising model and XY model [116, 117, 118, 119].

4.1.1 Quantum Ising model

The quantum Ising model in a transverse with lattice Hamiltonian is

$$H^{\text{Ising}} = J \sum_i \sigma_i^z \sigma_{i+1}^z + B \sum_i \sigma_i^x, \tag{4.1}$$

where σ_i^x and σ_i^z are Pauli matrices defined on the site i of 1D lattice, and we consider the nearest-neighbor interactions. The first term describes the ferromagnetic (antiferromagnetic) exchange interaction between spins depending

on $J < 0$ ($J > 0$), while the second term is the transverse magnetic field. Here the chain is assumed to be infinite.

The three components of the spins σ_i^x, σ_i^y, σ_i^z obey the commutation relations

$$[\sigma_i^\alpha, \sigma_i^\beta] = \sqrt{-1}\epsilon_{\alpha\beta\gamma}\sigma_i^\gamma, \tag{4.2}$$

where $\epsilon_{\alpha\beta\gamma}$ is the totally antisymmetric tensor, i.e. equal to zero if two indices are equal and $\epsilon_{\alpha\beta\gamma} = 1$. The basis states of spin-1/2 are denoted $|\uparrow\rangle = \binom{1}{0}$ and $|\downarrow\rangle = \binom{0}{1}$. Note that $\sigma_i^x = \sigma_i^+ + \sigma_i^-$, where σ_i^+ and σ_i^- are called raising and lowering operators, $\sigma^+|\downarrow\rangle = |\uparrow\rangle$ and $\sigma^-|\uparrow\rangle = |\downarrow\rangle$. σ_i^+ and σ_i^- allow to flip spins at site i.

In the absence of the transverse field, $B = 0$, it is most convenient to work in a basis diagonal in $\sigma^z = \pm 1$. The model then reduces to the well-known classical Ising model. For $J < 0$ the ground state is the ferromagnectically ordered state with $\sigma^z = 1$ or $\sigma^z = -1$ on every site, i.e. $|\uparrow\uparrow\uparrow\uparrow\cdots\rangle$ or $|\downarrow\downarrow\downarrow\downarrow\cdots\rangle$. For $J > 0$, the antiferromagnetically ordered state with $\sigma^z = 1$ ($\sigma^z = -1$) on odd sites and $\sigma^z = -1$ ($\sigma^z = 1$) on even sites, i.e. $|\uparrow\downarrow\uparrow\downarrow\cdots\rangle$ or $|\downarrow\uparrow\downarrow\uparrow\cdots\rangle$.

A small transverse field will cause the spins to flip and the ground state will be more complicated. If $|B| \ll |J|$, the ferromagnetic (antiferromagnetic) order will survive, i.e. $\langle\sigma_i^z\rangle \neq 0$. However, if $|B| \gg |J|$, all the spins will point in the x–direction, $\sigma^x = \pm 1$, which corresponds to a quantum paramagnetic ground state $|\rightarrow\rightarrow\rightarrow\rightarrow\cdots\rangle$ for $B > 0$ or $|\leftarrow\leftarrow\leftarrow\leftarrow\cdots\rangle$ for $B < 0$. Here $|\rightarrow\rangle = (|\uparrow\rangle + |\downarrow\rangle)/\sqrt{2}$ and $|\leftarrow\rangle = (|\uparrow\rangle - |\downarrow\rangle)/\sqrt{2}$ are the two eigenstates of σ_i^x with eigenvalues ± 1. The magnetization in the paramagnetic phase is zero $\langle\sigma_i^z\rangle = 0$.

Based on the above reason, there must be a quantum phase transition between ferromagnetic (antiferromagnetic) and paramagnetic ground state when $|J|$ is of the order of $|B|$. In fact, the critical point is at $J = B$. The equal-time correlation function in the ground state at each of the two limiting phases behaves like an exponential decay:

$$\langle\sigma_i^z\sigma_j^z\rangle \sim \mathrm{e}^{-|x_i - x_j|/\xi} \tag{4.3}$$

for large $x_i - x_j$, where x_i is the spatial coordinate of site i, and ξ is the correlation length. ξ could be the length scale determining the exponential decay of equal-time correlations in the ground state. However, at the critical point $|\frac{J}{B}|_c$, the correlation function is a power-law decay:

$$\langle\sigma_i^z\sigma_j^z\rangle \sim \Lambda|x_i - x_j|^{-\nu}, \tag{4.4}$$

where ν is the universal critical exponent, and Λ is nonuniversal constant of proportionality.

To quantitatively study quantum Ising model, one can use the Jordan-Wigner transformation [116, 117, 118, 119]. This is a powerful mapping between models with spin–1/2 degree of freedom and spinless fermions. Under this transformation the nearest-neighbor quantum Ising model with a transverse magnetic field can be transformed into a system of non-interacting fermions, then its exact solution can be obtained.

Assume $c_i^\dagger$ and c_i are the annihilation and creation operators of spinless fermions, which satisfy fermionic anticommutation relations:

$$[c_i, c_j^\dagger]_+ = \delta_{ij}, \quad [c_i, c_j]_+ = 0, \quad [c_i^\dagger, c_j^\dagger]_+ = 0, \tag{4.5}$$

and

$$c_i{}^2 = (c_i^\dagger)^2 = 0. \tag{4.6}$$

While the raising and lowering operators σ_i^+ and σ_i^- satisfy partly the relations of fermions:

$$[\sigma_i^-, \sigma_i^+]_+ = 1, \quad \sigma_i^{-2} = (\sigma_i^+)^2 = 0, \tag{4.7}$$

and partly the relations of bosons:

$$[\sigma_i^+, \sigma_j^-] = [\sigma_i^+, \sigma_j^+] = [\sigma_i^-, \sigma_j^-] = 0, \quad i \neq j. \tag{4.8}$$

The Jordan-Wigner transformation is

$$c_i = \exp\left[\pi i \sum_j^{i-1} \sigma_j^+ \sigma_j^-\right] \sigma_i^-, \tag{4.9}$$

$$c_i^\dagger = \sigma_i^+ \exp\left[-\pi i \sum_j^{i-1} \sigma_j^+ \sigma_j^-\right]. \tag{4.10}$$

Then

$$c_i^\dagger c_i = \sigma_i^+ \sigma_i^-, \tag{4.11}$$

and the inverse transformation is

$$\sigma_i^- = \exp\left[\pi i \sum_j^{i-1} \sigma_j^+ \sigma_j^-\right] c_i, \tag{4.12}$$

$$\sigma_i^+ = c_i^\dagger \exp\left[-\pi i \sum_j^{i-1} \sigma_j^+ \sigma_j^-\right]. \tag{4.13}$$

The coupling terms like $\sigma_i^+\sigma_{i+1}^-$ can also be written in terms of fermions. One can immediately get

$$\sigma_i^+\sigma_{i+1}^- = c_i^\dagger c_{i+1}, \quad \sigma_i^+\sigma_{i+1}^+ = c_i^\dagger c_{i+1}^\dagger, \tag{4.14}$$

$$\sigma_i^-\sigma_{i+1}^+ = -c_i c_{i+1}^\dagger, \quad \sigma_i^-\sigma_{i+1}^- = -c_i c_{i+1}. \tag{4.15}$$

To analyze the Ising model it is convenient to rotate spin axes by 90 degrees about y–axis, i.e. $\sigma^z \to \sigma^x$ and $\sigma^x \to -\sigma^z$. Then the Ising model is written as

$$H^{\text{Ising}} = J\sum_{\langle ij\rangle}\sigma_i^x\sigma_j^x - B\sum_i \sigma_i^z. \tag{4.16}$$

In the fermion operators Eq. (4.16) is transformed to

$$H^{\text{Ising}} = J\sum_i (c_i^\dagger c_{i+1} + c_{i+1}^\dagger c_i + c_i^\dagger c_{i+1}^\dagger + c_{i+1}c_i - \frac{2B}{J}c_i^\dagger c_i + \frac{B}{J}). \tag{4.17}$$

The above Hamiltonian is quadratic, so that it is obviously diagonalisable. Introducing the Fourier transform

$$c_q = \frac{1}{\sqrt{N}}\sum_{j=1}^N c_j \mathrm{e}^{iqr_j}, \tag{4.18}$$

$$c_q^\dagger = \frac{1}{\sqrt{N}}\sum_{j=1}^N c_j^\dagger \mathrm{e}^{-iqr_j}, \tag{4.19}$$

where N is the number of sites under periodic boundary conditions, and $q = \frac{2\pi m}{N}$ is the complete set of wave vector with

$$m = -\frac{N-1}{2}, \cdots, 0, \cdots, \frac{N-1}{2} \qquad (\text{odd } N), \tag{4.20}$$

$$m = -\frac{N}{2}, \cdots, 0, \cdots, \frac{N}{2}-1 \qquad (\text{even } N). \tag{4.21}$$

The Hamiltonian then becomes

$$H^{\text{Ising}} = J\sum_q \left\{2[\frac{B}{J} - \cos(q)]c_q^\dagger c_q - i\sin(q)[c_q^\dagger c_{-q}^\dagger + c_q c_{-q}] - \frac{B}{J}\right\}. \tag{4.22}$$

We wish to write the Hamiltonian in the form of

$$H^{\text{Ising}} = \sum_q \epsilon_q \eta_q^\dagger \eta_q + \text{const}, \tag{4.23}$$

so we employ a Bogoliubov transformation from the operators c_q, $c_q^\dagger$ to the operators η_q, $\eta_q^\dagger$:

$$\eta_q = u_q c_q + i v_q c_{-q}^\dagger, \quad \eta_q^\dagger = u_q c_q^\dagger - i v_q c_q, \tag{4.24}$$

where η_q, $\eta_q^\dagger$ are fermions, and $u_q^2 + v_q^2 = 1$, $u_{-q} = u_q$, and $v_{-q} = -v_q$. The inverse transformation is written as

$$c_q = u_q \eta_q + i v_q \eta_{-q}^\dagger. \tag{4.25}$$

To make the Hamiltonian in the diagonal form, we demand that the off-diagonal terms must vanish when we substitute Eq. (4.25) into Eq. (4.22). Define $u_q = \cos\theta_q$, $v_q = \sin\theta_q$, then

$$\tan 2\theta_q = \frac{\sin q}{\cos(q) - \frac{B}{J}}. \tag{4.26}$$

The final Hamiltonian is

$$H^{\text{Ising}} = \sum_q \epsilon_q \eta_q^\dagger \eta_q + \text{const}, \tag{4.27}$$

where

$$\epsilon_q = 2J\left[1 + 2B/J\cos(q) + (B/J)^2\right]^{1/2} \tag{4.28}$$

is the single particle energy. As $\epsilon_q \geq 0$, the ground state $|0\rangle$ has no η fermions and therefore satisfies $\eta_q|0\rangle = 0$ for all q. The excited states are created by occupying the single-particle states. For instance, the n–particle state has the form $\eta_{q1}^\dagger \eta_{q2}^\dagger \cdots \eta_{qn}^\dagger |0\rangle$. Other quantities, such as total energy, magnetizations and correlations can be obtained from the ground state. The details could be found in Refs. [117, 118, 119].

4.1.2 Quantum XY model

The generic quantum XY model in a transverse magnetic field is written as

$$H^{\text{XY}} = J\sum_i \left[\frac{1+\gamma}{2}\sigma_i^x \sigma_{i+1}^x + \frac{1-\gamma}{2}\sigma_i^y \sigma_{i+1}^y\right] + B\sum_i \sigma_i^z, \tag{4.29}$$

where γ is the anisotropy parameter with limiting values: $\gamma = 1$ corresponding to the transverse quantum Ising model, and $\gamma = 0$ describing the transverse XX model. For simplicity we will here consider only the transverse XX model, i.e.

$$H^{\text{XX}} = \frac{J}{2}\sum_i (\sigma_i^x \sigma_{i+1}^x + \sigma_i^y \sigma_{i+1}^y) + B\sum_i \sigma_i^z. \tag{4.30}$$

The XY Hamiltonian can also be mapped exactly into a free fermion model through the Jordan-Wigner transformation, consisting of an assembly of non-interacting fermions:

$$H^{\mathrm{XX}} = J\sum_i (c_i^\dagger c_{i+1} + c_{i+1}^\dagger c_i) + 2B\sum_i c_i^\dagger c_i - NB. \tag{4.31}$$

If we consider a finite chain with open boundary conditions, we can introduce the fermion operators in the momentum space as [120]

$$c_q^\dagger = \left(\frac{2}{N+1}\right)^{1/2} \sum_{j=1}^{N} \sin(\frac{\pi j}{N+1} q) c_j^\dagger, \tag{4.32}$$

where

$$c_{N+1}^\dagger|0\rangle = 0, \quad c_0^\dagger|0\rangle = 0, \tag{4.33}$$

and $1 \leq q \leq N$. Substituting Eq. (4.32) into Eq. (4.31), we can get the simple diagonal form

$$H^{\mathrm{XX}} = \sum_q \epsilon_q c_q^\dagger c_q + \mathrm{const}, \tag{4.34}$$

with

$$\epsilon_q = 2J\cos(\frac{\pi}{N+1} q) + 2B. \tag{4.35}$$

Assume $J > 0$. For $B > J$, the energy of all the fermions are positive and the ground state has no fermions present. For $|B| < J$, the occupation of fermions in the ground state is partial. For $B < -J$, all the fermions have negative energy and every fermion state is occupied. At $B = -J$ or $B = J$, there is a transition from a simple vacuum state with no fermions to a low density superfluid, or from a low density superfluid to the state with all occupied fermions. At the critical points, the correlations behave in a power-law decay, with the critical exponent 1/2.

Starting from the ground state, the total energy, magnetizations and correlations can be obtained exactly [116, 121, 122, 123, 124, 125].

However, note that our spin models with long-range interaction to be discussed in the following is not exactly solvable. But they can be handled by making use of the DMRG method, and their behaviors are similar to the nearest-neighbor Ising or XY model.

4.2 Effective spin systems in ion traps

In this section we review the theoretical description of a set of trapped ions under the action of off–resonant standing waves presented in [70], and show that their quantum dynamics follows approximately that of quantum interacting spins. We also discuss carefully the effects of residual spin–phonon couplings.

Our proposal works with a set of N ions in a linear Paul trap, or in microtraps in one or two dimensions. In order to simplify the discussion, we focus here on the 1D case: a string of trapped ions. We assume that the ions have two internal hyperfine ground states, which are denoted the qubit (spin–1/2) states $|g\rangle$ and $|e\rangle$. All the ions are driven by the off-resonant lasers propagating along the axial (z) and radial (x and y) directions of the trap. The possible laser configuration is plotted in Fig. 4.1, which figure is taken from Ref. [70]. In Fig. 4.1, the authors use $|\uparrow\rangle$ and $|\downarrow\rangle$ instead of $|e\rangle$ and $|g\rangle$ in my thesis to represent the spin states, and use $|e\rangle$ to represent the auxiliary state $|p\rangle$ in my thesis. Only here use we their notations to explain this figure. We assume that the counterpropagating lasers along the α–direction ($\alpha = x, y, z$) push the ions in case that they are in the state $|\uparrow\rangle_\alpha$, where $|\uparrow\rangle_\alpha$ means the up state in the σ^α basis. This can be achieved by choosing the relative phases of the copropagating lasers so that the state $|\downarrow\rangle_\alpha$ is dark with respective to the lasers along the α–direction.

We explain in more detail here. Assume that in the far-detuning standing waves $\Omega_{\alpha\uparrow} = |\Omega_\alpha|$ and $\Omega_{\alpha\downarrow} = |\Omega_\alpha|\mathrm{e}^{i\phi}$, where ϕ is the relative phase. The interaction Hamiltonian could be written as

$$\begin{aligned} H_I &= \Omega_{\alpha\uparrow}|e\rangle\langle\uparrow|_z + \Omega_{\alpha\downarrow}|e\rangle\langle\downarrow|_z + h.c. \\ &= |\Omega_\alpha|(|e\rangle\langle\uparrow|_z + \mathrm{e}^{i\phi}|e\rangle\langle\downarrow|_z) + h.c., \end{aligned} \tag{4.36}$$

where $\langle\uparrow|_z$ and $\langle\downarrow|_z$ are the eigenstates of the Paul matrix σ^z.

If $\phi = 0, \pi$, we have

$$\begin{aligned} H_I &= |\Omega_\alpha||e\rangle(\langle\uparrow|_z \pm \langle\downarrow|_z) + h.c. \\ &= \begin{cases} \sqrt{2}|\Omega_\alpha||e\rangle\langle\uparrow|_x + h.c. & (\phi = 0) \\ \sqrt{2}|\Omega_\alpha||e\rangle\langle\downarrow|_x + h.c. & (\phi = \pi) \end{cases}, \end{aligned} \tag{4.37}$$

where $\langle\uparrow|_x$ and $\langle\downarrow|_x$ are the eigenstates of the Pauli matrix σ^x. This means that $\langle\downarrow|_x$ ($\langle\uparrow|_x$) is the dark state when $\phi = 0$ ($\phi = \pi$). Similarly, the eigenstates $\langle\uparrow|_y$ and $\langle\downarrow|_y$ of σ^y can also be introduced under the specific relative phases, such as $\phi = \pi/2, 3\pi/2$. Obviously, if $\Omega_{\alpha\uparrow} = |\Omega_\alpha|$ and $\Omega_{\alpha\downarrow} = 0$, we just have the dark state $\langle\downarrow|_z$ for σ^z.

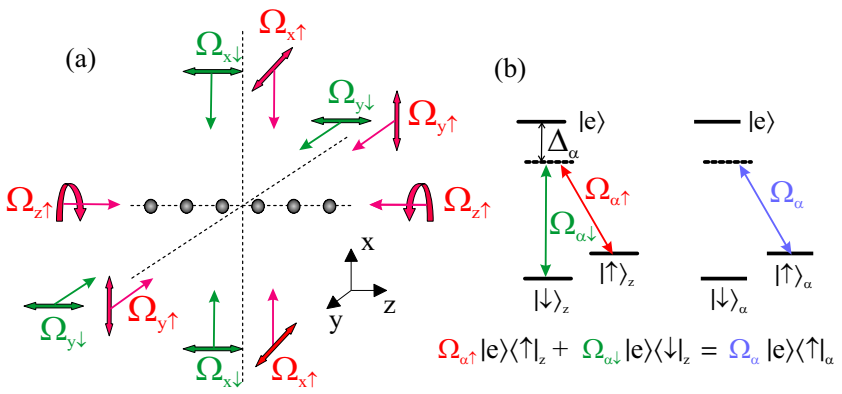

Figure 4.1: (a) The laser scheme in which the ions experience a force along α–direction ($\alpha = x, y, z$), if the ions are in the state $|\uparrow\rangle_\alpha$. Note that in Ref. [70] the authors use $|\downarrow\rangle$ and $|\uparrow\rangle$ to represent the spin–1/2 states. (b) Each pair of copropagating lasers in the α–direction drives a Raman transition between $|\uparrow\rangle_\alpha$ and $|\downarrow\rangle_\alpha$. By tuning the relative phases of the pair of copropagating lasers, the state $|\downarrow\rangle_\alpha$ could be coupled or uncoupled (i.e. dark state) to $|\uparrow\rangle_\alpha$. Counterpropagating lasers form a standing wave, which produce a position dependent ac-Stark shift on the ions if they are in the state $|\uparrow\rangle_\alpha$. Along the z–direction only one pair of counterpropagating lasers is needed. $\Omega_{\alpha\downarrow}$ and $\Omega_{\alpha\uparrow}$ are the Rabi frequencies of the lasers. Taken from [70] with kind permission by D. Porras and J. I. Cirac.

Our proposal relies on an always-on coupling between internal states (effective spins) and vibrational modes, in such a way that phonons transmit an interaction between different ions. Thus, the corresponding Hamiltonian has three contributions:

$$H = H_m + H_v + H_f. \tag{4.38}$$

H_m describes the local dynamics of internal states, which are a set of independent effective spins under the action of effective global magnetic fields in each direction:

$$H_m = \sum_{\substack{j=1,\ldots,N \\ \alpha=x,y,z}} B^\alpha \sigma_j^\alpha. \tag{4.39}$$

Note that B^z is the energy of the internal state, and B^x, B^y can be implemented by the action of lasers resonant with the internal transition. In Eq. (4.38), H_v is the vibrational Hamiltonian, and H_f is the internal state–phonon coupling. Both terms are described in the following two subsections.

4.2.1 Vibrational modes of ion chains

We consider 1D systems of trapped ions, whose physical implementation corresponds to Coulomb chains in linear Paul traps or linear arrays of ion microtraps. Here some main results are again listed for convenience. The details can be found in Chapter 2.

Let us assign **z** to the axis of the ion chain, and **x**, **y** to the radial directions. The potential experienced by the ions is determined by the trapping frequencies, ω_α (in the following the index α always runs over the spatial directions, $\alpha = x, y, z$), and the Coulomb repulsion:

$$\begin{aligned} V &= \frac{1}{2}m\sum_j \left(\omega_x^2 x_j^2 + \omega_y^2 y_j^2 + \omega_z^2 z_j^2\right) + \\ &\sum_{j>i} \frac{e^2}{\sqrt{(x_i - x_j)^2 + (y_i - y_j)^2 + (z_i - z_j)^2}}. \end{aligned} \tag{4.40}$$

In the harmonic approximation we express V as a function of the displacements around the equilibrium positions ($q_j^\alpha = x_j^\alpha - x_j^{\alpha,0}$), up to quadratic terms:

$$V = \frac{1}{2}m\sum_{\alpha,i,j} \mathcal{K}_{i,j}^\alpha q_i^\alpha q_j^\alpha, \tag{4.41}$$

where

$$\mathcal{K}_{i,j}^\alpha = \begin{cases} \omega_\alpha^2 - c_\alpha \sum_{j'(\neq i)} \frac{e^2/m}{|z_i^0 - z_{j'}^0|^3} & i = j \\ +c_\alpha \frac{e^2/m}{|z_i^0 - z_j^0|^3} & i \neq j \end{cases}. \tag{4.42}$$

The corresponding Hamiltonian can be diagonalized in terms of collective modes (phonons):

$$H_v = \frac{1}{2}m\sum_{i,j,\alpha} \mathcal{K}_{i,j}^\alpha q_i^\alpha q_j^\alpha + \sum_{i,\alpha} \frac{p_i^\alpha}{2m} = \sum_n \hbar\omega_{\alpha,n} a_{\alpha,n}^\dagger a_{\alpha,n}, \tag{4.43}$$

where p_i^α are the momenta corresponding to q_i^α, and $\omega_{\alpha,n}$ are the eigen frequencies. Local coordinates can be expressed in terms of creation and annihilation of collective vibrational modes:

$$q_i^\alpha = \sum_n \frac{\mathcal{M}_{i,n}^\alpha}{\sqrt{2m\omega_{\alpha,n}/\hbar}} \left(a_{\alpha,n}^\dagger + a_{\alpha,n}\right), \tag{4.44}$$

where $c_{x,y} = 1$, $c_z = -2$. Matrices $\mathcal{M}^\alpha$ in (4.48) diagonalize the vibrational hamiltonian: $\sum_{i,j} \mathcal{M}^\alpha_{i,n} \mathcal{K}^\alpha_{i,j} \mathcal{M}^\alpha_{j,m} = \omega^2_{\alpha,n} \delta_{n,m}$.

The characteristics of the vibrational modes are governed by the parameters β_α, which quantify the relative value of Coulomb interaction and trapping potentials:

$$\beta_\alpha = |c_\alpha| e^2 / m\omega_\alpha^2 d_0^3, \tag{4.45}$$

where d_0 is the mean distance between ions. If $\beta_\alpha \ll 1$, then phonons are close to be localized at each ion (stiff limit); on the contrary $\beta_\alpha \gg 1$ (soft limit) implies that Coulomb repulsion prevails over the trapping potential and, thus, phonons have a strong collective character that results in the ability to mediate interactions with a range of the order of the ion trap [70].

We summarize below the description of vibrational modes in different trapping conditions:

(i) *Coulomb chains (Paul traps).* In this experimental set–up the equilibrium positions in the axial ($\mathbf{z}$) direction are determined by the Coulomb interaction and the axial trapping, and β_z depends only on the number of ions N. This dependence can be estimated in the limit of many ions (see [126]):

$$\beta_z \approx \frac{1}{12} \frac{N^2}{\log(6N)}, \qquad N \gg 1. \tag{4.46}$$

$\beta_z \gg 1$ and thus axial modes in Coulomb crystals are always in the soft limit. On the other hand, $\beta_{x,y}$, can be reduced at will because one can increase the axial trapping frequencies $\omega_{x,y}$ while leaving constant the mean distance between ions, d_0. Indeed, condition $\beta_{x,y} < 1$ has to be fulfilled to make the Coulomb chain stable against zig-zag instabilities [126].

(ii) *Linear arrays of ion traps.* It is worth considering this case here due to the experimental effort currently being devoted to the fabrication of linear arrays of ion traps where equilibrium positions of the ions are chosen by individual confinement potentials for each ion [57]. In this case, all trapping frequencies ω_α can be chosen at will, and in particular condition $\beta_z \ll 1$ can be also fulfilled opposite to the case of standard Paul traps.

4.2.2 Internal state conditional forces

Internal states are coupled to the motion by placing the ions in an off–resonant standing–wave, such that they experience a state–dependent a.c.–Stark shift, see Chapter 2. Several configurations are possible, in which

internal states are coupled to vibrational modes that are transverse or longitudinal with respect to the trap axis. The characteristics of the resulting effective spin–spin interaction depends on the choice of the directions of the laser beams: in particular, axial vibrational modes mediate long–range interactions, with a range of the order of the ion chain, and radial modes mediate shorter range spin–spin interactions, with a power–law decay $J_{i,j} \propto 1/|i-j|^3$. Due to the fact that short–range spin Hamiltonians contain a rich quantum critical phenomenology, we focus in this work on this last situation.

Let us consider the following coupling between effective spins and radial motion:

$$H_f = -F_x \sum_j x_j |1\rangle\langle 1|_{z,j} - F_y \sum_j y_j |1\rangle\langle 1|_{y,j}. \tag{4.47}$$

$|1\rangle_\alpha$ is the eigenstate of σ^α with eigenvalue 1. The reason for this choice of couplings is that conditional forces are most easily implemented with the z component of the internal states (one only needs a single standing–wave). Thus, it is advantageous to couple σ^z to one of the radial directions. The first term in H_f is the one which corresponds to the pushing gate presented in [56], while the second one can be implemented by using two additional standing–waves [70].

The coupling of the internal states to the motion can be written as an effective spin–phonon coupling by expressing the ions' coordinates in terms of collective modes:

$$H_f = -\sum_{\alpha,i,n} F_\alpha \frac{\mathcal{M}^\alpha_{i,n}}{\sqrt{2m\omega_{\alpha,n}/\hbar}} \left(a^\dagger_{\alpha,n} + a_{\alpha,n}\right)\left(1+\tilde{\sigma}^\alpha_i\right). \tag{4.48}$$

In Eq. (4.48) we have introduced the notation $\tilde{\sigma^x} = \sigma^z$, $\tilde{\sigma^y} = \sigma^y$, that is, $\tilde{\sigma^\alpha}$ is the component coupled to the motion in the direction α.

4.2.3 Effective spin–spin interactions

Under certain conditions, a set of spins coupled to a common bath of vibrational modes is well described by an effective spin interacting Hamiltonian, something that is apparent if one makes use of the following canonical transformation [70, 127, 128]:

$$U = e^{-\mathcal{S}}, \qquad \mathcal{S} = \sum_{\alpha,i,n} \eta^\alpha_{i,n} \left(1+\tilde{\sigma}^\alpha_i\right)\left(a^\dagger_{\alpha,n} - a_{\alpha,n}\right),$$

$$\eta^\alpha_{i,n} = F_\alpha \frac{\mathcal{M}^\alpha_{i,n}}{\hbar\omega_{\alpha,n}} \sqrt{\frac{\hbar}{2m\omega_{\alpha,n}}}, \tag{4.49}$$

where $\eta^{\alpha}_{i,n}$ are the displacements of the modes in units of the ground state size.

In the new basis the Hamiltonian (4.38) includes an effective spin-spin interaction:

$$e^{-\mathcal{S}} H e^{\mathcal{S}} = H_v + \frac{1}{2}\sum_{\alpha,i,j} J^{[\alpha]}_{i,j}\tilde{\sigma}^{\alpha}_i\tilde{\sigma}^{\alpha}_j + \sum_{\alpha,i} B'^{\alpha}\sigma^{\alpha}_i + H_E, \tag{4.50}$$

where

$$-J^{[\alpha]}_{i,j} = \sum_n \frac{F^2_{\alpha}}{m\omega^2_{\alpha,n}}\mathcal{M}^{\alpha}_{i,n}\mathcal{M}^{\alpha}_{j,n} = 2\sum_n \eta^{\alpha}_{i,n}\eta^{\alpha}_{j,n}\hbar\omega_{\alpha,n}. \tag{4.51}$$

H_E is a residual spin–phonon coupling, whose explicit form is given below. From (4.51) and the definition of $\mathcal{M}^{\alpha}$ one can easily deduce that in the limit $\beta_{\alpha} \ll 1$:

$$J^{[\alpha]}_{i,j} \approx \frac{J^{[\alpha]}}{|z'^0_i - z'^0_j|^3}, \quad J^{[\alpha]} = 2\beta_{\alpha}\eta^2_{\alpha}\hbar\omega_{\alpha}, \tag{4.52}$$

where z'^0_i are the ions' positions in units of the average distance, d_0. We have introduced η, which characterizes the displacement of the phonons due to the presence of the state–dependent force:

$$\eta_{\alpha} = F_{\alpha}\sqrt{\hbar/2m\omega_{\alpha}}/\hbar\omega_{\alpha}. \tag{4.53}$$

Note that in (4.52) the effective magnetic fields receive, after the canonical transformation, a contribution from the pushing forces $B'^{\alpha} = B^{\alpha} + F^2_{\alpha}/(m\omega^2_{\alpha})$. The extra term in B'^{α} does not depend on the ion's site, and thus can be considered as an overall correction to the global effective magnetic fields.

Radial modes in a chain of trapped ions allow us to implement two types of spin models. If H_f acts only on one of the directions of motion, say $\mathbf{x}$, we get an Ising spin–spin interaction:

$$H^{\text{Ising}}_S = \frac{1}{2}\sum_{i,j} J^{[x]}_{i,j}\sigma^z_i\sigma^z_j + \sum_i B^x\sigma^x_i. \tag{4.54}$$

The residual spin–phonon couplings are given, to lowest order in η by:

$$H^{\text{Ising}}_E \;=\; B_x\sum_{i,n} -i\sigma^y_i\eta^x_{i,n}(a^{\dagger}_{x,n} - a_{x,n}). \tag{4.55}$$

On the other hand, if we apply two conditional forces in both radial directions, we get a Hamiltonian which couples two components of the effective spins.

$$H^{\text{XY}}_S = \frac{1}{2}\sum_{i,j}(J^{[x]}_{i,j}\sigma^z_i\sigma^z_j + J^{[y]}_{i,j}\sigma^y_i\sigma^y_j) + \sum_i B^x\sigma^x_i. \tag{4.56}$$

A magnetic field B^x is included such that, in a rotated basis $\sigma^z \rightarrow \sigma^x$, $\sigma^x \rightarrow -\sigma^z$, and (4.56) corresponds to the XY model in its usual basis. The residual spin–phonon couplings are given, to lowest order in η_α by:

$$H_E^{\mathrm{XY}} = -\frac{1}{2}\sum_{\substack{\alpha,\alpha'=z,y \\ i,n,m}} \eta_{i,n}^{\alpha}\eta_{i,m}^{\alpha'}\hbar\omega_{\alpha,n} (a_{\alpha,n}^{\dagger} + a_{\alpha,n})(a_{\alpha',m}^{\dagger} - a_{\alpha',m}) \left[\tilde{\sigma}_i^{\alpha}, \tilde{\sigma}_i^{\alpha'}\right]. \quad (4.57)$$

H_E^{XY} accounts for the interference between the two different conditional forces, which can be avoided by choosing different values for the two radial trapping frequencies, as we explain in the following subsection.

4.2.4 Decoherence induced by vibrational modes

The residual spin–phonon couplings (4.55, 4.57) are a source of decoherence which entangle internal states with phonons. Besides that, internal states are prepared and measured in a different basis than the one corresponding to effective interacting spins. Both effects have to be evaluated to study how the quantum dynamics of internal states departs from the ideal quantum spin Hamiltonian. The problem of solving the quantum dynamics of a system of interacting spins coupled to phonons is indeed quite complicated. We are interested here in estimating the error induced by these couplings, so that we will make use of perturbation theory and several approximations.

Let us consider that the system is initially in a product state of a thermal phonon density matrix, ρ_{ph}, and a given internal pure state, $\rho_i = |\psi_i\rangle\langle\psi_i|$. $|\psi_i\rangle$ evolves to $|\psi_f\rangle$ under the spin Hamiltonian H_S, thus, $|\psi_f\rangle$ represents the ideal simulated spin state. We define the fidelity in the quantum simulation by the overlap between the state of the system after the evolution with the whole Hamiltonian, and $|\psi_f\rangle$:

$$\mathcal{F}(\psi_i) = \langle\psi_f|\mathrm{Tr}_{ph}\{e^{-iHt/\hbar}\ \rho_i \otimes \rho_{ph}\ e^{iHt/\hbar}\}|\psi_f\rangle. \quad (4.58)$$

Having in mind perturbative calculations, let us express the fidelity in the following way:

$$\mathcal{F}(\psi_i) = \langle\psi_i|\mathrm{Tr}_{ph}\{e^{\mathcal{S}(t)}U(t)e^{-\mathcal{S}(0)}\rho_i\otimes\rho_{ph}e^{\mathcal{S}(0)}U(t)^{\dagger}e^{-\mathcal{S}(t)}\}|\psi_i\rangle, \quad (4.59)$$

where $U(t) \equiv e^{iH_0t/\hbar}e^{-i(H_0+H_E)t/\hbar}$, is the evolution operator in the interaction representation with respect to H_E. $H_0 = H_v + H_S$ is the Hamiltonian without

residual spin–phonon coupling. In Eq. (4.59), as well as in the right–hand side of the equations below, all the operators evolve with H_0.

We are particularly interested in the very practical question of how do measurements of internal state observables departure from the averages in the simulated quantum spin models. Let us consider a few–site spin operator, O, and define the error in its average, $E_O = \langle O(t)\rangle - \langle O(t)\rangle_0$, with:

$$\begin{aligned}&\langle O(t)\rangle = \\ &\quad \mathrm{Tr}\{O(t)e^{S(t)}U(t)e^{-S(0)}\rho_i\otimes\rho_{ph}e^{S(0)}U(t)^\dagger e^{-S(t)}\}, \\ &\langle O(t)\rangle_0 = \langle\Psi_f|O|\Psi_f\rangle. \end{aligned} \tag{4.60}$$

Equations (4.59) and (4.60) provide us with a well suited starting point for calculating the effects of the residual spin–phonon coupling in a series in η_α. We show below that these terms can result in negligible contributions with the right choice of parameters. Due to the fact that lowest order spin–phonon couplings are different in each quantum spin model, we consider the two cases separately.

Ising Model

The spin–phonon couplings in (4.55) are proportional to the transverse magnetic field, B^x. In the following we ignore the index α in the vibrational modes, and assume that it corresponds to one of the radial directions. In the most interesting regimes $B^x \approx J$, thus we estimate $B^x \approx \eta^2\omega$. All terms in H_E^{Ising} are non–resonant, such that, if we ignore the contributions from $\mathcal{S}$ in (4.59, 4.60), the only allowed transitions are virtual with probability $E \approx J^2\eta^2/\omega^2 = \mathcal{O}(\eta^6)$.

The most important contribution to the error is thus the one that comes from the canonical transformation only, which can be estimated by setting $U(t) = \mathbf{1}$, expanding $e^{S(t)}$ in (4.59), and keeping terms up to order η^2. In the stiff limit, that is $\beta \ll 1$, we make the additional approximation of considering vibrational modes in (4.59) as localized phonons, and get the following expression for the error to lowest order in η:

$$\begin{aligned} E &= 1 - \mathcal{F} = E^{[0,0]} + E^{[t,t]} - E^{[0,t]} - E^{[t,0]}, \\ E^{[t_1,t_2]} &= \eta^2 \sum_j (\bar{n}e^{i\omega(t_1-t_2)} + (\bar{n}+1)e^{-i\omega(t_1-t_2)}) \times \\ &\qquad \left(\langle\sigma_j^z(t_1)\sigma_j^z(t_2)\rangle - \langle\sigma_j^z(t_1)\rangle\langle\sigma_j^z(t_2)\rangle\right), \end{aligned} \tag{4.61}$$

where $\bar{n}$ is the mean radial phonon number. The error is of order $N\eta^2$, and is proportional to the fluctuations in σ_j^z. Note that equal–time averages give

the dominant contribution in (4.61) because the two–time spin averages in $E^{[0,t]}$ can be neglected at long enough times.

The scaling of E with N results from the fact that $\mathcal{F}$ in (4.59) represents the overlap between the internal state of the ion chain and the effective spin state. However, in practice, local observables like single spin averages or two–site correlation functions are measured. We can show that in this case the error does not increase with N. Let us consider again the effect of the canonical transformation in Eq. (4.60). We get the following error in the measurement of the observable:

$$\begin{aligned} E_O &= E_O^{[0,0]} + E_O^{[t,t]} - 2E_O^{[0,t]}, \\ E_O^{[t_1,t_2]} &= \frac{1}{2}\langle[[O(t), S(t_1)], S(t_2)]\rangle. \end{aligned} \tag{4.62}$$

An explicit expression can be derived from (4.62) which is not very enlightening. However we note again that equal time correlations in (4.62) are the dominant contribution, such that:

$$E_O \approx \frac{1}{2}\eta^2 \sum_j (2\bar{n}+1)\langle[[O(t), \sigma_j^z(t)], \sigma_j^z(t)]\rangle, \tag{4.63}$$

where we have also approximated vibrational modes by localized phonons. It is clear from Eq. (4.63) that if O is an M–site observable, there are only a maximum of M non-vanishing commutators and thus $E \approx M\eta^2\omega$. The most meaningful physical quantities in the study of quantum criticality are indeed one–site (mean values) or two–site (correlation functions) averages, and (4.63) implies that these ones can be studied with an error that is independent on the number of ions.

XY Model

In this case special care has to be paid to the effect of the residual spin–phonon couplings. H_E^{XY} in (4.57) is of order $\eta_\alpha^2\omega_\alpha$, that is, of the same order as $J_{i,j}^{[\alpha]}$ itself. On the other hand, if $\omega_x = \omega_y$, then H_E contains resonant terms that couple vibrational modes in different transverse directions. Under these conditions the effect of H_E is comparable to that of the spin–spin interaction and the quantum simulation is ruined.

A way out of this problem is to tune $\omega_x \neq \omega_y$, with $\omega_x - \omega_y$ of the order of ω_x, ω_y. In this case, there are no resonant terms in (4.57), and the interference between standing–waves in different radial directions is suppressed. The error is then of the order of $(\eta^2\omega_{x,y})^2/(\omega_x - \omega_y) \approx (\eta_x^4, \eta_y^4)$. Indeed, Paul traps are usually designed such that the radial frequencies are different, with

parameters that fulfill the conditions for the rotating terms in H_E^{XY} to be neglected [47]. Under these conditions, the lowest order contribution to the error is, again, the one that comes from the change of basis ($E \propto \eta_\alpha^2 \omega_\alpha$).

4.2.5 Preparation and detection of effective spin states

In the above we discussed the simplest laser configuration for realizing quantum spin models. Adding a transverse field $B^x\sigma^x$ to the simulated Ising interaction $J\sigma_i^z\sigma_j^z$, one could induce a quantum phase transition between the ferromagnetic (antiferromagnetic) ordered ground state and the paramagnetic state. We give here a possible experimental procedure of reaching the effective spin ground states by adiabatic evolution:

1. Initially prepare the ions at the state $|\downarrow\downarrow, \cdots, \downarrow\rangle$ through optical pumping.

2. Apply adiabatically the magnetic field B^x to the ions. The ground state is paramagnetic if $J = 0$: $|\rightarrow\rightarrow, \cdots, \rightarrow\rangle$.

3. Switch on adiabatically the effective spin interaction up to a value of J. Look for quantum phase transitions as J or B^x varies.

4. Measure the ground state through the global fluoresence. The new ground state would be antiferromagnetic if $J \gg B^x$: $|\uparrow\downarrow, \cdots, \uparrow\downarrow\rangle$.

One could repeat the above procedure many times with increasing adiabatically the value of J, and observe the quantum phase transition by the means of global fluorescence, which would show the population of the internal states. The condition for adiabaticity here is

$$\frac{\mathrm{d}J}{\mathrm{d}t}/J \ll \Delta, \tag{4.64}$$

where Δ is the energy gap between the first excited state and the ground state at the quantum phase transition $J \approx B^x$, and its value is approximately $\Delta \approx J/N$.

Furthermore, by switching on nonadiabatically the spin-spin interaction J, one could investigate quantum dynamics out of equilibrium. For example, the Kibble-Zurek mechanism in the antiferromagnetic ground state [129] could be tested or verified in such a clean experimental system.

4.3 Effective Ising model

We have shown that antiferromagnetic long–range Ising models can be realized in experiments with ion traps. Hamiltonian (4.54) is exactly solvable in the case of interaction between nearest–neighbors (NN) [119,118]. In this case, the sign of the interaction is not relevant at all, because the transformation:

$$U = \prod_{j \text{ odd}} \left(\sigma_j^x\right), \quad \sigma_j^z \rightarrow U\sigma_j^z U^{-1} = (-1)^j \sigma_j^z, \tag{4.65}$$

maps the ferromagnetic into the antiferromagnetic model.

The exact solution of the NN–Ising model shows that there exists a quantum phase transition at $B_c^x = J$ [119] between a paramagnetic state ($B^x > J$), and an antiferromagnetic phase ($B^x < J$) characterized by the Néel order parameter:

$$O_N \equiv \frac{1}{N} \sum_j (-1)^j \sigma_j^z. \tag{4.66}$$

We expect that the properties of the effective spin model in ion traps (4.54) are similar to those of the NN–Ising model, due to the fast decay of interactions $J_{i,j} \propto 1/|i-j|^3$; in particular, we expect a quantum phase transition at a given critical value of the longitudinal magnetic field, B_c^x. In the following we present numerical calculations to describe quantitatively the quantum phases of Hamiltonian (4.54), and show that critical properties are very similar to those of the NN–Ising model. Indeed, renormalization group arguments can be used to show that the $1/r^3$ Ising model belongs to the short–range Ising universality class [130]. On the other hand, the long range character of the interactions turns out to induce intriguing effects in the spin quantum correlations which are explained below by means of a spin–wave model.

This numerical problem is handled with the DMRG method [76,77], which is a quasi–exact numerical method for the study of ground states of interacting quantum systems in 1D. The fact that we have further than nearest–neighbor terms increases the complexity of the algorithm by a factor of the number of sites, N. We keep $m = 128$ eigenstates of the reduced density matrix at each step in the DMRG algorithm and test the accuracy of our calculation by comparing its results with the exact solution in the NN–Ising model at the critical point, where DMRG works worst. We have found that the relative error of the ground state energy in this case is limited by the machine accuracy $\delta E \sim 10^{-15}$. One can expect the same accuracy in calculations with the ion trap Ising models presented below because correlations are similar in both cases.

Our numerical calculations describe two types of quantum Ising models:

(i) $1/r^3$–*Ising interaction.*

This case corresponds to a linear array of microtraps, where equilibrium positions of the ions are approximately constant and fixed by the position of the microtrap.

(ii) *Linear trap–Ising model.*

If the trap is in the stiff limit, then effective spin–spin interactions decay like $1/|z_i^0 - z_j^0|^3$, but distances between ions in the Coulomb crystal depend on the position. Thus, we get an effective inhomogenous quantum Ising model with interaction strength $J_{i,j}$ which depends on the position (see Fig. 4.2). The ground state shows the coexistence of different phases in different locations of the ion trap.

The results presented in the following subsections where obtained with chains of $N = 100$ ions. $J_{i,j}$ in the linear trap–Ising model was calculated with $\beta_x = 10^{-2}$, however, our results do not change much with β_x, as long as one considers values within the stiff limit ($\beta_x < 0.1$). If we assume typical values $\omega_x = 10$ MHz, and $\eta^2 = 10^{-2}$, this would correspond to interaction strength $J_{i,i+1} \leq 20$ kHz.

4.3.1 Effective magnetization

In the following we study the effective magnetization and its fluctuations. We will be mainly interested in (i) whether global measurements are enough to characterize quantum phases, and (ii) what is the effect of inhomogeneity and finite size in linear trap models. All our results are presented in energy units J_0, where J_0 is the interaction strength between nearest–neighbors in the $1/r^3$–Ising model, or the averaged nearest–neighbor interaction $1/N \sum_i J_{i,i+1}$, in the case of the linear trap–Ising model, i.e.

$$J_0 = \begin{cases} J_{i,i+1} & (1/r^3 \text{ model}), \\ (1/N)\sum_j J_{i,i+1} & (\text{linear trap model}). \end{cases} \tag{4.67}$$

Transverse ($\langle\sigma^x\rangle$) magnetization.

The mean magnetization, $m^x = (1/N)\langle\sigma_T^x\rangle$ (where $\sigma_T^\alpha = \sum_j \sigma_j^\alpha$), can be obtained from global measurements. In Fig. 4.2 (a) we show the evolution of m_x with the magnetic field. The magnetization curve of the $1/r^3$–Ising model is similar to the NN case. The quantum phase transition results in a discontinuity in $d^2m^x/d(B^x)^2$ (see Fig. 4.3 (a)), something that allows us to locate the critical point $B_c^x(1/r^3) \approx 0.83$, which lies below the critical

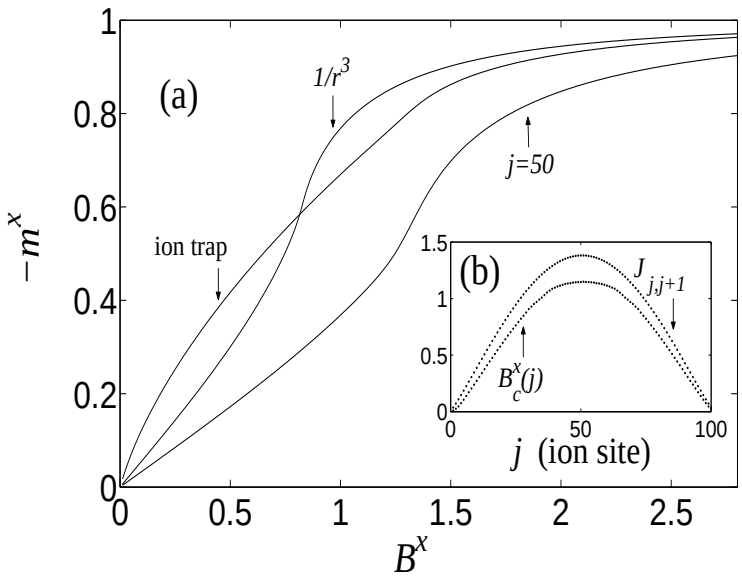

Figure 4.2: (a) Evolution of the averaged effective transverse magnetization in $1/r^3$ and linear trap Ising models (N=100 ions). We also plot $\langle\sigma_j^x\rangle$ in the case of the central ion ($j = 50$) in a linear trap. (b) Local strength of the Ising interaction in a linear ion trap, and local value of the critical field.

point in the NN- Ising model ($B_c^x(NN) = 1$). This effect can be explained in terms of frustration induced by terms $J_{i,j}$, with $(i - j)$ even, which reduces the stability of antiferromagnetic order.

On the other hand, m^x in the linear trap–Ising model departs from the homogeneous $1/r^3$–Ising case, due to the spatial variations in $J_{i,j}$ (see Fig. 4.2 (b)). The system shows the coexistence of different phases, depending on the local value of $J_{i,j}$, as shown in the evolution of the local magnetization $\langle\sigma_j^x\rangle$ with B^x in Fig. 4.3 (b). The local phase diagram at each ion j shows a critical point $B_c^x(j) \approx 0.83 J_{j,j+1}$, which is determined by the local value of the interaction, but satisfies the same relation with $J_{i,i+1}$ found for the homogenous $1/r^3$–Ising model (Fig. 4.2 (b)).

The local phases in a linear ion trap Ising model can be studied with only limited local addressing of the ions. For example, by measuring the average magnetization, m^x, corresponding to the 20 central ions, we can observe the signature of the quantum phase transition, as shown in Fig. 4.3 (a). Thus, individual ion addressing is not necessary for detecting the critical point in the quantum simulation.

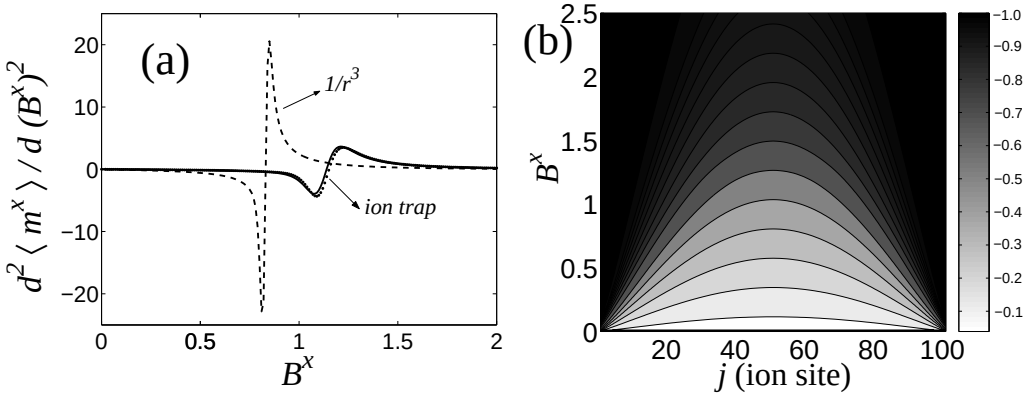

Figure 4.3: (a) Second derivative of m^x as a function of B^x in ion trap Ising models ($N = 100$ ions). Dashed line: $1/r^3$–Ising model. Solid line: average over the 20 central ions in a linear trap–Ising model. Dotted line: central ($j = 50$) ion in a linear trap–Ising model (solid and dotted line are almost on top of each other). (b) Contour plot of $\langle \sigma_j^x \rangle$ on the plane of the coordinate j and the magnetic field B^x.

Longitudinal ($\langle \sigma^z \rangle$) magnetization.

The antiferromagnetic order parameter is given by the staggered magnetization (4.66). In the thermodynamic limit, spontaneous symmetry breaking results in a non–zero value of $\langle O_N \rangle$. On the contrary, in finite systems, symmetry remains unbroken. In this case, it is convenient to study the squared antiferromagnetic order parameter $\langle O_N^2 \rangle$, which takes a value ≈ 1 in the antiferromagnetic phase. In Fig. 4.4, we present the evolution of $\langle O_N^2 \rangle$ in the $1/r^3$–Ising case, as well as in the central region (20 ions) of a linear trap.

For measuring O_N it is necessary to address each ion individually. On the other hand, the fluctuation of the average longitudinal magnetization, $(1/N^2)\langle (\sigma_T^z)^2 \rangle$ is an interesting alternative which does not require individual ion addressing. Antiferromagnetic order can be detected by means of this global observable, because longitudinal spin fluctuations are suppressed in the Néel ordered state, as shown in the case of the $1/r^3$–Ising model (Fig. 4.4).

4.3.2 Correlation functions

Correlation functions $C_{i,j}^{\alpha\alpha} \equiv \langle \sigma_i^\alpha \sigma_j^\alpha \rangle - \langle \sigma_i^\alpha \rangle \langle \sigma_j^\alpha \rangle$ characterize quantum correlations in the ground state of the effective spin system. Even when they play an important role in the description of strongly correlated systems, it is not

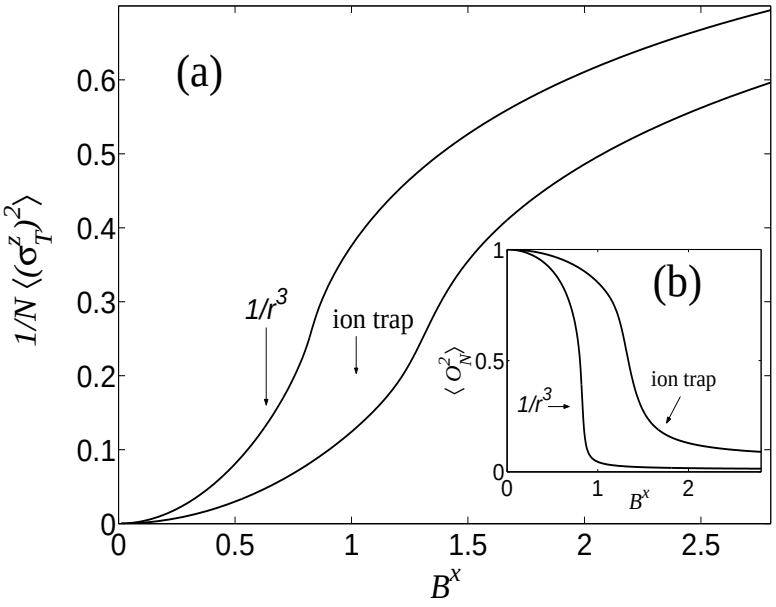

Figure 4.4: (a) Fluctuation of the longitudinal effective magnetization, and (b) Néel order parameter. In both plots we consider the $1/r^3$–Ising model, and the central region (20 ions) of the linear trap–Ising model.

possible to measure them directly in solid–state experimental setups [132]. Trapped ions, on the contrary, offer us the possibility to measure directly equal–time correlation functions by means of a set of measurements on single ions. We show here that realizations of Ising models with trapped ions allow us to test directly properties of quantum critical systems such as the algebraic decay of correlations at a quantum phase transition, as well as remarkable new effects induced by long–range interaction terms.

We consider correlations of observables that are transverse to the order parameter, that is, $C^{xx}_{i,j}$ correlations in the antiferromagnetic phase and $C^{zz}_{i,j}$ correlations in the paramagnetic one, because they are the most meaningful in terms of the spin–wave picture to be introduced later. In Figs. 4.5 and 4.6, it is shown that quantum correlations present two regimes, depending on the distance between ions, $|i-j|$:

Universality regime.

At intermediate distances, correlation functions both in $1/r^3$, and in linear trap–Ising models, show critical properties which are similar to those of the NN–Ising model: $C^{\alpha\alpha}_{i,j} \propto e^{-|i-j|/\xi^{\alpha\alpha}}$ when $B^x \neq B^x_c$, whereas $C^{\alpha\alpha}_{i,j} \propto |i-j|^{-p}$

at B_c^x, with $p = 2$. On the other hand, correlation lengths $\xi^{\alpha\alpha}$ (see Fig. 4.7) diverge near the critical point and show the dependence, $(\xi^{\alpha\alpha})^{-1} \propto |B^x - B_c^x|^\nu$, with $\nu \sim 1$. The critical properties of the $1/r^3$–Ising model are thus the same as those of the nearest–neighbor model [130].

We note that by measuring quantum correlations in the central region of the chain one can measure critical exponents even in the case of the linear–trap Ising model. Finite size effects are however more important in this case (see Fig. 4.6 (b)).

Long-range correlation mediated by the interaction.

A remarkable feature in Figs. 4.5 and 4.6, is that correlation functions decay like a power–law, $C_{i,j}^{\alpha\alpha} \approx 1/|i-j|^3$, at very long distances, so that properties of quantum correlations depart from the nearest–neighbor case (see Fig. 4.5 (b)).

This effect can be qualitatively understood by considering that entanglement between distant ions can be created in two ways: (i) by nearest–neighbor terms in the Hamiltonian, in such a way that correlations present the same characteristics as those of the NN–Ising model (exponential decay), or (ii) directly by long–range terms in (4.54) in such a way that they decay following the power law of the spin–spin interaction. This hand–waving argument will be justified in the following section by means of a spin–wave formalism.

4.3.3 Spin–wave picture

Far away from the critical point, excitations over the ground state can be described as spin–waves satisfying a harmonic Hamiltonian. This picture allows us to understand the numerical results presented above; in particular correlations in the presence of power–law interactions. It also brings ion trap spin models in connection with recent results on quantum correlations and criticality in bosonic gaussian ground states [131].

Spin–waves are defined by the Holstein–Primakoff (HP) transformation [132], whose particular form depends on the ground state. Thus we have two consider separately the two limits corresponding to antiferromagnetic or paramagnetic phases.

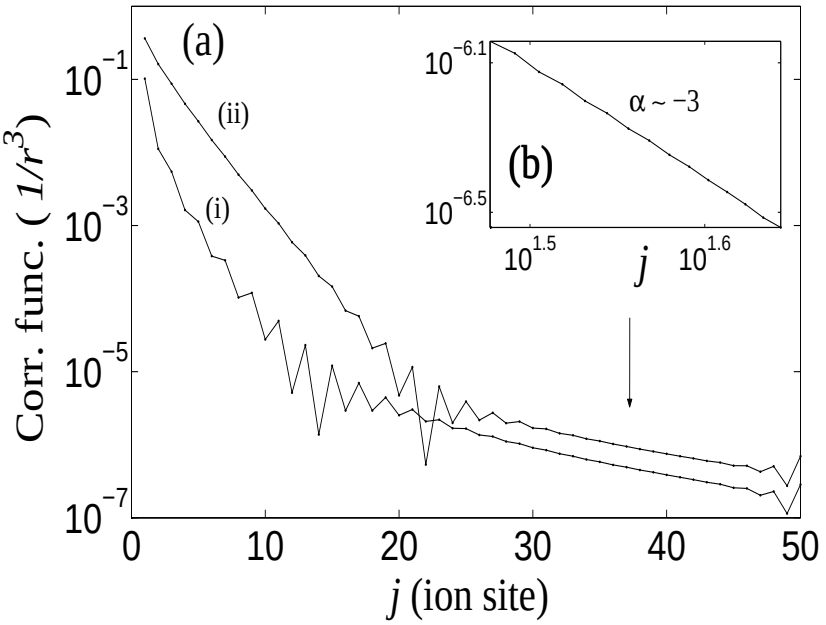

Figure 4.5: (a) Absolute value of correlations, $|C^{\alpha\alpha}_{j_0,j_0+j}|$, between the central ion ($j_0 = 50$) and the rest of a chain with $N = 100$ ions, in the case of the $1/r^3$–Ising model. (i) $C^{xx}_{j_0,j_0+j}$, $B^x = 0.72 < B^x_c$; (ii) $C^{zz}_{j_0,j_0+j}$, $B^x = 1.32 > B^x_c$. (b) Zoom of the long–range tail of C^{zz}, which follows an algebraic decay with an exponent $\alpha = -3$.

$B^x \gg J$

In this phase, HP bosons describe spin–waves excited over the paramagnetic ground state:

$$\begin{aligned} (\sigma^z_j - i\sigma^y_j)/2 &= b^\dagger_j(1 - b^\dagger_j b_j)^{1/2} \approx b^\dagger_j, \\ (\sigma^z_j + i\sigma^y_j)/2 &= (1 - b^\dagger_j b_j)^{1/2} b_j \approx b_j, \\ \sigma^x_j &= 2b^\dagger_j b_j - 1. \end{aligned} \tag{4.68}$$

The harmonic approximation is valid if $b^\dagger_j b_j \ll 1$. In this limit the effective spin Hamiltonian takes the following form:

$$H = \frac{1}{2}\sum_{j,l} J_{j,l}(b^\dagger_j + b_j)(b^\dagger_l + b_l) + B^x \sum_j (2b^\dagger_j b_j - 1). \tag{4.69}$$

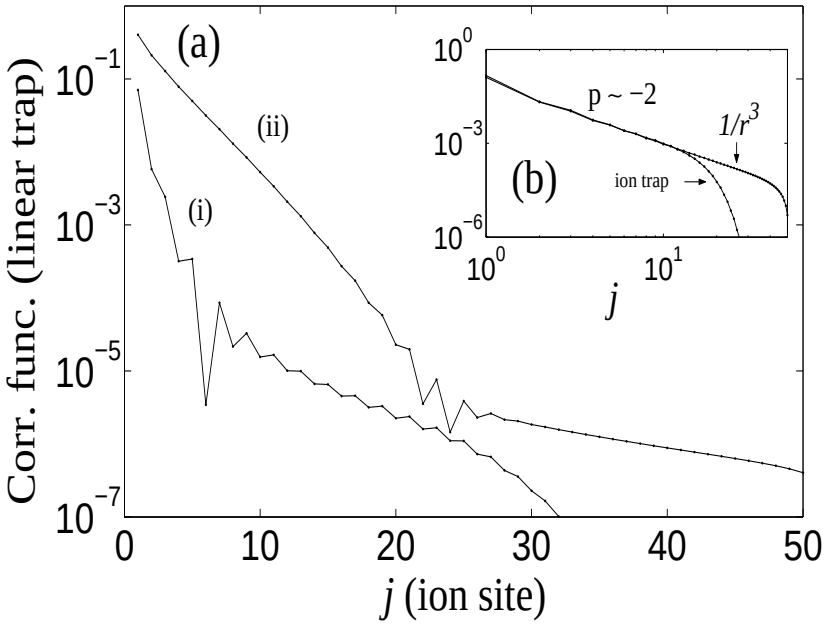

Figure 4.6: (a) Absolute value of correlations, $|C^{\alpha\alpha}_{j_0,j_0+j}|$, between the central ion ($j_0 = 50$) and the rest of a chain with $N = 100$ ions, in the case of the linear trap–Ising model. (i) C^{xx}, $B^x = 0.89 < B^x_c$; (ii) C^{zz}, $B^x = 1.72 > B^x_c$. (b) Plot of $C^{xx}_{j_0,j_0+j}$ for both $1/r^3$ and linear ion trap models, exactly at the critical point $B^x = B^x_c$.

Let us write this Hamiltonian in terms of canonical operators:

$$\begin{aligned} Q_l &= \frac{1}{\sqrt{2}}(b_l^\dagger + b_l), \\ P_l &= \frac{i}{\sqrt{2}}(b_l^\dagger - b_l), \\ H/|2B^x| &= \frac{1}{2}\sum_{j,l} K_{j,l} Q_j Q_l + \frac{1}{2}\sum_j P_j^2, \end{aligned} \tag{4.70}$$

with $K_{j,l} = J_{j,l}/|B^x| + \delta_{j,l}$. In the following we consider the limit $N \to \infty$, so that we can get analytic results. In this limit, Hamiltonian (4.70) is diagonalized by plane–waves, $\tilde{Q}_q = 1/\sqrt{N}\sum_j e^{iqj} Q_j$ and correlation functions

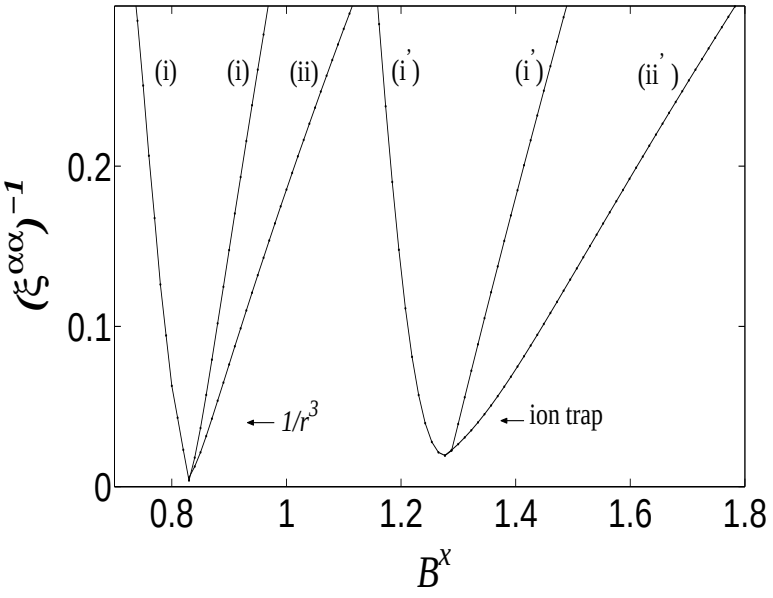

Figure 4.7: Correlation lengths $(\xi^{\alpha\alpha})^{-1}$ as a function of B^x in both $1/r^3$ and linear ion trap models. (i), (i') curves correspond to $(\xi^{xx})^{-1}$, whereas (ii), (ii') correspond to $(\xi^{zz})^{-1}$). ξ^{zz} is not shown in the antiferromagnetic phase because $C^{zz}_{i,j}$ tends to a constant value in the absence of symmetry breaking.

are given by:

$$\begin{aligned} C^{zz}_{0,j} &= 2\langle Q_0 Q_j\rangle = \frac{2}{N}\sum_q e^{-iqj}\langle \tilde{Q}_q \tilde{Q}_{-q}\rangle \\ &= \frac{1}{N}\sum_q e^{-iqj}\frac{1}{\Omega_q}. \end{aligned} \tag{4.71}$$

Ω_q is the spin–wave dispersion relation:

$$\Omega_q^2 = \frac{1}{N}\sum_j K_{j,0}e^{iqj}. \tag{4.72}$$

It is illuminating to write the correlation function in the following way:

$$\begin{aligned} C^{zz}_{0,j} = \langle \sigma^z_0 \sigma^z_j\rangle &= \frac{1}{N}\sum_q e^{-iqj}\Omega_q^2\frac{1}{\Omega_q^3} = \sum_l K_{j,l}A^z_l = \\ & A^z_j + \sum_l \frac{J_{j,l}}{B^x}A^z_l, \end{aligned} \tag{4.73}$$

with:

$$A_j^z = \frac{1}{N}\sum_q \frac{e^{iqj}}{\Omega_q^3} \approx \frac{1}{2\pi}\int_{-\pi}^{\pi} dq \frac{e^{iqj}}{\Omega_q^3}. \quad (4.74)$$

The function $A_j^z \to 0$ as $j \to \infty$, such that for long distances, Eq. (4.73) implies that correlations decay following the spin–spin interaction power law. Indeed, the decay of correlations with the same power–law than the interaction term, has been recently shown to be a general property of ground states of harmonic lattices with long–range interactions [131].

$B^x \ll J$

In this limit the ground state is close to the antiferromagnetic (Néel state), so that we use the following HP transformation:

$$\begin{aligned} (-1)^j\sigma_j^z &= 2b_j^\dagger b_j - 1, \\ (\sigma_j^x + i(-1)^j\sigma_j^y)/2 &= b_j^\dagger(1-b_j^\dagger b_j)^{1/2} \approx b_j^\dagger, \\ (\sigma_j^x - i(-1)^j\sigma_j^y)/2 &= (1-b_j^\dagger b_j)^{1/2} b_j \approx b_j. \end{aligned} \quad (4.75)$$

Signs, $(-1)^j$, have to be added to choose the Néel state as the ground state of the HP oscillators. The Hamiltonian is:

$$\begin{aligned} H &= \frac{1}{2}\sum_{j,l}(-1)^{j-l}J_{j,l}\left(2b_j^\dagger b_j - 1\right)\left(2b_l^\dagger b_l - 1\right) + \\ &\quad B^x\sum_j\left(b_j^\dagger + b_j\right). \end{aligned} \quad (4.76)$$

If we neglect interactions between bosons, then we get a set of non–coupled harmonic oscillators. However, non–quadratic terms in (4.76) induce correlations due to the presence of the transverse field B^x. To see this, we solve first the quadratic part of the bosonic Hamiltonian:

$$H_0 = \sum_j 2\tilde{J}b_j^\dagger b_j + B^x\sum_j\left(b_j^\dagger + b_j\right), \quad (4.77)$$

where $\tilde{J} = -\sum_j(-1)^{j-l}J_{j,l}$, that is, the mean longitudinal magnetic field. Hamiltonian (4.77) is solved by displacing the HP bosons, which corresponds to consider the mean-field ground state as a reference state for the HP transformation:

$$b_j \to b_j - B^x/(2\tilde{J}). \quad (4.78)$$

Up to quadratic terms in the displaced HP bosons, we get the following Hamiltonian:

$$H = 2\tilde{J}\sum_j b_j^\dagger b_j + \left(\frac{B^x}{2\tilde{J}}\right)^2 \sum_{j,l}(-1)^{(j-l)} J_{j,l}\left(b_j^\dagger + b_j\right)\left(b_l^\dagger + b_l\right). \tag{4.79}$$

By following the same steps as in the previous case, we show that:

$$C_{0j}^{xx} = A_j^x + \sum_l (-1)^{j-l}\frac{B^x J_{j,l}}{\tilde{J}^2} A_l^x, \tag{4.80}$$

with A_l^x given by the same function (4.74) of the spin–wave energies that diagonalize (4.77). Thus, to lowest order in $B^x/\tilde{J}$, x–x correlations behave in a similar way as z–z correlations in the antiferromagnetic phase, with the only difference being the alternation in the sign.

Equations (4.73) and (4.80) allow us to understand the interference oscillattions observed in Figs. 4.5 and 4.6 at intermediate distances where the transition occurs between exponential decay and the long-range correlation induced directly by the interaction. If we assume that at short distances correlation functions decay in a way similar to the antiferromagnetic NN Ising model, then the correlation functions are well described by the sum of two contributions:

$$\begin{aligned} C_{i,j}^{zz} &= C_{\rm exp}^{zz}(-1)^{i-j}{\rm e}^{-|i-j|/\xi^{zz}} + C_{\rm int}^{zz} J_{i,j}, \\ C_{i,j}^{xx} &= C_{\rm exp}^{xx}{\rm e}^{-|i-j|/\xi^{xx}} + C_{\rm int}^{xx}(-1)^{i-j} J_{i,j}. \end{aligned} \tag{4.81}$$

In this expression, the decay of the correlation functions in the universal regime has been estimated by making use of the exact results in the ferromagnetic case, and the mapping defined by Eq. (4.65). According to Eq. (4.81), when the magnitude of the two contributions is comparable, they interfere, something that explains the fringes observed in the absolute value of the correlation functions plotted in Figs. 4.5 and 4.6.

Finally, in Fig. 4.8 we show the comparison between results obtained by means of the spin-wave picture and DMRG calculations in both antiferromagnetic and paramagnetic phases. We have checked that the agreement is good far away from the critical point, and gets worse when one approaches it because the assumptions behind the HP approximation are no longer valid.

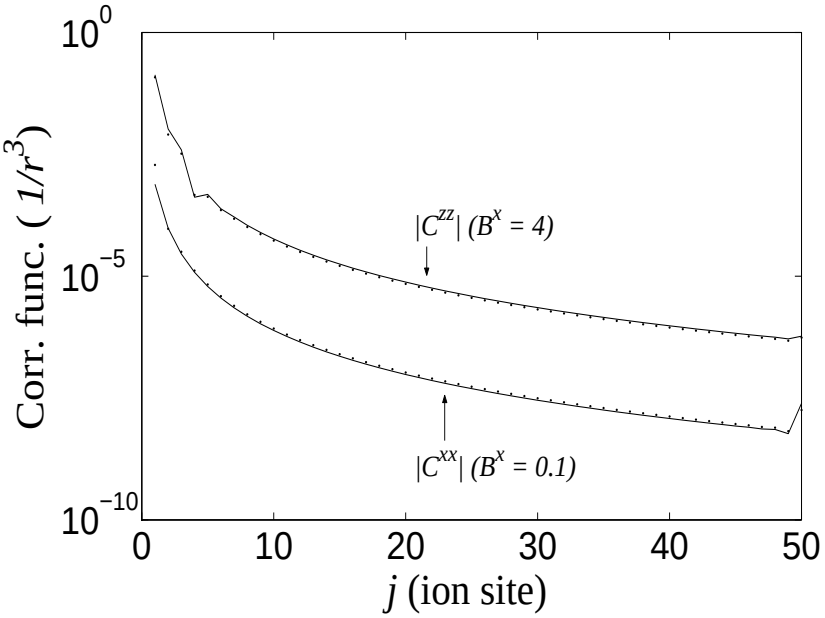

Figure 4.8: (a) Absolute value of correlations $|C^{\alpha\alpha}_{j_0,j_0+j}|$ ($j_0 = 50$, $N = 100$ ions) in the case of the $1/r^3$–Ising model. Points: Numerical results from the DMRG calculations. Solid line: calculation with the HP transformation.

4.4 Effective XY model

We consider the isotropic case of Hamiltonian (4.56), $J^{[x]}_{i,j} = J^{[y]}_{i,j} > 0$. Let us work in the rotated basis defined below Eq. (4.56), with $B^z \to -B^z$:

$$H_S^{\mathrm{XY}} = \frac{1}{2}\sum_{i,j} J_{i,j}(\sigma_i^x\sigma_j^x + \sigma_i^y\sigma_j^y) + \sum_i B^z\sigma_i^z, \tag{4.82}$$

but will keep in mind that in experiments effective spin observables must be measured in the original basis. Note also that $[H, \sum_j \sigma_j^z] = 0$ and hence σ_T^z is a conserved quantity.

The nearest-neighbor (NN) XY model can be exactly solved by a Jordan–Wigner mapping to free fermions [116]. Note that here we consider the antiferromagnetic model, which can be mapped onto the ferromagnetic one by (4.65). The whole region $|B^z|/J < 1$ is critical and $C^{xx}_{i,j}$ follow a power law with critical exponent $\alpha = 1/2$. $\langle\sigma_x\rangle = \langle\sigma_y\rangle = 0$, whereas $\langle\sigma_z\rangle$ grows as a function of B^z up to the non–analytical point $|B^z_c|/J = 1$. One can expect that properties of XY models in trapped ions are similar to those of the NN case.

In this section we study the two cases of $1/r^3$-XY interactions and linear trap-Ising interactions (see the beginning of section (4.3) for a motivation of this distinction) by means of DMRG. $m = 128$ eigenstates of the reduced density matrix are kept, and comparison with the exact solution allows us to estimate a relative error in the calculation of the energy, $\delta E \sim 10^{-13}$. We consider ion chains with $N = 50$ ions, and the same parameters for the ion linear trap, and energy units, considered in the previous section.

4.4.1 Effective magnetization

The most interesting single spin observable is the magnetization in the **z** direction. Here we will follow the same lines and definitions explained in subsection 4.3.1. In Fig. 4.9 we plot the evolution of m^z as a function of B^z. The steps in the curve are due to the finite size of the ion chains. The magnetization curve of the $1/r^3$–XY model follows approximately the same relation as in the nearest–neighbor model:

$$m_z \propto 1 - \frac{2}{\pi} \arccos(-B^z/B_c^z). \tag{4.83}$$

We find again the same effect that in the Ising model, that is, the critical point is shifted $B_c^z(1/r^3)(\approx 0.9) < B_c^z(NN)(= 1)$ due to frustration induced by long-range interaction terms.

On the other hand, in the linear trap-XY model, m^z departs from the homogenous $1/r^3$ case, due again to the variations of the interaction strength along the ion trap. As we did in the case of the Ising model, we get a local phase diagram by plotting the evolution of the single site magnetization as a function of B^z. An interpretation of our results in terms of local quantum phases governed by the local value of $J_{i,j}$ is, however, not justified in this case, because of the existence of long–range correlations in the critical region of the XY model. This fact is shown in the dependence of the local critical field which does not match the spatial profile of the spin–spin interaction (Fig. 4.10 (a)). In both $1/r^3$ and linear trap–XY models, B_c^z can be calculated exactly [133, 134], and the result agrees with our numerical calculation.

A better picture of the linear trap-XY model can be obtained in terms of Jordan–Wigner fermions [118]. If one neglects long-range terms, which lead to fermion-fermion interactions, then σ_j^z corresponds to the local density of Jordan–Wigner fermions, and the evolution of σ_j^z shows the emptying of fermionic levels as $-B^z$ (which plays the role of a chemical potential) is decreased (Fig. 4.10 (b)).

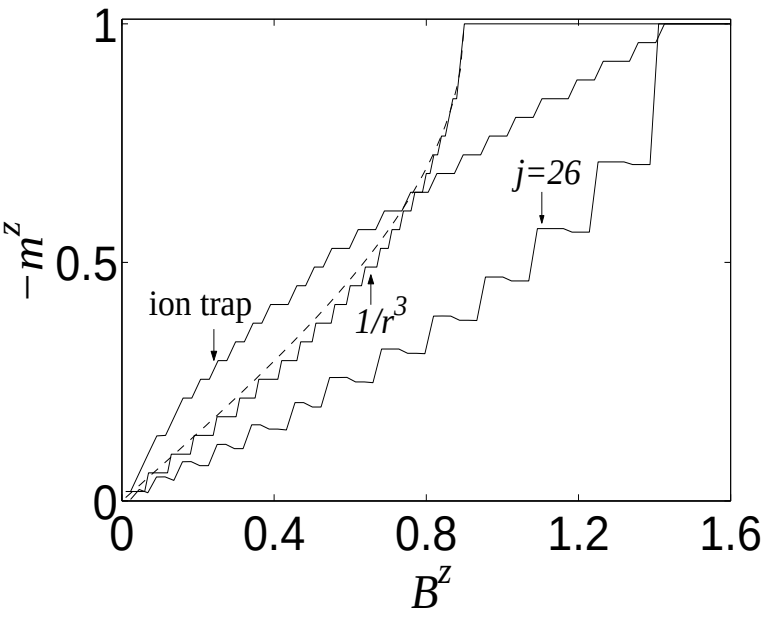

Figure 4.9: Phase diagram of $1/r^3$ and linear trap–XY models. We plot the averaged global magnetization, as well as the evolution of $\langle\sigma_j^z\rangle$ at the center of a linear trap ($N = 50$ ions). The dotted line corresponds to the thermodynamical limit of the NN XY model.

4.4.2 Correlation functions

Our DMRG calculations show that the phase $B^z < B_c^z$ is also critical in both $1/r^3$ and linear trap–XY models, as evidenced in the algebraic decay of $C_{i,j}^{xx} \propto 1/|i-j|^{\alpha}$. In this case, contrary to the Ising model, critical exponents are slightly different than in the NN–XY model, in which $\alpha = 1/2$ (see Fig. 4.11). Note that experiments with linear ion traps can detect the algebraic decay of correlation functions in XY models, even in the presence of the finite size effects induced by variations of $J_{i,j}$.

4.5 Conclusions

In this chapter we have discussed in detail a recent proposal [70] for the realization of quantum spin systems with trapped ions under the action of off-resonant standing waves. Under certain conditions the coupling between internal states and vibrational modes can be written as an effective spin-spin interacting Hamiltonian with a residual spin-phonon coupling. In this way,

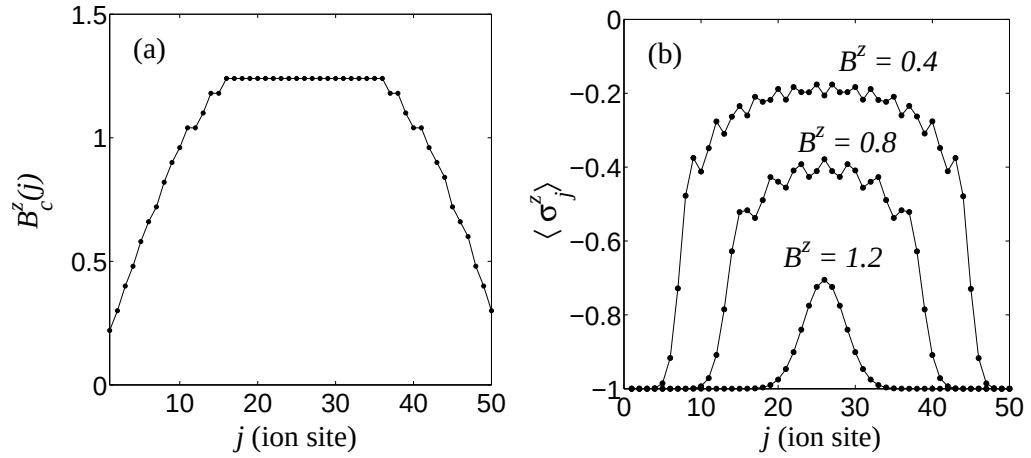

Figure 4.10: (a) Local critical field calculated from the evolution of $\langle \sigma_j^z \rangle$ in the linear trap–XY model. (b) Spatial dependence of $\langle \sigma_j^z \rangle$ in a linear–trap XY model with different values of B^z.

the physics of quantum criticality can be accessed in experiments with ion traps. Our numerical calculations show that:

(i) In the homogeneous $1/r^3$-Ising model, which can be realized with ion microtraps there is a quantum phase transition with critical field $B_c^x \approx 0.83J$, and same critical properties as the nearest–neighbor Ising model.

(ii) In linear ion traps, due to the non-constant separation of the ions, the spin–spin interaction is inhomogeneous, which leads to the coexistence of different quantum phases. However, critical properties can be accessed by measuring each region in the trap separately, which only requires partial ion local measurements (10-20 ions).

(iii) Ion trap Ising models show long–range quantum correlations that are not present in nearest–neighbor models and can be explained by means of a spin–wave theory.

(iv) In the case of the $1/r^3$-XY model the critical field is shifted to a value $B_c^x \approx 0.9$. The quantum phase diagram can be determined by measuring the effective longitudinal magnetization, m^z. Besides that, experiments with trapped ions can access the algebraic decay of correlation functions in the critical phase of XY models.

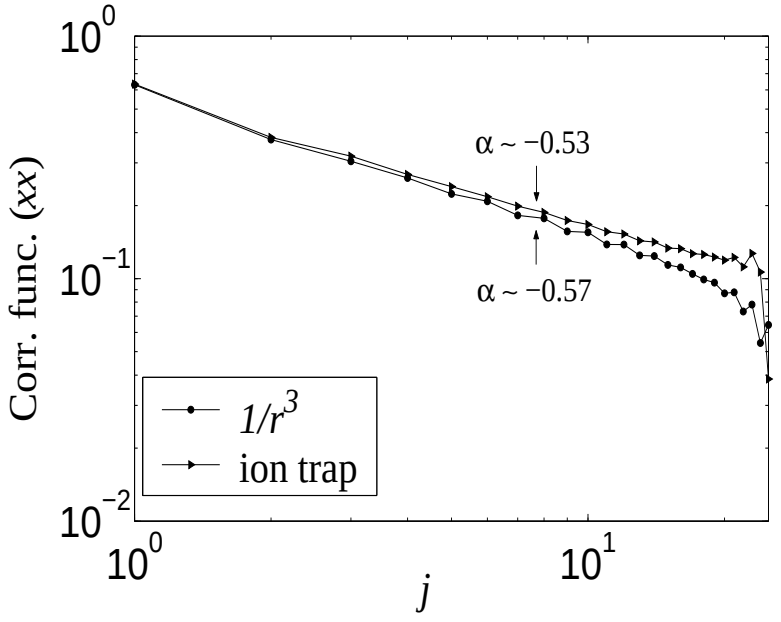

Figure 4.11: Correlation $C^{xx}_{j_0,j_0+j}$ between the central ion $j_0 = 26$ and the rest of the chain in the critical region as a function of ion separation j. $C^{xx}_{j_0,j_0+j}$ is well fitted by a power–lay decay with the exponents α shown in the figure.

Chapter 5

Interacting Phonons in Ion Traps

Cold bosonic atoms in optical lattices is a realization of the Bose–Hubbard Model (BHM) in a clean experimental setup, where one can tune the value of interactions and observe quantum phase transitions in a controlled way [9]. However, in experiments with optical lattices, atoms are separated by optical wavelengths, and thus single particle addressing with optical means is severely limited by diffraction effects.

Trapped ions are also an experimental system with potential applications to the quantum simulation of many–body problems [70, 71, 72, 73, 74, 75], see also Chapter 4. It has the advantage that internal electronic or vibrational quantum states can be measured at the single particle level [47,60], since the distance between ions is large enough to address them individually by optical means. In particular, Ref. [71] has recently shown that the vibrational modes of a chain of trapped ions under suitable experimental conditions follow the quantum dynamics of a BHM. The interaction between phonons is induced by the anharmonicities of an optical potential, which can be created by an off–resonant standing–wave.

In this chapter we present a theoretical study of interacting phonons in trapped ions, and show the following results: (i) The quantum phase transition between a superfluid and a Mott insulator phase can be induced and observed in this system. (ii) Even though finite size–effects are important due to the finite length of the ion chain, properties corresponding to the thermodynamical limit can be accessed in experiments with a limited number of ions. These include critical exponents of correlation functions, and critical values of parameters in the Hamiltonian. (iii) The ability to control phonon–phonon interactions allows us to realize models of interacting bosons which are difficult to reproduce in other experimental setups, like for example,

BHM's with negative interactions, as well as models with site dependent interactions.

The structure of this chapter is the following. In section 5.1 we give an introduction of the Bose-Hubbard model. Then in section 5.2 we derive the Bose–Hubbard model for phonons in a chain of trapped ions, in the presence of the anharmonicities induced by an optical dipole potential. The DMRG algorithm that we have used to study numerically this problem is summarized in section 5.3. In sections 5.4 and 5.5, we study the quantum phases which correspond to repulsive and attractive phonon–phonon interactions, respectively. Section 5.6 is devoted to the case of a Bose–Hubbard model with site–dependent interactions. Finally in the last section we summarize our results and conclusions.

5.1 The Bose-Hubbard model

In this section we review some details of the Bose-Hubbard model that we aim to simulate with ion traps.

5.1.1 The Hamiltonian

The Bose-Hubbard Hamiltonian was introduced in the paper by M. Fisher *et al* [135]. It is defined directly on the 1D lattices, given by

$$H = -t \sum_i (a_i^\dagger a_{i+1} + \text{h.c.}) + U \sum_i n_i(n_i - 1) - \mu \sum_i n_i, \tag{5.1}$$

where $a_i^\dagger$ (a_i) are boson creation (annihilation) operators on sites i, obeying the commutation relation

$$[a_i, a_j^\dagger] = \delta_{ij}, \tag{5.2}$$

and n_i are the boson number operators

$$n_i = a_i^\dagger a_i. \tag{5.3}$$

The first term t describes hopping of bosons from site to site. The second term U represents the simplest repulsive interaction (if $U > 0$) between the on-site bosons. It is possible to be extended to long-range interactions. Finally, the third term μ is the chemical potential of the bosons. The value of μ decides the total number of bosons. One can choose the system either with a fixed chemical potential (at the grand canonical ensemble) or with a fixed total number of bosons (at the canonical ensemble). It is simpler to

consider the system with a fixed chemical potential. However, in our ion-trap case we will consider the system with a fixed total number of phonons.

This Hamiltonian describes the main physics of strongly correlated bosonic systems: the competition between the kinetic potential t and the repulsive interaction potential U. The quantum phase transition from a superfluid to a Mott insulator could occur in this simplest system. There are several ways to study this model: mean field theory (Gutzwiller Ansatz) [119,136,137,138], renormalization group methods [135], strong coupling expansions [139], Quantum Monte Carlo [140], DMRG [141], etc. Below we list some main properties of this Hamiltonian.

5.1.2 Superfluid and Mott insulator states

Assume that the bosonic system contains the fixed number of particles, which is commensurate with the number of lattice sites. We consider here the ground state of the Hamiltonian Eq. (5.1) in two regimes.

When $t \gg U$, the ground state is a superfluid state. The particles are delocalized over all sites: the number of particles per site fluctuates and the coherences between particles on different sites are very large. The ground state of the Hamiltonian at $U = 0$ in an homogeneous system is well described by a macroscopic wave function

$$|\psi_{\mathrm{SF}}\rangle = \frac{1}{\sqrt{N!}}(\frac{1}{\sqrt{M}}\sum_{i}^{M} a_i^{\dagger})^N|0\rangle, \tag{5.4}$$

where N is the total number of particles and M is the number of lattice sites. $|0\rangle$ denotes the vacuum state. In the superfluid state the correlations behave in a power-law decay.

With the increase of the repulsive on-site interaction U, a quantum phase transition from superfluid to Mott insulator takes place at about $U \approx 2t$ at zero temperature. When the interaction dominates the hopping terms, the tunnelling is suppressed, the system tends to have one phonon per site and the particle number fluctuations tend to zero, in order to be in the lowest energy state. The ground state in the Mott-insulator phase is different completely than the superfluid state. It is approximately written as a product of local Fock states:

$$|\psi_{\mathrm{MI}}\rangle = \prod_{i}^{M} \frac{1}{\sqrt{\bar{n}!}}(a_i^{\dagger})^{\bar{n}}|0\rangle, \tag{5.5}$$

where $\bar{n} = N/M$ means the particle number per site. The correlations decay exponentially in the Mott-insulator phase.

5.1.3 Tonks-gas state

Assume that the bosonic system contains a fixed number of particles, which is incommensurate with the number of lattice sites, e.g. $N = M/2$. Taking $U \to \infty$, the Hamiltonian Eq. (5.1) is then describing the hard-core bosons with an infinite on-site repulsive interactions. The states having a finite energy are only the ones with $n_i = 0$ or $n_i = 1$ on every site. Other states with $n_i > 1$ are excluded.

Therefore, this hard-core boson model can be written as a spin–1/2 XX model with nearest-neighbor interactions. The two states with $n_i = 0$ and $n_i = 1$ are associated with the spin up and down states. Identifying

$$\begin{aligned} \sigma_j^x &= a_j + a_j^\dagger, \\ \sigma_j^y &= -i(a_j - a_j^\dagger), \\ \sigma_j^z &= 1 - 2a_j^\dagger a_j, \end{aligned} \tag{5.6}$$

then $\sigma_j^{x,y,z}$ here obey the commutation relations of the Pauli matrices and satisfy $(\sigma_j^\alpha)^2 = 1$. Considering them as Pauli matrices, we have then that the state with all spins up is the state of $n_i = 0$, and the state with all spins down is the state of $n_i = 1$.

Substituting Eq. (5.6) into Eq. (5.1), we have

$$H_{\mathrm{XX}} = -t \sum_i (\sigma_i^x \sigma_{i+1}^x + \sigma_i^y \sigma_{i+1}^y) + \mu \sum_i \sigma_i^z, \tag{5.7}$$

which is the quantum XX model we were talking about in Chapter 4. The behaviors in the Tonks-gas phase are the same as the quantum XX model, which can be exactly solved.

5.2 Phonon-Hubbard model in ion traps

In this section we show that under certain experimental conditions, the dynamics of the vibrational modes of a chain of ions satisfies the Bose-Hubbard model of interacting phonons in a lattice [71]. Phonon number conservation is ensured whenever vibrational energies are much higher than other energy scales in the system. In this limit, physical processes which involve creation or destruction of a phonon do not conserve particle number and are suppressed in much the same way as processes which do not conserve the number of electrons or atoms in low–energy physics.

5.2.1 Harmonic and phonon conserving approximation

Let us start by writing the Hamiltonian that describes a chain of ions in a linear trap:

$$H_0 = \sum_{i=1}^{N} \frac{\vec{P}_i^2}{2m} + V_{\mathrm{T}} + \sum_{\substack{i,j=1 \\ (i>j)}}^{N} \frac{e^2}{|\vec{R}_i - \vec{R}_j|}. \tag{5.8}$$

N is the number of ions, and m is their mass. $\vec{P}_j$ and $\vec{R}_j$ are the momenta and the absolute positions of the ions, respectively. V_{T} is the trapping potential, which determines the ions' equilibrium positions. In this work we deal with two different situations. On one hand we consider the case of ions in a linear Paul trap, where they are confined by an overall trapping potential:

$$V_{\mathrm{T}} = \frac{1}{2} m \sum_{i=1}^{N} \sum_{\alpha=x,y,z} \omega_\alpha^2 R_{i,\alpha}^2, \tag{5.9}$$

where ω_α are the trapping frequencies in each spatial direction. On the other hand, we consider ions confined by an array of separate microtraps:

$$V_{\mathrm{T}} = \frac{1}{2} m \sum_{i=1}^{N} \sum_{\alpha=x,y,z} \omega_\alpha^2 \left(R_{i,\alpha} - \bar{R}_{i,\alpha}\right)^2, \tag{5.10}$$

where $\bar{R}_{j,\alpha}$ are the centers of each microtrap. Note that in (5.10) we assume that the confinement is strong enough, such that each ion feels only a single microtrap.

The equilibrium positions of the ions are given by the minima of the trapping potential plus the Coulomb repulsion. From now on, we choose the condition $\omega_z \ll \omega_x, \omega_y$, such that the ion chain is along the **z** axis, with equilibrium positions given by z_i^0. In the case of a linear Paul trap, described by Eq. (5.9), the equilibrium positions of the ions have to be calculated numerically. The distance between ions is smaller at the center of the chain. In the case of independent microtraps (Eq. (5.10)), one can approximate the equilibrium positions by assuming that they correspond to the center of each microtrap: $z_i^0 = \bar{R}_{i,z}$. This fact has strong implications for the phonon quantum dynamics, as we will see below.

In the harmonic approximation, H_0 is expanded up to second order in the displacements of the ions around the equilibrium positions, and we get a set of independent vibrational modes corresponding to each spatial direction. The phonon number is a conserved quantity if the vibrational energies are the largest energy scale in the system. This condition can be met either in the

case of ions in individual microtraps, or in the case of the radial vibrations of ions in a linear trap, because the corresponding trapping frequencies can be increased without destroying the stability of the ion chain. For concreteness we restrict from now on to the case of vibrations in one of the radial directions, say **x**, but keep in mind that our results can be applied also to the axial vibrational modes if ions are in individual microtraps.

The Hamiltonian that governs the dynamics of the radial coordinates in the harmonic approximation reads:

$$\begin{aligned} H_{\mathrm{x0}} = \sum_{i=1}^{N} \frac{P_{i,x}^2}{2m} &+ \frac{1}{2} m\omega_x^2 \sum_{i=1}^{N} x_i^2 \\ &- \frac{1}{2} \sum_{\substack{i,j=1 \\ (i>j)}}^{N} \frac{e^2}{|z_i^0 - z_j^0|^3} \left(x_i - x_j\right)^2 , \end{aligned} \tag{5.11}$$

where x_i are the displacements of the ions around the equilibrium positions, that is, simply $x_i = R_{i,x}$, and $P_{i,x}$ the corresponding momenta. The second quantized form of this Hamiltonian is (we consider units such that $\hbar = 1$):

$$H_{\mathrm{x0}} = \sum_{i=1}^{N} \omega_{x,i} a_i^\dagger a_i + \sum_{\substack{i,j=1 \\ (i>j)}}^{N} t_{i,j} \left(a_i^\dagger + a_i\right) \left(a_j^\dagger + a_j\right). \tag{5.12}$$

$a_i^\dagger$ (a_i) are creation (annihilation) operators for phonons in the radial direction. Harmonic corrections induced by the Coulomb interaction determine the effective trapping frequency, $\omega_{x,i}$ which depends on the ions' positions, as well as the tunneling amplitudes $t_{i,j}$:

$$\omega_{x,i} = \omega_x - \frac{1}{2} \sum_{\substack{j=1 \\ (j\neq i)}}^{N} \frac{e^2/(m\omega_x^2)}{|z_i^0 - z_j^0|^3} \, \hbar\omega_x, \tag{5.13}$$

$$t_{i,j} = \frac{1}{2} \frac{e^2/(m\omega_x^2)}{|z_i^0 - z_j^0|^3} \, \hbar\omega_x. \tag{5.14}$$

Eq. (5.13) yields an important result on the properties of phonons in trapped ions: the corrections to the local trapping energy, $\omega_{x,i}$ may depend on the position of the ions, in case the distance between ions changes along the chain. In [71] we have shown that in a linear ion trap, ions arrange themselves in a Coulomb chain, such that $\omega_{x,i}$ is an effective harmonic confining potential for the phonons. On the contrary, in the case of an array of ion microtraps,

the distances between ions can be considered to be approximately constant, and thus this confining effect does not take place.

Before going any further, let us study under which conditions phonon nonconserving terms can be neglected in Eq. (5.12). We define the parameter:

$$\beta_x = e^2/(m\omega_x^2 d_0^3), \tag{5.15}$$

where d_0 is the distance between ions. Since we will be interested in the limit $\beta_x \ll 1$, we choose d_0 to be the minimum distance between ions in the case of a linear Paul trap. Phonon tunneling terms $t_{i,j}$ are of the order of t, defined by:

$$t = \beta_x \omega_x / 2. \tag{5.16}$$

Since phonon nonconserving terms rotate fast in (5.12), we can neglect them in a rotating wave approximation if:

$$t/\omega_x = \beta_x/2 \ll 1. \tag{5.17}$$

In our numerical calculations, we will parameterize the tunneling of phonons between sites by the parameter t, which corresponds, due to the definition of β_x, to the highest value of the tunneling along a chain in the case of a linear Paul trap, and to the tunneling between nearest–neighbors in the case of an array of microtraps.

5.2.2 Phonon–phonon interactions

Anharmonic terms in the vibrational Hamiltonian are interpreted as phonon–phonon interactions, and can be induced by placing the ions at the minimum or maximum of the optical dipole potential created by an off–resonant standing wave along **x**:

$$H_{\rm sw} = F \sum_{i=1}^{N} \cos^2(kx_i + \frac{\pi}{2}\delta). \tag{5.18}$$

F is the amplitude of the dipole potential, and δ determines the position of the ions relative to the standing wave. We define the Lamb–Dicke parameter $\eta = kx_0$, where k is the wave–vector of the standing wave lasers, and x_0 is the ground–state size of the radial trapping potential. The only relevant cases for us are $\delta = 0$ (maximum of the optical potential), and $\delta = 1$ (minimum). Under the condition $\eta \ll 1$, we can write $H_{\rm sw}$ as a series around $x_i = 0$. The term that is quadratic in x_i in Eq. (5.18) can be included in the harmonic vibrational Hamiltonian just by redefining the global radial trapping frequency:

$$\omega_x^2 \rightarrow \omega_x \left(\omega_x - (-)^\delta 4\eta^2 F\right). \tag{5.19}$$

In the case $\delta = 0$, condition $\eta^2 F \ll \omega_x$ has to be fulfilled, such that the radial trapping frequency is not strongly suppressed by the standing wave, and the system remains in the phonon number conserving regime. Under this condition the only relevant term is thus the quartic one:

$$H_{\rm sw}^{(4)} = (-1)^{\delta} \frac{F\eta^4}{3} \sum_{j=1}^{N} \left(a_j + a_j^{\dagger} \right)^4 . \tag{5.20}$$

We can neglect nonconserving phonon terms again under the condition $F\eta^4 \ll \omega_x$. In this way we get, finally, the promised BHM for phonons:

$$\begin{aligned} H_{\rm x}^{\rm BHM} &= \sum_{\substack{i,j=1 \\ i>j}}^{N} t_{i,j} (a_i^{\dagger} a_j + h.c.) \\ &+ \sum_{i=1}^{N} (\omega_x + \omega_{x,i}) a_i^{\dagger} a_i + U \sum_{i=1}^{N} a_i^{\dagger 2} a_i^2 . \end{aligned} \tag{5.21}$$

The on–site interaction is given by:

$$U = 2(-1)^{\delta} F\eta^4 . \tag{5.22}$$

Thus, it is repulsive or attractive depending on whether the ions are placed at a minimum or maximum of the standing-wave, respectively.

5.2.3 Preparation and detection of SF and MI states

According to the properties of the BHM, one could propose experimental sequences to create the superfluid-Mott insulator quantum phase transition. A possible experimental procedure is given below:

1. Initially prepare the vibrational modes of the string of ions in the state with zero phonons. This could reached by laser cooling.

2. Under the condition $U \gg t$, create the ground state of the phonon system by means of sequences of blue/red sideband transitions. The generated ground states of the phonon system here are Fock (Mott-insulator)states localized at each ion.

3. Vary the value of U adiabatically down to a given value U_c. The adiabatical evolution means that the phonon system remains in the ground state. At a critical point value $U_c \approx 2t$, the system undergoes a transition to a phonon superfluid.

4. Measure the ground state of the phonon system by the method explained in Chapter 2.

We get the information of phonons by measuring the internal states of the ions, since they are coupled each other. For example, one can apply a blue sideband pulse for a time t and measure the photoluminescence from each ion [60]. Repeat many times to get the averaged photoluminescence, which is straightforward representing the probability of finding the ion in the ground internal state,

$$P_g(t) = \sum_n \left[\cos(\frac{\Omega}{2}\sqrt{n+1}\eta t)\right]^2 P(n), \tag{5.23}$$

where Ω is the Rabi frequency, η is the Lamb-Dicke parameter, and $P(n)$ is the probability of having n phonons. In this way by measuring $P_g(t)$ one could get the corresponding $P(n)$. Then, the variations of the phonon density along the chain will give a signature of superfluid-Mott insulator transition.

Finally, the complete phonon density matrix would be obtained by means of quantum tomography [47].

5.3 Numerical method

The Bose–Hubbard Model with tunneling between nearest–neighbors has been thoroughly studied in the past [119, 135]. It has recently received considerable attention because it describes experiments with ultracold atoms in optical lattices. In general, we expect the same phenomenology to appear in our problem, such as, for example, a superfluid–Mott insulator quantum phase transition. However, the situation of phonons in ion traps presents a few peculiarities that deserve a careful analysis: the effects of long–range tunneling in (5.21), finite size effects, as well as the possibility of having attractive interactions.

To handle this many–body problem numerically we use the DMRG method [76, 77], which has proved to be a quasi–exact method in quantum chains. In particular we use the finite-size algorithm for open boundary conditions. Our problem is defined in the microcanonical ensemble, that is, we find the minimum energy state within the Hilbert subspace with a given number of total phonons $N_{\rm ph}$. For this reason, we have implemented a DMRG code which uses the total phonon number as a good quantum number and projects the problem into the corresponding subspace at each step in the algorithm [96].

To keep a finite dimensional Hilbert space, we truncate the number of phonons in each ion, and define a maximum value n_{max}, which is usually

taken to be of the order of $6\langle n\rangle$, with $\langle n\rangle$ the mean phonon number. The number of eigenstates of the reduced density matrix that we keep at each step is always in the range $80 - 100$.

We have checked the accuracy of our method by comparing our numerical calculations with the exact solution in the case of a system of non–interacting ($U = 0$) phonons, where the ground state at zero temperature is a condensate of phonons in the lowest energy vibrational state. We have also compared our numerical results with exact diagonalizations of Eq. (5.21) with up to $N = 5$ ions. In both cases we found agreement between DMRG and the exact results up to machine accuracy $\delta E \sim 10^{-14}$.

The relevant experimental parameters of our phonon-Hubbard model are discussed in the Ref. [71]. Typically we could choose the minimum distance between ions $d_0 = 5\mu m$ and $\beta_x = 2 \times 10^{-2} \ll 1$. Then we have $\omega_z \approx 177$kHz and $\omega_x \approx 12.5$MHz for a string of ions with $N = 50$. The number of phonons is $N_{ph} = N$ for the superfluid and Mott-insulator phases and $N_{ph} = N/2$ for the Tonks-gas phase. In the end we discuss $N_{ph} = 2N$ for a special case with site-dependent interactions. All our calculations are for the ground state, i.e. at zero temperature.

Following the discussion below Eqs. (5.13, 5.14), one expects to find significant differences between the cases of phonons in ions trapped in a linear trap (Coulomb chain), and phonons in an array of ion microtraps. Finite size and inhomogeneity effects are indeed much more important in the linear trap case, since harmonic Coulomb corrections induce an effective harmonic trapping for the phonon field. For this reason, we always study these two cases separately, in the different quantum phases that we will explore in what follows.

5.4 Repulsive interactions: $U > 0$

We study first the quantum phases of phonons with $U > 0$, and both commensurate and incommensurate total phonon number. In this section we present results for a chain with $N = 50$ ions, and total phonon number $N_{\rm ph} = N$ in the commensurate case, or $N_{\rm ph} = N/2$ in the incommensurate case.

The local observables that we consider are the number of phonons at each site, $n_j = \langle a_j^\dagger a_j\rangle$, as well as its fluctuations, $\delta n_j = \sqrt{\langle n_j^2\rangle - \langle n_j\rangle^2}$. Two–point correlation functions have to be defined carefully, to take into account finite size effects, for example, the variations of the density of phonons along the

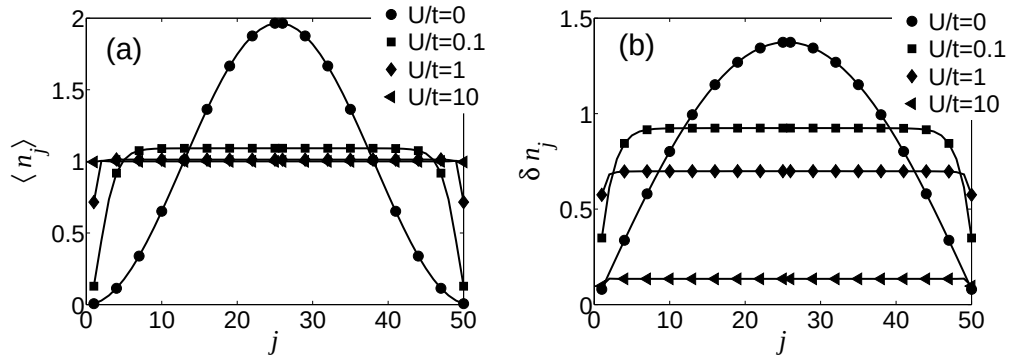

Figure 5.1: (a) Mean phonon number $\langle n_j \rangle$, and (b) fluctuations δn_j, at each ion in the phonon ground state in an array of microtraps. Number of ions $N = 50$, and total phonon number $N_{\rm ph} = 50$.

chain. Correlations in the number of phonons are given by:

$$C_{i,j}^{nn} = \langle n_i n_j \rangle - \langle n_i \rangle \langle n_j \rangle. \tag{5.24}$$

A suitable definition of correlations that are non–diagonal in the phonon number basis is the following one [142]:

$$C_{i,j}^{aa} = \frac{\langle a_i^\dagger a_j \rangle}{\sqrt{\langle n_i \rangle \langle n_j \rangle}}, \tag{5.25}$$

such that correlations are rescaled by local values of the phonon density. The rescaling is inspired by the decomposition of the phonon field in density and phase operators, $a_j = \sqrt{n_j} e^{-i\phi_j}$, which is the starting point for the Luttinger theory of the weakly interacting bosonic superfluid [143, 144, 145].

In Figs. 5.1 and 5.2, we plot the local density and its fluctuations in the cases of an array of microtraps, and a linear Paul trap, respectively. These figures show a signature of the different phases which can be observed in the model defined by the Hamiltonian (5.21). Figs. 5.1(a) and 5.2(a), in particular, show the variation of the density of phonons along the chain. The evolution of the density profile shows the transition from the phonon superfluid to the Mott–insulating phase. When $t \gg U$, the ground state of the system is a condensate such that all the phonons occupy the lowest energy vibrational mode. In the case of a linear Paul trap, phonons are confined in the center of the chain, due to the effective trapping potential induced by the nonconstant ion–ion distance. At $U \gg t$, the ground state is a phonon Mott insulator with approximately one phonon per site, and no phonon number

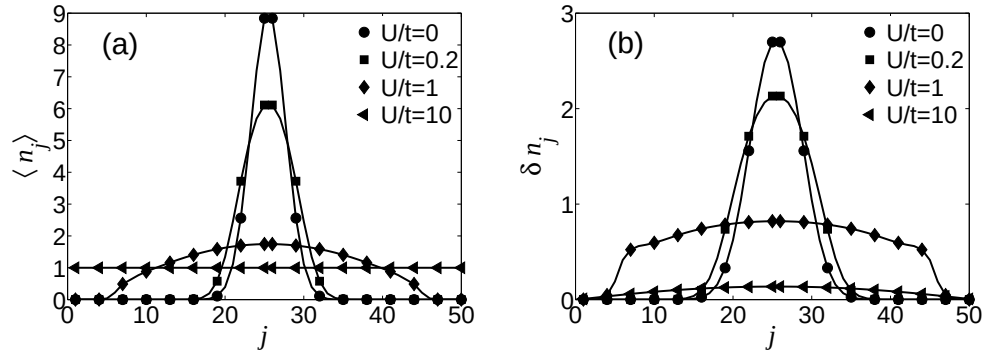

Figure 5.2: (a) Mean phonon number and (b) fluctuations, at each ion in the phonon ground state in a linear Paul trap. $N = 50$, $N_{\rm ph} = 50$.

fluctuations. Note that due to the effective harmonic trapping potential, the Mott phase in the whole chain is reached for lower values of U in the case of the array of microtraps (Fig. 5.1) than in the linear Paul trap case (Fig. 5.2).

In the following subsections, we study these two quantum phases separately, paying particular attention to their correlation functions.

5.4.1 Superfluid phase

When the tunneling dominates the on–site interactions, the system is in the superfluid phase[1]. The non-interacting ground state is given by a condensate solution in which the $N_{\rm ph}$ phonons are in the lowest vibrational mode:

$$|\psi_{SF}\rangle = \frac{1}{\sqrt{N_{\rm ph}!}} \left(\frac{1}{\sqrt{N}} \sum_i \mathcal{M}_i^0 a_i^\dagger \right)^{N_{\rm ph}} |0\rangle, \tag{5.26}$$

where $\mathcal{M}_i^0$ is the wave–function of the lowest energy vibrational mode. Interactions suppress long range order in 1D, even in the weak interacting limit, $U \ll t$, in which Luttinger liquid theory allows us to make predictions on the

[1]Note that long–range order is destroyed by quantum fluctuations even at zero temperature in one spatial dimension. However we use here the usual terminology in lattice models, and choose the term "superfluid phase" for the quantum phase $U < U_c$ of the Bose–Hubbard model. This phase does not show long–range order, but algebraic decay of the phase correlations.

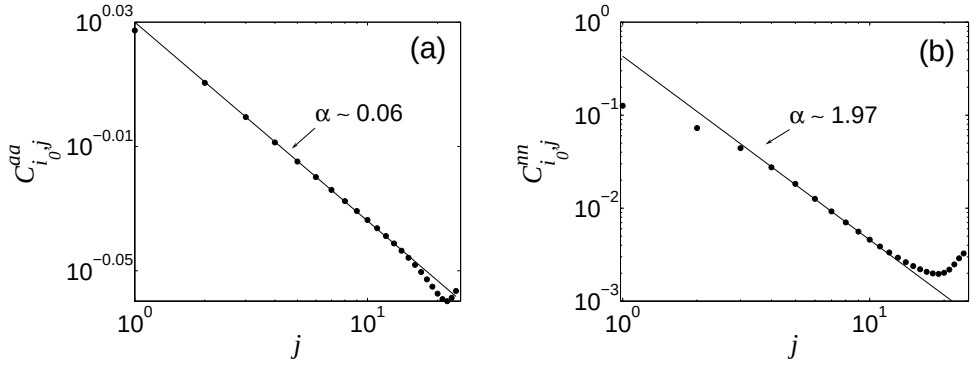

Figure 5.3: Correlation functions (a) $C^{aa}_{i_0,j}$ and (b) $C^{nn}_{i_0,j}$ as a function of coordinate j, at the superfluid phase ($U/t = 0.1$) in an array of ion microtraps. We choose $i_0 = 26$ (center of the chain), $N = N_{\rm ph} = 50$. The dotted and solid lines are numerical results and fittings in the region where the functions show algebraic decay.

scaling of correlation functions:

$$\begin{aligned} C^{aa}_{i,j} &\propto |i-j|^{-\alpha}, \\ C^{nn}_{i,j} &\propto |i-j|^{-2}, \end{aligned} \tag{5.27}$$

where α depends on the parameters of the model:

$$\alpha \propto \sqrt{\frac{U/t}{n_0}}. \tag{5.28}$$

In deriving (5.27) one has to neglect phonon tunneling beyond nearest–neighbor ions, and assume an homogeneous system [143]. In the following we will check if Luttinger theory describes also our numerical results in the case of phonons in a chain of trapped ions, by fitting our results to the form (5.27).

(1) Array of microtraps. We start with the case of the superfluid phase in an array of ion microtraps, see Fig. 5.3. Correlation functions $C^{aa}_{i,j}$ and $C^{nn}_{i,j}$ decay algebraically in an intermediate range of ion–ion separations, with exponents which satisfy the predictions of Luttinger theory. In particular, the evolution of α in Eq. (5.27) is well described by the Luttinger liquid scaling law (5.28), as shown in Fig. 5.4.

(2) Linear ion trap. In the case of ions in a linear Paul trap, finite size effects play a more important role, because of the inhomogeneities of the on–site phonon energy. Correlation functions still decay algebraically for short

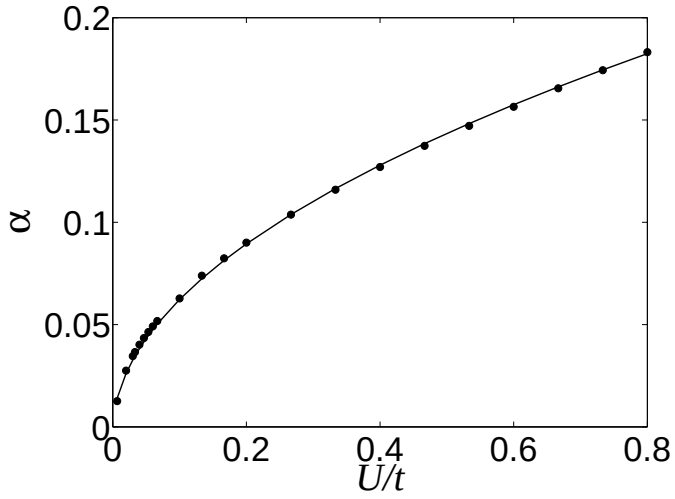

Figure 5.4: The evolution of the exponent α of $C^{aa}_{i_0,j}$ as a function of U/t in the regime of superfluid phase, in an array of ion microtraps ($i_0 = 26$, $N = N_{\rm ph} = 50$). The dotted line is from numerical data, and the solid line the fitting result from the Luttinger liquid, that is, $\alpha \approx A\sqrt{\frac{U/t}{n_0}}$, where the coefficient $A \approx 1.68$.

distances in the superfluid regime, but boundary effects spoil this behavior at large separations between ions. In the algebraic regime, exponents are close to those predicted by Luttinger theory in the homogeneous case, see Figs. 5.5 and 5.6.

Due to the localization of phonons as we increase U/t, a Mott insulator phase appears first at the sides of the ions chain, which coexists with a superfluid core at the center. This coexistence of the phases can be observed in the correlation functions, which show regions of algebraic or exponential decay, as shown in Fig. 5.7.

5.4.2 Mott-insulator phase

In the commensurate case, by increasing the on-site interaction U, a quantum phase transition from a superfluid to a Mott-insulator state takes place at about $U \approx 2t$. In the limit in which interaction dominates over hopping, the ground state for a commensurate filling of $\bar{n}$ particles per site is simply a

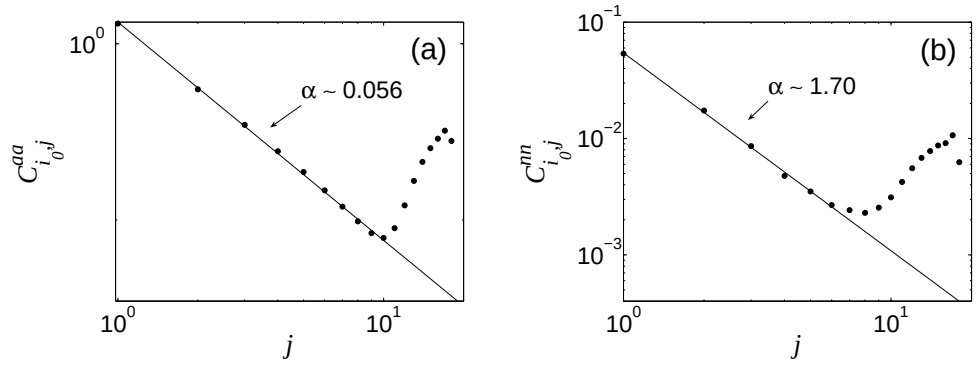

Figure 5.5: Correlation functions (a) $C^{aa}_{i_0,j}$ and (b) $C^{nn}_{i_0,j}$ at the superfluid phase $U/t = 0.2$ in a linear Paul trap ($N = N_{\rm ph} = 50$). The dotted lines are numerical data, and the solid lines are fittings in the region where the correlations decay algebraically.

product state of local phonon Fock states,

$$|\psi_{MI}\rangle = \prod_{i=1}^{N} \frac{1}{\sqrt{\bar{n}!}} (a_i^\dagger)^{\bar{n}} |0\rangle. \tag{5.29}$$

In the Mott insulator phase correlations decay exponentially with distance, $C^{aa,nn}_{i,j} \propto \mathrm{e}^{-|i-j|/\xi}$, where ξ is the correlation length. The correlation length diverges when approaching the quantum phase transition.

(1) Array of ion microtraps. In Fig. 5.8 (a) we plot the correlation functions in the phonon Mott phase in the case of an array of ion microtraps. These curves can be fitted to an exponential decay, and the correspond correlation lengths are plotted in Fig. 5.8 (b) as a function of the interaction strength. Due to the finite size of the system, ξ does not diverge at the critical value of U. However, the extrapolation of the curves in the linear regime allows us to estimate the critical point, which lies at $U_c/t \approx 1.55$. This critical value is smaller than the one in the BHM with tunneling between nearest–neighbors only, $U_c^{nn}/t \approx 2$. The condition $U_c < U_c^{nn}$ is due to the frustration induced by hopping between next–nearest–neighbors, which makes the superfluid phase more unstable against the effect of on–site interactions.

(2) Linear ion trap. In the case of a linear trap, the behavior of spatial correlations is similar, see Fig. 5.9. $C^{nn}_{i,j}$ is difficult to fit due to the few points with exponential decay, therefore we only plot the correlation length corresponding to $C^{bb}_{i,j}$. Due to the effective phonon trapping potential, the Mott insulator and superfluid phases coexist in a range of values of U (Fig.

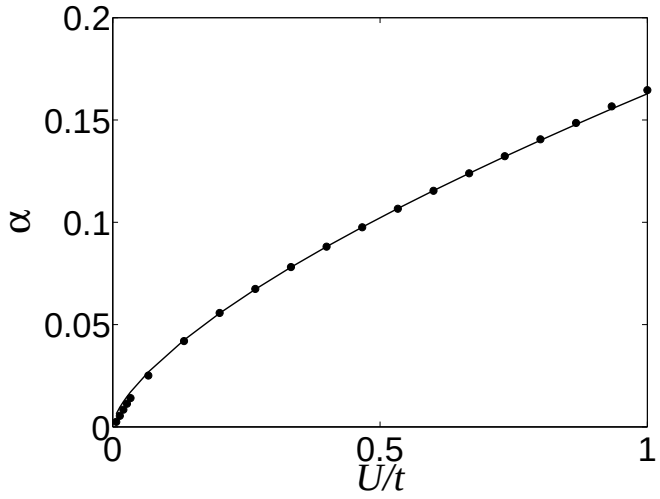

Figure 5.6: The evolution of the parameters α in $C^{aa}_{i_0,j}$ with U/t. The dotted line is the values from the correlation, and the solid line is the fitting data from $\alpha \approx 0.215\sqrt{\frac{U/t}{n_0}}$, corresponding to the Luttinger liquid theory.

5.7). For this reason, in the case of a linear Paul trap, one cannot follow the extrapolation procedure of Fig. 5.8 to find a critical value of the interaction.

Finally, in the Mott-insulator phase the long-range hopping terms which decay like $1/|z^0_i - z^0_j|^3$ play a major role, since they induce a peculiar long-range correlation in this phase. In Fig. 5.10, we show that $C^{aa}_{i,j}$ indeed also behaves like $1/|z^0_i - z^0_j|^3$ at long distances. The existence of power–law decay in correlation functions of non–critical systems due to long–range interactions was also observed in the case of spin models in trapped ions, see the discussion in Ref. [72].

5.4.3 Tonks-gas phase

We turn now to the incommensurate filling case, where in the limit $U \gg t$ the system forms a Tonks-Girardeau gas, which can be described in terms of effective free fermions. A Tonks-Girardeau gas has recently been realized in the experiments with ultracold bosons in an optical lattice [33, 35].

(1) Array of ion microtraps. We have studied numerically the Tonks–Girardeau regime in the case of phonons in ion traps, starting with the case of an array of ion microtraps with $N = 50$ sites and $N_{ph} = 25$ phonons, that is, 1/2 filling. The density of phonons evolves from a superfluid to a Tonks-

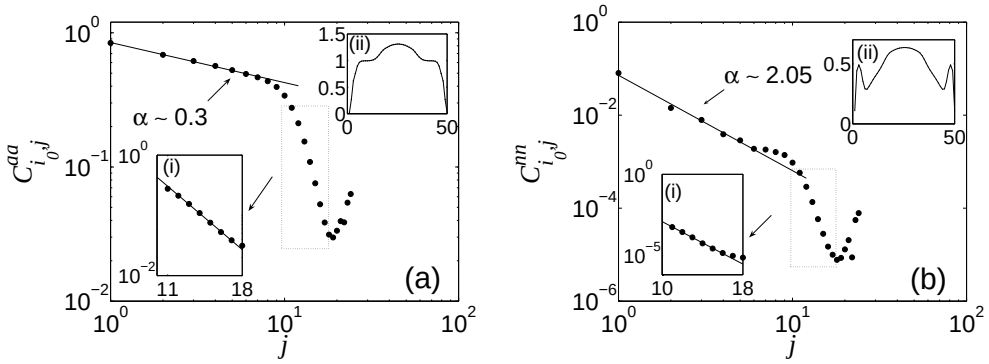

Figure 5.7: Correlation functions (a) $C^{aa}_{i_0,j}$ and (b) $C^{nn}_{i_0,j}$ in a linear Paul trap when $U/t = 2$ ($N = N_{\rm ph} = 50$). Both of them show the coexistence of superfluid and Mott-insulator phases. In (a) and (b), the insets (i) show the exponential decay in the region of the Mott phase, and the insets (ii) show the occupation number and fluctuations at the same parameters. The exponents α of the algebraic decay are also given in the figures. The dotted and solid lines are numerical and fitting data, respectively.

gas profile when increasing the interaction, and at the end it approaches a constant value of 1/2. Correlation functions decay algebraically, with an exponent that approaches $\alpha \approx 0.58$ for large interactions (see Fig. 5.11). Note that α deviates from 1/2, which is the value that corresponds to a Tonks gas with nearest–neighbor tunneling only. The deviation can be explained by the mapping from the BHM model (5.21) with $U \gg t$ to an XY model with antiferromagnetic interactions of the form $J_{i,j} = J/|i-j|^3$. The long–range terms in the antiferromagnetic interaction induces a change in the exponent of the correlation functions, as shown with the numerical calculations of our previous work on spin models in ion traps [72].

(2) Linear ion trap. We study now the case of phonons in a linear Paul trap under the same conditions, see Fig. 5.12. Correlation functions decay algebraically, with an exponent that is extrapolated to $\alpha = 0.53$ in the limit of strong interactions. This result can also be explained by the mapping to the XY model, and coincides with the result found in [72].

In order to test if the system is really in the Tonks–gas phase, we introduce the quantity $\langle O \rangle = \langle \sum_i n_i(n_i - 1) \rangle / N$, which measures the probability of phonon occupancies larger than one. In the Tonks–gas regime $\langle O \rangle \sim 0$. The parameter $\langle O \rangle$ as a function of the interaction U is plotted in Fig. 5.13, showing the continuous evolution into the Tonks–gas regime.

Our results are consistent with the behaviors observed in optical lattices

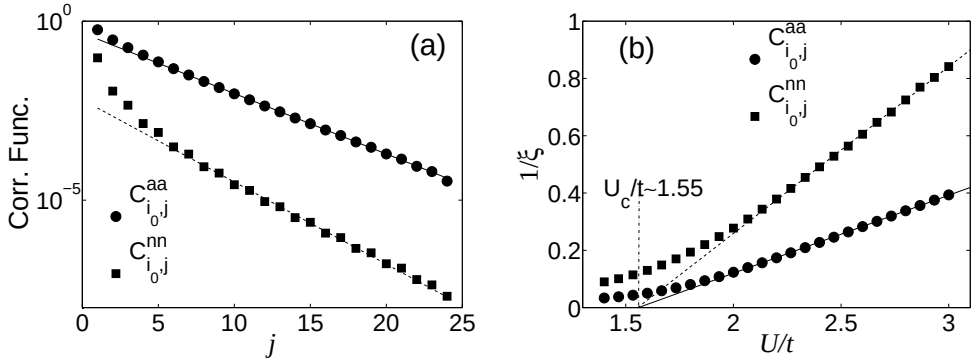

Figure 5.8: (a) Correlation functions $C^{aa}_{i_0,j}$ at $U/t = 3$ and $C^{nn}_{i_0,j}$ at $U/t = 2.4$ decay exponentially with the coordinate j at the Mott-insulator phase for an array of microtraps ($N = N_{\rm ph} = 50$, $i_0 = 26$). (b) The inverse of the correlation lengths in $C^{aa}_{i_0,j}$ and $C^{nn}_{i_0,j}$. The circle markers represent $C^{aa}_{i_0,j}$ and the square markers $C^{nn}_{i_0,j}$. The solid lines are the fitting data. The extrapolation in (b) show that the critical point in the microtraps is $U_c/t \approx 1.55$.

[33, 35]. The numerical analysis shows that phonons in ion traps are also a good candidate like atoms in optical lattices for studying Tonks gases.

5.5 Attractive interactions: $U < 0$

The BHM with attractive interactions in optical lattices has been the focus of recent theoretical studies [146,147,148]. The sign of phonon–phonon interactions in trapped ions can be made negative simply by changing the relative position of the standing–wave relative to the ion chain. For a qualitative understanding of this model, it is useful to consider a Bose–Einstein condensate in a double well potential [147,149,150]. In a symmetric potential in the absence of tunneling, energy is decreased when bosons accumulate in one of the wells. When tunneling is switched on, the ground state of the system is a linear superposition of states with all the bosons placed in one of the wells, showing large phonon number fluctuations.

The increase of phonon number fluctuations in our model when we switch on a negative interaction is also shown in our numerical calculations. In Fig. 5.14, the density at the center of the ion chain and its fluctuations increase with the magnitude of the interaction for $N = 10$ ions and $N_{ph} = 10$ phonons with open boundary conditions. Due to the open boundary condition and the symmetry of the potential, the phonons tend to collect themselves on one

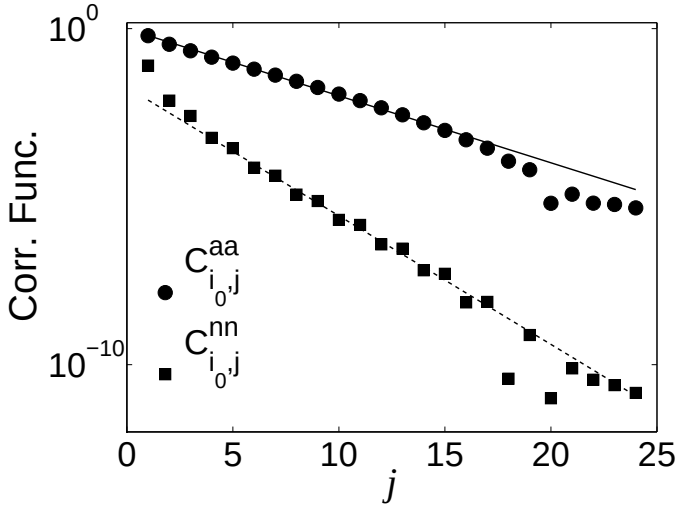

Figure 5.9: The exponential decay correlations $C^{aa}_{i_0,j}$ and $C^{nn}_{i_0,j}$ at the Mott phase $U/t = 2.8$ for a linear Paul trap ($N = N_{\rm ph} = 50$, $i_0 = 26$).

of the two sites at the center when increasing $|U|$ with an even number of sites. The ground state is then a superposition of N_{ph} phonons on site $N/2$ and N_{ph} phonons on site $N/2+1$.

When $|U|$ is large enough, our numerical calculations yield a ground state with all the phonons in a single ion, such that the spatial symmetry of the problem is broken. This effect is an artifact of the DMRG calculation, due to the small energy difference between the exact ground state of the system and the one which breaks the spatial symmetry. Thus, in order to study properly the phonon phases with negative interaction, it is convenient to define the following order parameter, whose value is independent on the breaking of the spatial symmetry in the problem:

$$\langle O \rangle = \frac{1}{N^2} \langle \sum_j (a_j^\dagger a_j)^2 \rangle. \tag{5.30}$$

In Fig. 5.15 we show the evolution of this quantity, which shows a sudden increase for negative interactions.

5.6 Site-dependent interactions

Phonons in trapped ions have a higher controllability than ultracold neutral atoms in optical lattices, due to the possibility of individual addressing. In

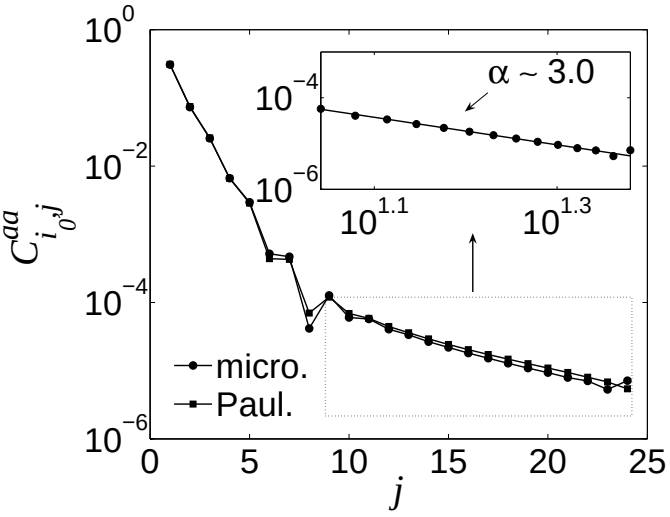

Figure 5.10: The correlation $C^{aa}_{i_0,j}$ at the Mott phase $U/t = 6$ in an array of microtraps (circle markers) and a linear Paul trap (square markers), respectively. $N = N_{\rm ph} = 50$, $i_0 = 26$. The inset shows the power-law decay with exponent $\alpha \approx 3$ for the microtraps only.

particular, on–site interactions can be induced in such a way that they depend on the ion position. In this section we present a model which shows how this possibility can be exploited for the engineering of quantum phases.

Let us consider repulsive on-site interactions which vary over the ion chain in the following way:

$$\begin{aligned} U_i = U_{\rm odd} = U, \qquad & \text{i odd}, \\ U_i = U_{\rm even} = 2U, \qquad & \text{i even}, \end{aligned} \tag{5.31}$$

We focus on the case with filling factor 2, $N_{\rm ph} = 2N$, in the regime where interactions dominate over tunneling, $U/t \gg 1$. In the limit $t = 0$, the ground state of this model is highly degenerate. For instance, in a chain with two sites the ground state manifold in the Fock basis spans the states $|2, 2\rangle$ and $|3, 1\rangle$. In a chain with even number N of sites and $N_{\rm ph} = 2N$, the ground state degeneracy is $\begin{pmatrix} N \\ N/2 \end{pmatrix}$.

Our DMRG algorithm allows us to calculate the density and fluctuations in the phonon number, which are shown in Fig. 5.16, for the case where the interactions defined by Eq. (5.31) are induced on an array of ion microtraps. In the ground state of the chain, the number of phonons fluctuates between $|2\rangle$ and $|3\rangle$, and $|2\rangle$ and $|1\rangle$, in odd and even sites, respectively.

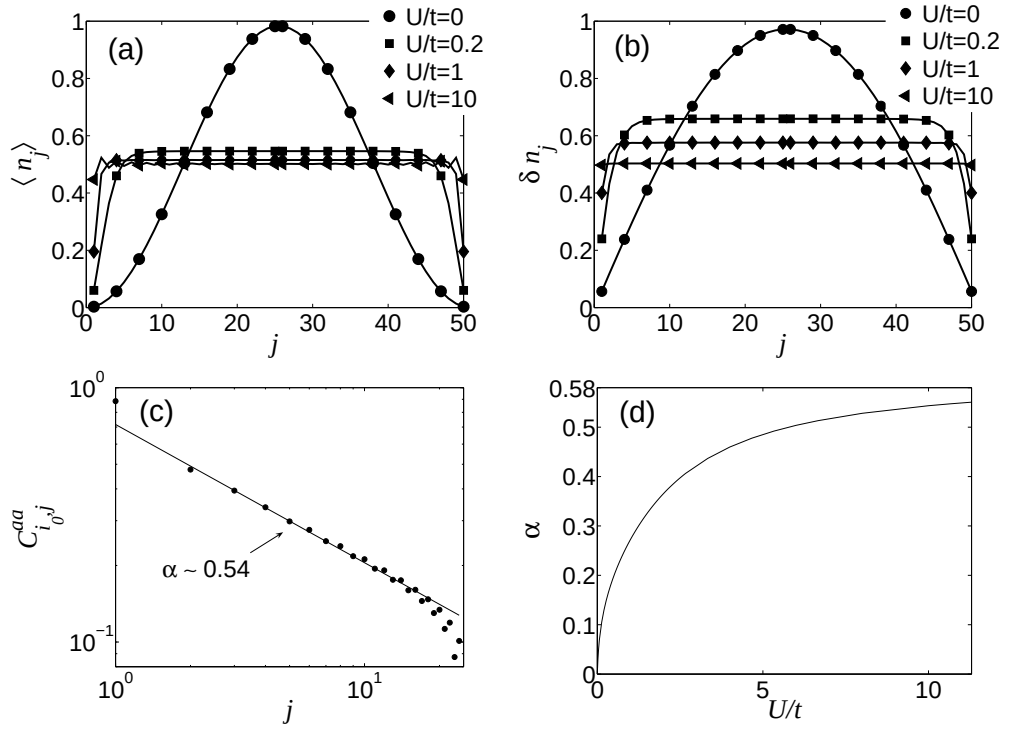

Figure 5.11: (a) Densities of phonons in an array of microtraps with $N = 50$, $N_{ph} = 25$. (b) Fluctuations at the same conditions. (c) The correlation function $C^{aa}_{i_0,j}$ ($i_0 = 26$) at Tonks-gas phase $U/t = 10$ with exponent $\alpha \approx 0.54$, where the dotted and solid lines are numerical and fitting data, respectively. (d) Evolution of exponent α of $C^{aa}_{i_0,j}$ with the interaction U/t, which would approach $\alpha \approx 0.58$.

This model can be understood in the hard–core boson limit by introducing a spin representation, which is valid near filling factor 2. At each site in the ion chain, we define a two level system by means of the following rule:

$$\begin{aligned} |\bar{0}\rangle_i = |2\rangle_i, \;\; |\bar{1}\rangle_i = |3\rangle_i, \qquad & \text{i odd}, \\ |\bar{0}\rangle_i = |1\rangle_i, \;\; |\bar{1}\rangle_i = |2\rangle_i, \qquad & \text{i even}. \end{aligned} \tag{5.32}$$

Where $|\bar{0}\rangle$ and $|\bar{1}\rangle$ are the two levels which define the spin states of the spin representation of the hard–core bosons. Spin and phonon annihilation

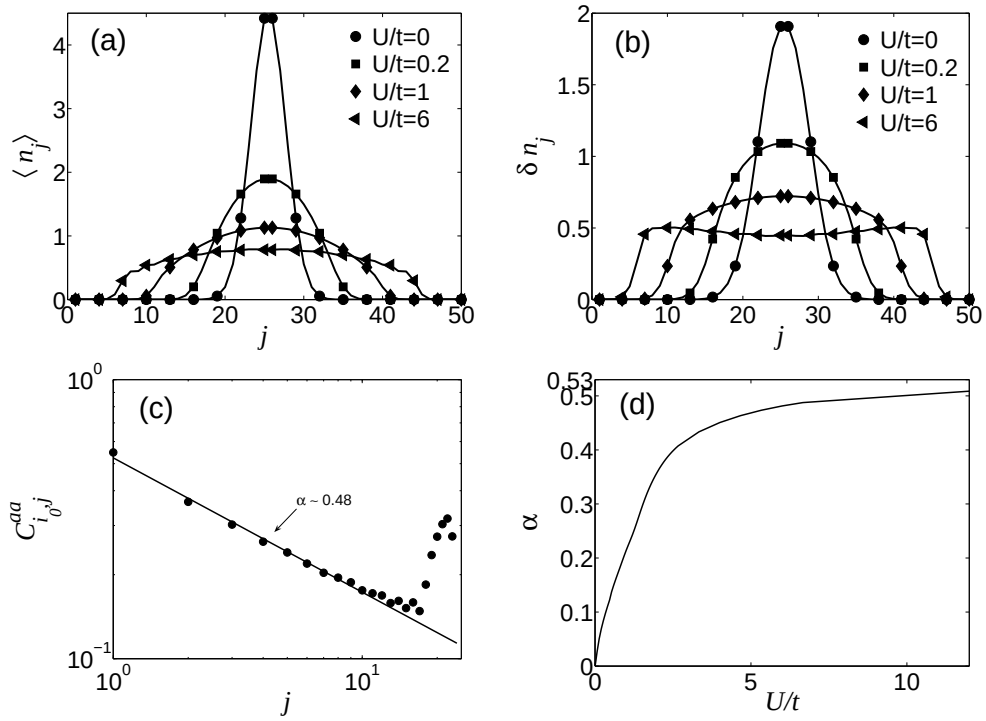

Figure 5.12: (a) and (b) show densities and fluctuations of phonons, respectively, in a linear Paul trap with $N = 50$ and $N_{ph} = 50$; (c) The correlation $C^{aa}_{i_0,j}$ at the Tonks-gas phase $U/t = 6$, whose exponent is $\alpha \approx 0.48$; (d) Evolution of the exponents α of $C^{aa}_{i_0,j}$, approaching $\alpha \approx 0.53$. In (c) the dotted and solid lines represent numerical and fitting data, respectively.

operators satisfy:

$$\begin{aligned} \sigma_i^+ &= \frac{1}{\sqrt{3}} a_i^\dagger, \text{ i odd,} \\ \sigma_i^+ &= \frac{1}{\sqrt{2}} a_i^\dagger, \text{ i even.} \end{aligned} \tag{5.33}$$

where the equality is understood to hold within the ground state manifold. In terms of this operators, the Hamiltonian of the system is described by an XY model (for simplicity we consider here the nearest-neighbor case):

$$H = \tilde{J} \sum_i (\sigma_i^+ \sigma_{i+1}^- + h.c.), \tag{5.34}$$

with $\tilde{J} = \sqrt{6}t$. Under the condition $N_{\rm ph}/N = 2$, the ground state of our

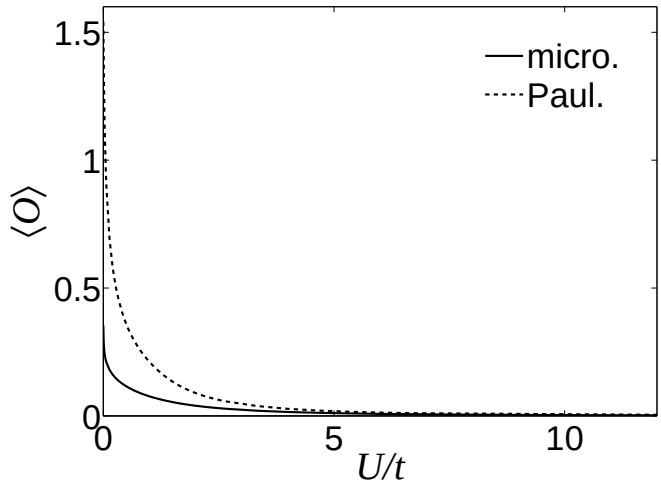

Figure 5.13: The evolution of the parameter $\langle O \rangle$ with the interaction U/t in an array of microtraps (solid line) and a linear Paul trap (dashed line). $N = 50$, $N_{\rm ph} = 25$.

hard–core boson Hamiltonian corresponds to the solution of the XY model (5.34) with the constraint $\sum_i \sigma_i^z = 0$.

Spin-spin correlation functions are related to the bosonic correlations functions of the BHM by the relation Eq. (5.33). In Fig. 5.17 we plot $\langle \sigma_i^+ \sigma_j \rangle$ calculated by means of correlation functions of hard–bosons. This correlation function shows an algebraic decay for short distances, which is spoiled for long separations between ions due to boundary effects. The exponent $\alpha \sim 0.56$, differs from the one that we expect from the mapping to the XY model, that is, $\alpha = 0.5$, due to the effect of further than nearest–neighbor interactions terms, which we have neglected.

Another interesting possibility is to study the phase diagram of the BHM with filling factor 2, and alternating interactions, beyond the XY point $U_{\rm even} = 2U_{\rm odd}$. If we change the ratio $U_{\rm even}/U_{\rm odd}$ in the vicinity of this point, the ground state degeneracy with zero tunneling is lifted. The system is in a Mott insulator phase, with constant phonon density if $U_{\rm even} < 2U_{\rm odd}$, $|2, 2, 2, \ldots\rangle$, or alternating occupation numbers if $U_{\rm even} > 2U_{\rm odd}$, $|3, 1, 3, 1, \ldots\rangle$. The phase diagram as a function of the ratio $U_{\rm even}/U_{\rm odd}$, shows two gaped regions, separated by a single critical point, which corresponds to the XY limit studied above. This is shown in Fig. 5.18, where we calculate the energy gap ΔE for small chains ($N = 6$).

To generalize, the same also takes place with other distributions of the on–

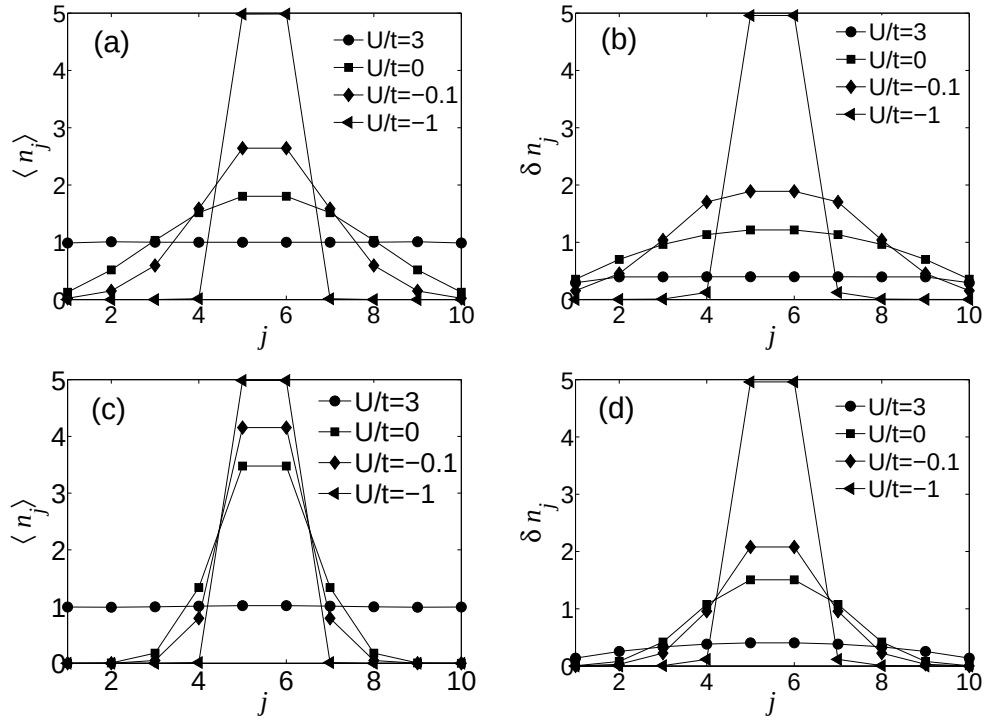

Figure 5.14: (a) Density of phonons and (b) phonon number fluctuations in an array of microtraps with $N = 10$, $N_{ph} = 10$, and negative on–site interactions . (c) Density of phonons and (d) phonon number fluctuations in a linear Paul trap under the same conditions.

site interactions, whenever the number of sites where phonons interact with U is the same as the number of sites with $2U$ interaction. For example, the chain can be divided in two regions, left and right, such that the interactions depend on the site in the way $U, U, ..., 2U, 2U, ...$, that is, $U_i = U_{\text{left}} = U$ and $U_i = U_{\text{right}} = 2U$.

5.7 Conclusions

In conclusion, we have studied the quantum phases of interacting phonons in ion traps. The superfluid–Mott insulator quantum phase transition can be detected by the evolution of the phonon density profile, as well as by the divergence of the correlation length near the quantum critical point. Although boundary effects are important, specially in the case of a Coulomb chain of ions, correlation functions show a similar behavior as those of systems in the

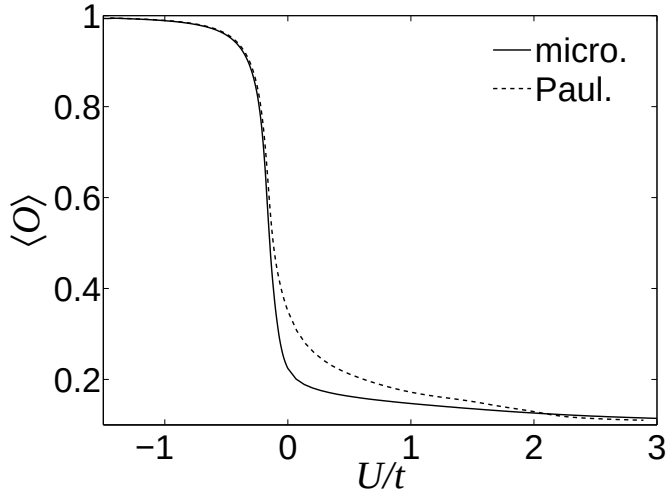

Figure 5.15: Evolution of the order parameter $\langle O \rangle$ with the ratio U/t for an array of ion microtraps (solid line) and a linear Paul trap (dashed line). $N = N_{\rm ph} = 10$.

thermodynamical limit. For example, Luttinger liquid theory gives an approximate description of the algebraic decay of correlations in the superfluid regime.

We have also shown that the ability to control phonon–phonon interactions allows us to study a variety of situations like attractive interactions, where a phase with large phonon number fluctuations takes place. The ability to tune locally the value of the on–site interactions also leads to the realization of new exciting models, where the degeneracy of the classical ground state can be tuned by choosing properly the value of the phonon–phonon interactions.

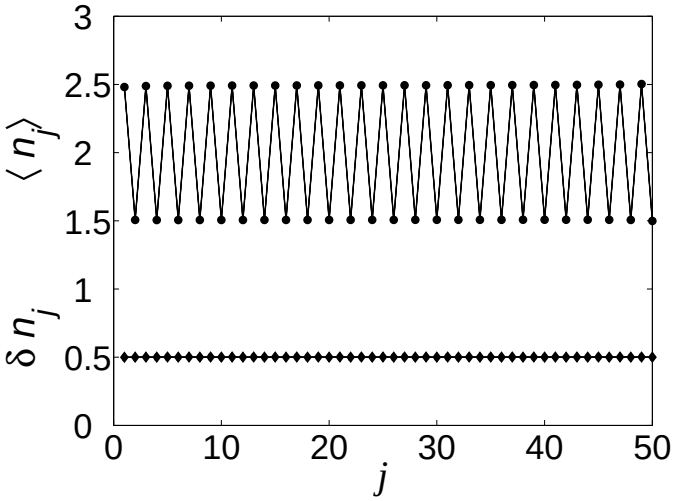

Figure 5.16: The phonon density $\langle n_j \rangle$ and phonon number fluctuations, δn_j, in an array of ion microtraps, with the on–site interactions defined by Eq. (5.31), $U/t = 40$, $N = 50$, and $N_{ph} = 2N = 100$.

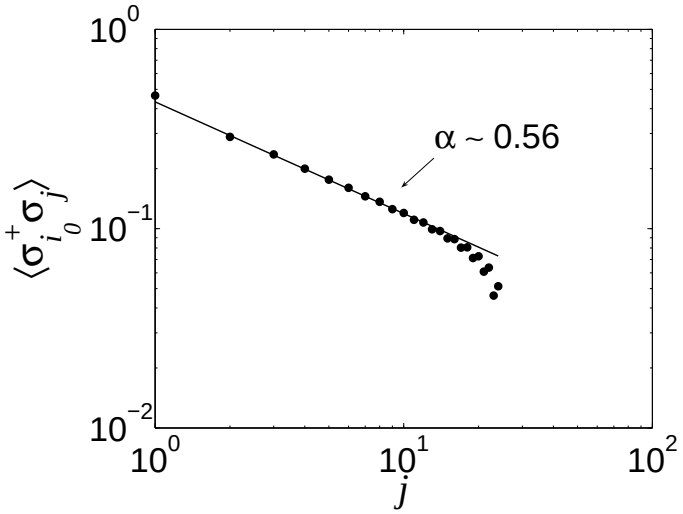

Figure 5.17: The correlation function $\langle \sigma^+_{i_0} \sigma_j \rangle$ defined by (5.32). $i_0 = 26$, $N = 50$, $N_{\rm ph} = 100$, $U/t = 40$.

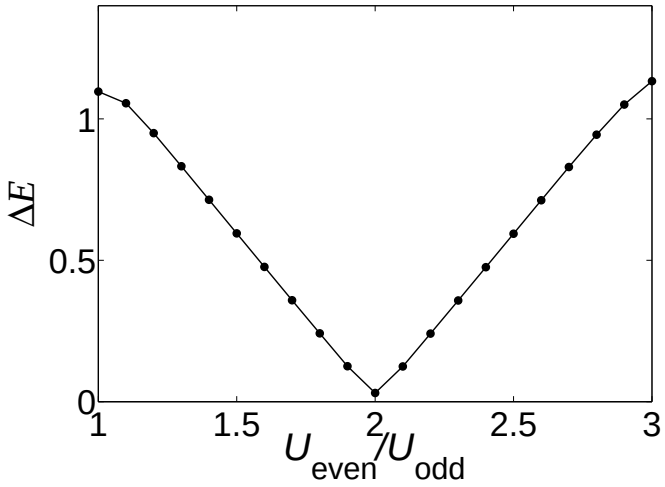

Figure 5.18: The energy gap ΔE between the ground state and the first excited state as a function of $U_{\text{even}}/U_{\text{odd}}$. $U_{\text{odd}}/t = 40$. For simplicity, we consider here a small system of ions $N = 6$.

Chapter 6

Conclusion and Outlook

In this thesis we have studied quantum simulations with trapped ions. By using internal states coupling to vibrational modes one can induce effective spin-spin interactions in such a way that a variety of quantum spin models can be implemented, such as quantum Ising, XY and Heisenberg models. On the other hand, radial phonons in a linear Paul trap or in an array of microtraps are similar to bosons in optical lattices. Inducing effective phonon-phonon interactions from the anharmonic terms of the expanding of the off-resonant standing wave, one can get the Bose-Hubbard Hamiltonian. Superfluidity and Tonks-gas of phonons could be observed for the first time in a linear Paul trap or an array of microtraps.

In ion traps quantum correlations can be studied with a degree of controllability that still is not possible in solid state or optical lattice set-ups. In this way a number of phenomena from quantum many body physics could be accessed for the first time in experiments. These quantum models that can be realized with trapped ions show also new remarkable features like coexistence of different phases and quantum correlation induced by long-range spin-spin interactions or boson-boson hoppings.

Trapped ions are ideally suited to build quantum simulators and explore a variety of quantum phase transitions. They have the advantages that quantum states can be prepared and measured at the single particle level, holes, impurities and defects which always exist in real materials can be avoided or can be added on purpose, dynamic behaviors can be investigated, and so on. In this thesis we exposed only a few applications of quantum simulations with trapped ions. In fact, our proposals with some modifications could be used to simulate many other systems of great interest in condensed matter physics. For instance, we can simulate quantum spin ladders, when we design that two XY chains are coupled by Ising interaction. A spin-boson Hamiltonian can also be realized under certain conditions when an ion is

in an off-resonant standing wave, where the bosonic bath is given by the vibrational modes of the ion. Our proposals have also potential applications to the 2D system of microtraps or the Penning trap. Furthermore, designing different laser configurations would lead to other novel Hamiltonians.

Bibliography

[1] T. Giamarchi, *Quantum Physics in One dimension* (Oxford University Press, Oxford, 2004).

[2] H. J. Metcalf and P. van der Straten, *Laser Cooling and Trapping*, (Springer-Verlag, New York, 2002).

[3] E. Jané, G. Vidal, W. Dür, P. Zoller, and J. I. Cirac, Quant. Inf. Comp. **3**, 15 (2003).

[4] D. Jaksch and P. Zoller, arXiv:cond-mat/0410614.

[5] M. Lewenstein, A. Sanpera, V. Ahufinger, B. Damski, A. Sen(De), and U. Sen, arXiv:cond-mat/0606771.

[6] R. P. Feynman, Int. J. Theor. Phys. **21**, 467 (1982).

[7] S. Lloyd, Science **273**, 1073 (1996).

[8] D. Jaksch, C. Bruder, J. I. Cirac, C. W. Gardiner, and P. Zoller, Phys. Rev. Lett. **81**, 3108 (1998).

[9] M. Greiner, O. Mandel, T. Esslinger, T. W. Hänsch, and I. Bloch, Nature **415**, 39 (2002).

[10] W. Hofstetter, J. I. Cirac, P. Zoller, E. Demler, and M. Lukin, Phys. Rev. Lett. **89**, 220407 (2002).

[11] J. J. Garcia-Ripoll and J. I. Cirac, New J. Phys. **5**, 76 (2003).

[12] L.-M. Duan, E. Demler, and M. D. Lukin, Phys. Rev. Lett. **91**, 090402 (2003).

[13] J. J. Garcia-Ripoll, M. A. Martin-Delgado, and J. I. Cirac, Phys. Rev. Lett. **93**, 250405 (2004).

[14] L. Santos, M. A. Baranov, J. I. Cirac, H.-U. Everts, H. Fehrmann, and M. Lewenstein, Phys. Rev. Lett. **93**, 030601 (2004).

[15] A. Sorensen, E. Demler, and M. Lukin, Phys. Rev. Lett. **94**, 086803 (2005).

[16] H. P. Büchler, M. Hermele, S. D. Huber, M. P. A. Fisher, and P. Zoller, Phys. Rev. Lett. **95**, 040402 (2005).

[17] A. Micheli, G. K. Brennen, and P. Zoller, arXiv:quant-ph/0512222.

[18] R. Barnett, D. Petrov, M. Lukin, and E. Demler, Phys. Rev. Lett. **96**, 190401 (2006).

[19] C. W. Zhang, V. W. Scarola, and S. Das Sarma, arXiv:cond-mat/0611689.

[20] A. Burkov and E. Demler, Phys. Rev. Lett. **96**, 180406 (2006).

[21] J. I. Cirac and P. Zoller, Science **301**, 176 (2003).

[22] J. I. Cirac and P. Zoller, Phys. Today **57**, 38 (2004).

[23] B. Laburthe Tolra, K. M. O'Hara, J. H. Huckans, W. D. Phillips, S. L. Rolston, and J. V. Porto, Phys. Rev. Lett. **92**, 190401 (2004).

[24] M. Köhl, H. Moritz, T. Stöferle, K. Günter, and T. Esslinger, Phys. Rev. Lett. **94**, 080403 (2005).

[25] K. Xu, Y. Liu, J. R. Abo-Shaeer, T. Mukaiyama, J. K. Chin, D. E. Miller, W. Ketterle, K. M. Jones, and E. Tiesinga, Phys. Rev. A **72**, 043604 (2005).

[26] C. Ryu, X. Du, E. Yesilada, A. M. Dudarev, S. Wan, Q. Niu, and D. Heinzen, arXiv:cond-mat/0508201.

[27] G. Thalhammer, K. Winkler, F. Lang, S. Schmid, R. Grimm, and J. H. Denschlag, Phys. Rev. Lett. **96**, 050402 (2006).

[28] L. Fallani, J. E. Lye, V. Guarrera, C. Fort, and M. Inguscio, arXiv:cond-mat/0603655.

[29] K. Günter, T. Stöferle, H.Moritz, M. Köhl, and T. Esslinger, Phys. Rev. Lett. **96**, 180402 (2006).

[30] S. Ospelkaus, C. Ospelkaus, O. Wille, M. Succo, P. Ernst, K. Sengstock, and K. Bongs, Phys. Rev. Lett. **96**, 180403 (2006).

[31] T. Volz, N. Syassen, D. M. Bauer, E. Hansis, S. Dürr, and G. Rempe, Nature Phys. **2**, 692 (2006).

[32] K. Winkler, G. Thalhammer, F. Lang, R. Grimm, J. Hecker-Denschlag, A. J. Daley, A. Kantian, H. P. Büchler, and P. Zoller, Nature **441**, 853 (2006).

[33] B. Paredes, A. Widera, V. Murg, O. Mandel, S. Fölling, I. Cirac, G. V. Shlyapnikov, T. W. Hänsch, and I. Bloch, Nature **429**, 277 (2004).

[34] H. Moritz, T. Stöferle, M. Köhl, and T. Esslinger, Phys. Rev. Lett. **91**, 250402 (2003).

[35] T. Kinoshita, T. Wenger, and D. S. Weiss, Science **305**, 1125 (2004)

[36] T. Stöferle, H. Moritz, C. Schori, M. Köhl, and T. Esslinger, Phys. Rev. Lett. **92**, 130403 (2004).

[37] M. Greiner, C. A. Regal, and D. S. Jin, Nature **426**, 537 (2003).

[38] M. Bartenstein, A. Altmeyer, S. Riedl, S. Jochim, C. Chin, J. H. Denschlag, and R. Grimm, Phys. Rev. Lett. **92**, 120401 (2004).

[39] M. W. Zwierlein, C. A. Stan, C. H. Schunck, S. M. F. Raupach, A. J. Kerman, and Ketterle, Phys. Rev. Lett. **92**, 120403 (2004).

[40] T. Bourdel, L. Khaykovich, J. Cubizolles, J. Zhang, F. Chevy, M. Teichmann, L. Tarruell, S. J. J. M. F. Kokkelmans, and C. Salomon, Phys. Rev. Lett. **93**, 050401 (2004).

[41] J. Kinast, S. L. Hemmer, M. E. Gehm, A. Turlapov, and J. E. Thomas, Phys. Rev. Lett. **92**, 150402 (2004).

[42] P. K. Ghosh, *Ion traps*, (Oxford University Press, 1995)

[43] A. Steane, Appl. Phys. B. **64**, 623 (1997).

[44] D. J. Winland, C. Monroe, W. M. Itano, D. Leibfried, B. E. King, and D. M. Meekhof, J. Res. Natl. Inst. Stand. Technol. **103**, 259 (1998).

[45] D. F. V. James, Appl. Phys. B **66**, 181 (1998).

[46] M. Šašura and V. Bužek, arXiv:quant-ph/0112041.

[47] D. Leibfried, R. Blatt, C. Monroe, and D. Wineland, Rev. Mod. Phys. **75**, 281 (2003).

[48] M. Nielsen and I. Chuang, *Quantum Computation and Quantum Information*, (Cambridge University Press, Cambridge, 2000).

[49] D. Bouwmeester, A. Ekert, and A. Zeilinger (Eds.), *The Physics of Quantum Information* (Springer-Verlag, Berlin, 2001).

[50] J. I. Cirac, L.-M. Duan, and P. Zoller, arXiv:quant-ph/0405030.

[51] J. I. Cirac and P. Zoller, Phys. Rev. Lett. **74**, 4091 (1995).

[52] C. Monroe, D. M. Meekhof, B. E. King, W. M. Itano, and D. J. Wineland, Phys. Rev. Lett. **75**, 4714 (1995).

[53] J. F. Poyatos, J. I. Cirac, and P. Zoller, Phys. Rev. Lett. **81**, 1322 (1998).

[54] A. Sørensen and K. Mølmer, Phys. Rev. Lett. **83**, 2274 (1999).

[55] A. Sørensen and K. Mølmer, Phys. Rev. A **62**, 022311 (2000).

[56] J. I. Cirac and P. Zoller, Nature **404**, 579 (2000).

[57] D. Kielpinski, C. Monroe, and D. J. Wineland, Nature **417**, 709 (2002).

[58] D. Leibfried, B. DeMarco, V. Meyer, D. Lucas, M. Barrett, J. Britton, W. M. Itano, B. Jelenkovi, C. Langer, T. Rosenband, and D. J. Wineland, Nature **422**, 412 (2003).

[59] T. Calarco, J. I. Cirac, and P. Zoller, Phys. Rev. A **63**, 062304 (2001).

[60] D. M. Meekhof, C. Monroe, B. King, W. M. Itano, and D. J. Wineland, Phys. Rev. Lett. **76**, 1796 (1996).

[61] H. Nägerl, D. Leibfried, H. Rohde, G. Thalhammer, J. Eschner, F. Schmidt-Kaler, and R. Blatt, Phys. Rev. A 60, 145 (1999).

[62] R. J. Rafac, B. C. Young, J. A. Beall, W. M. Itano, D. J. Wineland, and J. C. Bergquist, Phys. Rev. Lett. **85**, 2462 (2000).

[63] C. A. Sackett, D. kielpinski, B. E. King, C. Langer, V. Meyer, C. J. Myatt, M. Rowe, Q. A. Turchette, W. M. Itano, D. J. Wineland, and C. Monroe, Nature **404**, 256 (2000).

[64] S. Gulde, M. Riebe, G. P. T. Lancaster, C. Becher, J. Eschner, H. Häffner, F. Schmidt-Kaler, I. L. Chuang, and R. Blatt, Nature **421**, 48 (2003).

[65] J. Chiaverini, J. Britton, D. Leibfried, E. Knill, M. D. Barrett, R. B. Blakestad, W. M. Itano, J. D. Jost, C. Langer, R. Ozeri, T. Schaetz, and D. J. Wineland, Science **308**, 997 (2005).

[66] K.-A. Brickman, P. C. Haljan, P. J. Lee, M. Acton, L. Deslauriers, and C. Monroe, Phys. Rev. A **72**, 050306(R) (2005).

[67] H. Häffner, W. Hänsel, C. F. Roos, J. Benhelm, D. Chekalkar, M. Chwalla, T. Körber, U. D. Rapol, M. Riebe, P. O. Schmidt, C. Becher, O. Gühne, W. Dür, and R. Blatt, Nature **438**, 643 (2005).

[68] D. Leibfried, E. Knill, S. Seidelin, J. Britton, R. B. Blakestad, J. Chiaverini, D. B. Hume, W. M. Itano, J. D. Jost, C. Langer, R. Ozeri, R. Reichle, and D. J. Wineland, Nature **438**, 639 (2005).

[69] D. J. Wineland, C. Monroe, W. M. Itano, B. E. King, D. Leibfried, C. Myatt, and C. Wood, Phys. Scipt. **T76**, 147 (1998).

[70] D. Porras and J. I. Cirac, Phys. Rev. Lett. **92**, 207901 (2004).

[71] D. Porras and J. I. Cirac, Phys. Rev. Lett. **93**, 263602 (2004).

[72] X.-L. Deng, D. Porras, and J. I. Cirac, Phys. Rev. A **72**, 063407 (2005).

[73] J. P. Barjaktarevic, G. J. Milburn, and R. H. McKenzie, Phys. Rev. A **71**, 012335 (2005).

[74] D. Porras and J. I. Cirac, Phys. Rev. Lett. **96**, 250501 (2006).

[75] X.-L. Deng, D. Porras, and J. I. Cirac, arXiv:quant-ph/0703178.

[76] S. White, Phys. Rev. Lett. **69**, 2863 (1992).

[77] S. White, Phys. Rev. B. **48**, 10345 (1993).

[78] W. Paul, Rev. Mod. Phys. **62**, 531 (1990).

[79] S. Stenholm, Rev. Mod. Phys. **58**, 699 (1986).

[80] J. I. Cirac, R. Blatt, P. Zoller, and W. D. Phillips, Phys. Rev. A **46**, 2668 (1992).

[81] C. J. Foot, *Atomic Physics* (Oxford University Press, Oxford, 2005).

[82] R. G. DeVoe, Phys. Rev. A **58**, 910 (1998).

[83] M. J. Madsen, W. K. Hensinger, D. Stick, J. A. Rabchuk, and C. Monroe, Appl. Phys. B **78**, 639 (2004).

[84] D. Stick, W. K. Hensinger, S. Olmschenk, M. J. Madsen, K. Schwab, and C. Monroe, Nature Physics **2**, 36 (2006).

[85] P. Meystre, *Atom Optics* (Springer-Verlag, New York, 2001).

[86] J. Collaway, *Quantum Theory of the Solid State* (Academic Press, New York, 1976)

[87] T. P. Meyrath and D. F. V. James, Phys. Lett. A **240**, 37 (1998).

[88] R. R. Puri, *Mathematical Methods of Quantum Optics* (Springer-Verlag, Heidelberg, 2001)

[89] D. F. Walls and G. J. Milburn, *Quantum Optics* (Springer-Verlag, Heidelberg, 1994).

[90] J.I. Cirac, A.S. Parkins, R. Blatt and P. Zoller, Adv. At. Mol. Opt. Phys. **37**, 237 (1996).

[91] P. Zoller, *Quantum Optics*, the lecture at the University of Innsburck.

[92] B. E. King, PhD thesis, University of Colorado, 1999.

[93] W. Vogel and D.-G. Welsch, *Quantum Optics: An Introduction* (Wiley-VCH, Weinheim, 2006).

[94] I. Peschel, X. Q. Wang, M. Kaulke, and K. Hallberg (Eds.), *Density-Matrix Renormalization: A New Numerical Method in Physics* (Springer-Verlag, Berlin, 1999).

[95] N. Shibata, J. Phys. A **36**, 381 (2003).

[96] U. Schollwöck, Rev. Mod. Phys. **77** 259 (2005).

[97] G. Vidal, Phys. Rev. Lett. **91**, 147902 (2003).

[98] F. Verstraete, M. A. Martin-Delgado, and J. I. Cirac, Phys. Rev. Lett. **92**, 087201 (2004).

[99] F. Verstraete, D. Porras, and J. I. Cirac, Phys. Rev. Lett. **93**, 227205 (2004).

[100] F. Verstraete, J. J. Garcia-Ripoll, and J. I. Cirac, Phys. Rev. Lett. **93**, 207204 (2004).

[101] M. Zwolak and G. Vidal, Phys. Rev. Lett. **93**, 207205 (2004).

[102] D. Porras, F. Verstraete, and J. I. Cirac, Phys. Rev. B **73**, 014410 (2006).

[103] S. Östlund and S. Rommer, Phys. Rev. Lett. **75**, 3537 (1995).

[104] M. Fannes, B. Nachtergaele, and R. F. Werner, Comm. Math. Phys. **144**, 443 (1992).

[105] G. Vidal, Phys. Rev. Lett. **93**, 040502 (2004).

[106] S. R. White and A. Feiguin, Phys. Rev. Lett. **93**, 076401 (2004).

[107] U. Schollwöck and S. R. White, arXiv:cond-mat/0606018.

[108] N. Metropolis, A. W. Rosensbluth, M. N. Rosensbluth, A. H. Teller, and E. Teller, J. Chem. Phys. **21**, 1087 (1953).

[109] K. G. Wilson, Rev. Mod. Phys. **47**, 773 (1975).

[110] R. A. Horn and C. R. Johnson, *Matrix Analysis* (Cambridge University Press, Cambridge, 1985).

[111] A. Peres, *Quantum Theory: Concepts and Methods* (Kluwer, Dordrecht, 1993).

[112] S. R. White, Phys. Rev. Lett. **77**, 3633 (1996).

[113] U. Schollwöck, Phys. Rev. B **58**, 8194 (1998).

[114] L. Q. Sun, J. Zhang, S. J. Qin, and Y. Lei, Phys. Rev. B **65**, 132412 (2002).

[115] S. Nigg, Diploma thesis, Technische Universität München, 2004.

[116] E. Lieb, T. Schultz, and D. Mattis, Ann. Phys. **16**, 407 (1961).

[117] P. Pfeuty, Ann. Phys. **57**, 79 (1970).

[118] B.K. Chakrabarti, A. Dutta and P. Sen, *Quantum Ising Phases and Transitions in Transverse Ising Models* (Springer–Verlag, Berlin, 1996).

[119] S. Sachdev, *Quantum Phase Transitions* (Cambridge University Press, Cambridge, 1999).

[120] U. Busch and K. A. Penson, Phys. Review B (36), 9271 (1987).

[121] S. Katsura, Phys. Rev. **127**, 1508 (1962).

[122] E. Barouch, B. M. McCoy, and M. Dresden, Phys. Rev. A **2**, 1075 (1970).

[123] E. Barouch and B. M. McCoy, Phys. Rev. A **3**, 786 (1971).

[124] E. Barouch and B. M. McCoy, Phys. Rev. A **3**, 2137 (1971).

[125] R. Jullien and P. Pfeuty, Phys. Rev. B **19**, 4646 (1979).

[126] D.H.E. Dubin and T.M. O'Neil, Rev. Mod. Phys. **71**, 87 (1999).

[127] F. Mintert and C. Wunderlich, Phys. Rev. Lett. **87**, 257904 (2001).

[128] C. Wunderlich, arXiv:quant-ph/0111158.

[129] W. H. Zurek, U. Dorner, and P. Zoller, Phys. Rev. Lett. **95**, 105701 (2005).

[130] A. Dutta, J.K. Bhattacharjee, Phys. Rev. B **64**, 184106 (2001).

[131] N. Schuch, J. I. Cirac, and M. M. Wolf, Commun. Math. Phys. **267**, 65 (2006).

[132] A. Auerbach, *Interacting electrons and quantum magnetism* (Springer–Verlag, New York, 1994).

[133] F. Pázmándi and Z. Domanski, J. Phys. A **26**, L689 (1993).

[134] F. Pázmándi and Z. Domanski, Phys. Rev. Lett. **74**, 2363 (1995).

[135] M. Fisher, P. Weichman, G. Grinstein, and D. Fisher, Phys. Rev. B **40**, 546 (1989).

[136] K. Sheshadri, H. R. Krishnamurthy, R. Pandit, and T. V. Ramakrishnan, Europhys. Lett. **22**, 257 (1993).

[137] D. S. Rokhsar and B. G. Kotliar, Phys. Rev. B **44**, 10328 (1991).

[138] W. Krauth, M. Caffarel, and J.-P. Bouchaud, Phys. Rev. B **45**, 3137 (1992).

[139] J. K. Freericks and H. Monien, Europhys. Lett. **26**, 545 (1994).

[140] G. G. Batrouni, R. T. Scalettar, and G. T. Zimanyi, Phys. Rev. Lett. **65**, 1765 (1990).

[141] T. D. Kühner, S. R. White, and H. Monien, Phys. Rev. B **61**, 12474 (2000).

[142] C. Kollath, U. Schollwöck, J. von Delft, and W. Zwerger, Phys. Rev. A **69**, 031601(R) (2004).

[143] F.M.D. Haldane, Phys. Rev. Lett. **47**, 1840 (1981).

[144] D.M. Gangardt and G.V. Shlyapnikov, Phys. Rev. Lett. **90**, 010401 (2003).

[145] K.V. Kheruntsyan, D.M. Gangardt, P.D. Drummond, and G.V. Shlyapnikov, Phys. Rev. A **71**, 053615 (2005).

[146] J. Dorignac, J. C. Eilbeck, M. Salerno, and A. C. Scott, Phys. Rev. Lett. **93**, 025504 (2004).

[147] M.W. Jack and M. Yamashita, Phys. Rev. A **71**, 023610 (2005).

[148] P. Buonsante, V. Penna, and A. Vezzani, Phys. Rev. A **72**, 043620 (2005).

[149] M.J. Steel and M.J. Collett, Phys. Rev. A **57**, 2920 (1998).

[150] J. I. Cirac, M. Lewenstein, K. Mølmer, and P. Zoller, Phys. Rev. A **57**, 1208 (1998).

Acknowledgements

First and foremost I would like to thank my thesis supervisor Ignacio Cirac for the guidance and support he has provided throughout the course of this work. I am especially grateful for the inspiring and instructive discussions with him that have widened my fundamental understanding of physics.

I am deeply thankful to my co-supervisor Diego Porras for his careful guidance and great help throughout this work. I am especially grateful for many fruitful and constructive discussions with him in physics.

I also thank Valentin Murg, Tommaso Roscilde, Juan Jose Garcia-Ripoll for their valuable advice concerning questions in condensed matter physics.

My regards extend to all my colleagues and friends at the Max-Planck Institute, especially to Tassilo Keilmann, Michael Wolf, Geza Giedke, Karl Gerd Vollbrecht, Henning Christ and Markus Pop for their help.

Last but not least, I wish to thank my wife Yang Ma and my daughter AnQi for the encouragement and love I have received throughout my time at the MPQ. Without their love and support the completion of this work would not have been possible.

I gratefully acknowledge the scholarship of the DAAD to support my PhD studies at the MPQ, and four-months German language learning in Frankfurt.